Stiffness-Modulation of Multi-DoF Pneumatic Soft Actuator for Minimally Invasive Surgery

August 2024

Yuxi LU

Department of Medical Engineering,
Graduate School of Science and Engineering

Chiba University

（千葉大学審査学位論文）

Stiffness-Modulation of Multi-DoF Pneumatic Soft Actuator for Minimally Invasive Surgery

August 2024

Yuxi LU

Department of Medical Engineering,
Graduate School of Science and Engineering

Chiba University

ABSTRACT

Soft actuators have demonstrated significant potential for minimally invasive surgeries (MIS). In complex MIS procedures, such as single-port transvesical prostatectomy, precise navigation in unstructured environments (e.g., the bladder and urethra) and stable control of surgical instruments are critical. Actuators used in these contexts require multiple degrees of freedom (multi-DoF) and stiffness modulation. Multiple pneumatic antagonistic chambers in these actuators not only enable the necessary multi-DoF but also facilitate stiffness modulation without additional equipment. However, the necessity to insert endoscopes through the hollow central passage for single-port MIS introduces complexities in the interaction between soft actuators and endoscopes, complicating maneuverability and control properties. Moreover, this passage affects the internal stress distribution during the inflation of multiple antagonistic chambers, which challenge our understanding of the stiffness modulation mechanisms in multi-DoF soft actuators.

In designing soft actuators for MIS, it is crucial to consider the constraints imposed by the sizes and materials of MIS instruments, as these factors directly influence the design and functionality of pneumatic chambers. Our study focused on how these design constraints of cross-sectional pneumatic chambers affect their interaction with endoscopes, significantly impacting performance. While previous research has briefly touched on the impact of chamber shapes on bending properties, our comprehensive exploration via Finite Element Analysis (FEA) simulations and prototype testing identified friction as a critical factor. We found that wider chambers, influenced by material choices and dimensional constraints, amplify frictional forces, thereby improving maneuverability, control properties, and stiffness adjustability.

To clarify the mechanisms of stiffness modulation in multi-DoF soft actuators, we constructed, validated, and analyzed an FEA simulation model. Our findings revealed that inflating specific chambers generates bending moments that affect deformation responses to external loads and influence stiffness. This process also impacts the hollow central passage's bending moment, geometrical moment of inertia and modifies the tensile and compressive regions during bending, further affecting stiffness.

Addressing the need for precise stiffness selection based on external load, we introduced an advanced neural network mechanism for external loads, particularly those from neighboring organs. Given the non-linear dynamics of actuators and the unpredictability of surgery, we implemented an environment exploration strategy. Combined with the neural network's inverse dynamics model, this ensures adjusting stiffness for various external loads and endoscopes.

Finally, to validate the practical relevance of our research, we devised a preliminary master-slave framework. Initial surgical simulations underscored our actuator's potential, highlighting its ability to improve surgical precision and safety in transvesical prostatectomy. Our research deepens the understanding of stiffness modulation in soft actuators, offering valuable insights for improving the design and performance of actuators in complex MIS.

ACKNOWLEDGEMENTS

First and foremost, I wish to convey my deepest gratitude to my advisor, Professor Yu, for his unwavering support and invaluable guidance throughout my doctoral research. His patient, comprehensive guidance, continuous encouragement, and acceptance of my shortcomings have been indispensable. He has consistently strived to help me develop the skills and qualities of a dedicated researcher, for which I am profoundly grateful.

I am also deeply grateful to Professor Igarashi for his selfless collaboration and essential advice in medical surgical procedures, which significantly advanced my research and improved the clinical applicability of my findings. Furthermore, this project could not have been realized without the generous support of the Chiba University Research Fellowship for Informatics-Based Medical Engineering.

My sincere appreciation goes to the members of my defense committee: Prof. Nakaguchi, Prof. Namiki, Prof. Nakagawa, Prof. Igarashi, Prof. Gomez for their generous contributions of knowledge and expertise, which enriched the quality of this work.

I would like to thank our laboratory secretary, Osugi, for her vital assistance in the smooth procurement of experimental tools and materials. Her efficiency and dedication were instrumental in ensuring the seamless execution of my research.

I also express my heartfelt gratitude to my laboratory colleagues for fostering a stimulating and supportive research environment. Special acknowledgment goes to Zhou, Tanno, and Tortós Vinocour for their invaluable assistance with experiments, editorial help, and insightful advice.

Lastly, but most importantly, I offer my profound thanks to my family and friends for their immense support, unwavering encouragement, and enduring belief in my abilities. Their faith has been a key motivator, consistently uplifting my spirits and inspiring me to persevere throughout this endeavor.

CONTENTS

LIST OF TABLES

Contents Page

LIST OF FIGURES

Contents Page

1. Introduction

1.1. Preface

This chapter provides the background, problem statement, and purpose of this doctoral project. It begins by discussing the role of soft actuators in the minimally invasive surgery (MIS) and identifies the requirements for their application in complex MIS procedures: 1) the need for inserting surgical instruments into the soft actuator, 2) the necessity of multi degrees of freedom (Multi-DoF) movement, and 3) stiffness modulation. The necessity of these requirements will also be highlighted. The final segment of this chapter will summarize the purposes, limitations, and contributions of the project, culminating with an outline of the thesis structure.

1.2. Background

MIS offers an alternative to traditional surgical procedures that required larger incisions [1]. Studies have shown that MIS provides benefits such as increased safety, improved cosmesis, shorter recovery periods, reduced postoperative complications, and decreased patient discomfort [1].

A significant advancement in MIS is the integration of robotic surgical systems. The da Vinci robotic system, particularly in robotic simple prostatectomy for transvesical procedures, has been extensively researched. Studies have linked its use to reduced intraoperative blood loss and shorter hospital stays [2], [3]. It has also been effective in addressing coexisting bladder conditions, adhering to the principles of open simple prostatectomy (OSP) [4], [5]. For patients with benign prostatic hyperplasia (BPH) and significant prostate enlargement, using MIS techniques in conjunction with robotic systems is recommended [6], [7].

However, challenge in MIS remain. Robotic systems, such as the da Vinci, primarily use rigid instruments. When multiple instruments are used in the limited MIS workspace, interference can occur. This constrained, deformable, and dynamic workspace often challenge the maneuverability of rigid instruments. The "fulcrum effect" with rigid endoscopes can complicate surgical movements [8]. In transvesical prostatectomy, using rigid instruments in tight areas like the intra-bladder space risks unintended tissue contact [4], [9], which can endanger the patient [5], [10], [11]. Additionally, the significant footprint and costs of advanced robotic systems like the da Vinci hinder their broader adoption. Therefore, innovative solutions in MIS are needed [10].

Several companies, including Ambu Inc. and Olympus Corp., have introduced flexible endoscopes designed with a single Degree of Freedom (DoF) to permit lens rotation within the body and an access channel for surgical instruments. While beneficial in surgeries like thoracoabdominal and bladder-related procedures, their single DoF limits maneuverability in more complex surgeries.

To address these limitations, research in soft robotics is gaining prominence. Unlike conventional robotics with rigid components, soft robotics employs highly compliant

materials, allowing more nuanced interactions in unstructured environments and reducing potential harm to adjacent tissues [12], [13]. These materials' ability to adaptively deform presents a solution to the maneuverability issues in current flexible endoscopes [14].

In MIS, single-port surgical techniques offer benefits such as fewer incisions, reduced bleeding, and quicker recovery times compared to multiport or open surgery [3], [15]. These techniques are effective in urological surgeries, particularly transvesical prostatectomy for severe benign prostatic hyperplasia (BPH) [15], [6], [7], [16], [17]. Surgical instruments are introduced at the bladder apex and maneuvered along the bladder neck's curvature. This procedure requires the end-effector to navigate through a confined space with limited visibility, making the diameter difference between the insertion section and the end-effector's flexibility critical. These surgeries present challenge due to limited access, reduced maneuverability, and the risk of unintended tissue contact with rigid instruments [4], [9].

Therefore, precise navigation of surgical instruments through the bladder while maintaining a stable posture is needed for various surgical actions [10]. Actuators designed for this purpose must offer multi-DoF and stiffness modulation [9], [18], [19], [20], [21]. This combination is expected to facilitate precise navigation through tissues or organs with minimal invasiveness for complex procedures like single-port transvesical prostatectomy (see Figure 1.1).

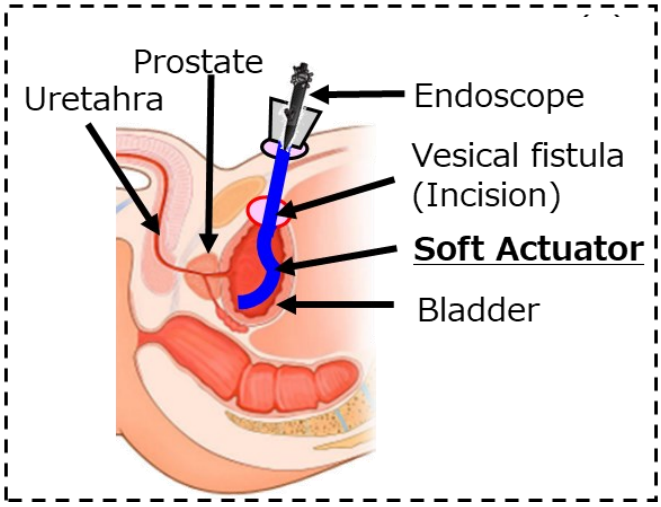

Figure 1.1 Schematic of Single-Port Transvesical Prostatectomy

Pneumatic soft actuators, a key advancement in soft robotics, use internally embedded air chambers that can be pressurized and depressurized to enable movement and shape alterations [12], [17], [20]. These actuators, designed with multiple air chambers in various sections, allow for the construction of soft actuators with multiple Degrees of Freedom (DoFs). This multi-DoF feature is essential for precise navigation through tissues or organs during complex surgical procedures, enabling the actuator to perform a variety of surgical actions such as cutting, suturing, and manipulating tissues.

Hollow central ducts within the actuator are designed to accommodate and guide surgical instruments to the surgical site alongside the actuator for single-port MIS [17], [20], [21]. Another approach involves multi-DoF soft actuators equipped with a tendon-driven mechanism that uses fibers or threads for actuation, resembling muscle fibers, and employing semi-rigid materials to generate movement and force. However, incorporating semi-rigid components may compromise the overall softness of the actuators, potentially increasing invasiveness and limiting the ability to navigate the confined or highly flexible environments characteristic of MIS [12]. In contrast, pneumatic soft actuators maximize material softness, ensuring minimal invasiveness and broader operational flexibility.

1.3. Problem Statement

1.3.1 Chamber Shapes Influence Soft Actuators

- **Cross-sectional Chamber Shape**

In the intricate design of soft actuators for minimally invasive surgeries (MIS), understanding the specific constraints imposed by the MIS environment and equipment is crucial. The size and choice of materials used in MIS instruments, particularly the specifications related to the outer and inner diameters of the actuator, are inherently limited and play a pivotal role in design considerations. These constraints do not merely enhance the importance of the cross-sectional chamber shape; rather, they underscore a fundamental principle in soft actuator design. The shape of these chambers is critical not only for fitting within the confined spaces typical of MIS procedures but also for ensuring optimal interaction between the actuator and the endoscope. This interaction is key to achieving the desired maneuverability and precision in surgical tasks.

The chamber shape significantly affects how forces are transmitted and controlled within the actuator, influencing the actuator's bending response and its ability to navigate and operate within the complex anatomical pathways encountered in MIS. Therefore, even without the stringent constraints of an MIS environment, the deliberate design of chamber shape remains essential. It determines the efficacy of the actuator by affecting aspects such as force distribution, bending flexibility, and operational stability. This critical design element ensures that actuators can meet both the rigorous demands of specific surgical tasks and adapt to broader applications where versatility and precision are required.

- **Complex Interaction**

One method of employing soft actuators in MIS is to use them as bidirectional bending access channels for surgical instruments [17]. These actuators feature broad internal channels designed to accommodate both surgical instruments and endoscopes, facilitating interactions between them. By increasing the Degrees of Freedom (DoF) and range of motion, soft actuators enable MIS to access hard-to-reach areas within the body, ensuring safe navigation among organs.

Many of these actuators are made from elastomeric materials, such as silicone rubbers, typically with a shore hardness of 10-30A [19]. In contrast, mainstream endoscopes from companies like Ambu Inc. and Olympus Corp. are constructed from

stiffer materials for functionalities like damage prevention, water resistance, and signal transmission, resulting in an overall stiffness of approximately 50A. This stark contrast in material properties can pose challenge during interaction. Factors such as contact surface area, endoscope stiffness, and friction are vital determinants of this dynamic.

Friction significantly affects the bending and response properties of the actuator [12] and leads to relative sliding between components due to the disparity in stiffness. This can cause actuation delays and influence other essential properties of the actuator.

- **Related Research and Challenge in Cross-sectional Chamber Shape**

Previous studies [11], [17], [22], [23], [24] have highlighted the effects of various chamber shapes, such as circular [17], [22], rectangular [17], semicircular [24], [25], and fake crescent [24], [26], on the bending properties of soft actuators. However, the broader implications for enhancing the navigational process of endoscopes during MIS [17] remain unknown.

A notable gap exists in our holistic understanding of the broad implications of these chamber shapes. While the prevailing literature extensively explores bending properties, it has largely overlooked the significance of chamber shapes in the interaction dynamics between the endoscope and the soft actuator [11], [12], [24]. Given the integral role these interactions play in determining bending properties, response properties, and stiffness adjustability—the latter being optimized by a bilateral symmetrical air chamber design—it is imperative to investigate the influence of chamber shapes on these interactions.

1.3.2 Stiffness Modulation in Multi-DoF Soft Actuator

- **The importance of Stiffness Modulation**

A key feature of soft actuators is their ability to modulate stiffness based on the specific demands of the surgical environment. This adaptability allows the actuator to conform to surrounding biological structures, enhancing both safety and efficacy. Enhanced stiffness offers the resistance needed to counteract external loads from organs or tissues, ensuring stable control of integrated surgical instruments. Reduced stiffness, however, enables navigation through unstructured or sensitive areas, allowing the actuator to navigate tight spaces or delicate tissues without causing undue stress or damage. [20], [21].

- **Related Research and Challenge in Stiffness Modulation**

Various design and innovative methodologies have been explored to achieve adjustable stiffness [12], [27], [28]. Among these, shape memory alloy (SMA)-based actuators can modulate the stiffness of flexible endoscopes during operation, countering external pressures from surrounding organs, thus improving maneuverability and maintaining a steady surgical view in MIS [27], [28]. However, incorporating SMAs into soft actuators can lead to increased size and weight, potentially reducing the space available for the hollow central duct, which is used for inserting surgical instruments. This reduction may limit size and require larger incisions. Additionally, the need for heat or electrical energy to activate SMAs poses concerns regarding safety and practicality.

Pneumatic soft actuators with antagonistic chambers have been employed to enable stiffness modulation without requiring additional equipment [21], [29].

- **Challenge in Stiffness Modulation of Multi-DoF Soft Actuator**

However, few studies have examined stiffness modulation in multi-DoF and multi-sectional contexts [12], [29]. Compared to antagonistic structures that incorporate rigid components [30], pneumatic antagonistic chambers undergo substantial deformation, causing notable changes in the internal stress distribution of the structure [15], [16], [19]. In actuators with a hollow central duct designed for inserting surgical instruments in single-port surgery, inflating multiple antagonistic chambers introduces complexities into internal stress distribution and the structure of the hollow central duct. These complexities make it difficult to predict the impact of inflation on stiffness modulation. Direct measurement of internal stresses may provide a better understanding of the structural changes within pneumatic soft actuators during the inflation of antagonistic chambers; however, measuring these stresses presents significant challenge and may be overlooked. FEA allows for the examination of internal stresses and structural changes in soft actuators [20], [31], [32], particularly regarding their bending properties and performance metrics [33], [34], [35], [36]. However, limited studies have explored their application, especially concerning stiffness modulation in soft actuators.

1.3.3 Load Sensing and Stiffness Adjustment for Soft Actuator in MIS

- **Related Research and Challenge in Sensors for Soft Actuator in MIS**

To select an appropriate stiffness, estimating the external load is essential [18], [37]. However, conventional load sensors are unsuitable for pneumatic soft actuators because embedding them directly impacts the actuator's omnidirectional compliance [38]. Instead, researchers have turned their attention to soft sensors made of compliant materials, which can be easily integrated with soft actuators due to their high compliance [39], [40], [41]. These soft-load sensors measure and model changes in electrical properties, such as resistance or capacitance, in response to material stress and strain changes. However, manufacturing these actuator-sensor combinations presents significant challenge. Incorrect sensor placement can easily damage the actuator and cause leaks [38]. Furthermore, many soft sensors are limited to specific conditions, such as those involving magnetic or bright light sources [42].

Recently, there has been growing interest in soft actuators embedded with sensing mechanisms [43], [44], [45], [46]. These actuators incorporate sensing layers or units, such as fiber embroidery [43], thin biphasic metal films [44], conductive working fluids [45], or wires [46], within their structure. Analytical models for monitoring the actuator’s movement or load are based on mechanical or electrical principles. For example, a soft pneumatic actuator with self-sensing of external load was reported in [44], requiring the embedding of a sensing layer in the soft actuator, a difficult fabrication process. The sensing mechanism relies on an analytical model of the relative change in resistance and load. While this mechanism is highly sensitive and suitable for measuring dynamic signals

such as vibrations or impact forces, it cannot measure static external loads needed to determine stiffness.

- **Related Research and Challenge in self-sensing for Soft Actuator in MIS**

Developing an accurate analytical model for self-sensing in MIS is particularly challenging. In MIS support scenarios, the characteristics of the actuator (bending, stiffness, deformation) change when different flexible endoscopes are inserted into a pneumatic soft actuator, necessitating adjustments to the analytical model. Additionally, when a flexible endoscope is inserted into a pneumatic soft actuator and bent, internal interference occurs between the endoscope and the actuator. This interference is complex, making the effect of the endoscope on the actuator's characteristics equally complex. For instance, the overall stiffness of the pneumatic soft actuator and flexible endoscope could change with the bending angle, and this relationship is nonlinear. Therefore, creating an accurate analytical model for a pneumatic soft actuator with an inserted flexible endoscope is challenging.

Given these challenge, neural networks (NNs) are necessary to adaptively acquire the model, as NNs are effectively applied for modeling nonlinearity and uncertainty [47], [48]. A self-sensing approach based on NNs has been proposed, as NNs can approximate functions with great precision. This method does not rely on independent or embedded physical sensors but uses the relationship between target physical quantities and a set of state variables directly or indirectly affected by or interacting with these quantities. This relationship can be learned from the collected raw data of a soft actuator [47].

A NN-based self-sensing method for bending angle and contact force was proposed and implemented for a 3D printed pneumatic soft actuator [38]. After training, the NN could predict the bending angle and contact force using air pressure values. However, while the NN accurately predicted cases similar to the training samples, it generated significantly deviated predictions for real test samples. This discrepancy arises from the nonlinearity of the soft actuating system and the uncertainty of the interaction between the soft actuator and its environment, rather than the learning capability of the NNs [48]. This issue is common in real-world robotic applications [47].

1.4. Purpose of study

The primary objective of this Ph.D. project was to provide design insights and solutions to address the problems in stiffness-modulating multi-DoF pneumatic soft actuators for complex MIS (refer to Section 1.3, Problem Statement). To achieve this, the following goals were identified, each addressing a specific problem:

1. Complex interaction between surgical instrument and soft actuator (Chapter 2): Central to our study is the interaction between the soft actuator and endoscope, a dynamic that is fundamental for enhancing the efficiency and safety of MIS procedures. Our study aimed to understand how the design of these cross-sectional pneumatic chambers can affect the interaction and critical attributes, such as bending properties, response properties, and stiffness adjustability, which in turn influence the maneuverability [49] and control of soft actuators.

2. Stiffness Modulation in Multi-DoF Soft Actuator (Chapter 3): We aimed to understand the mechanism of stiffness modulation in Multi-DoF soft actuator with multiple antagonistic chambers by constructing, validating, and analyzing an FEA simulation model of a soft actuator used in complex MIS.
3. Load Sensing and Stiffness Adjustment for Soft Actuator in MIS (Chapter 4): We aimed to propose a NN-based load active-sensing scheme and stiffness adjustment for a MIS-support pneumatic soft actuator with antagonistic chambers for soft actuator.
4. Preliminary master-slave Framework (Chapter 5): We also aimed to devise a preliminary master-slave framework for our designed stiffness-modulating multi-DoF pneumatic soft actuators used in MIS, to validate the practical relevance of our research and confirm the actuator's potential to enhance surgical precision and safety.

1.5. Limitation

In this Ph.D. project, while providing design insights and solutions to address the problems in stiffness-modulating multi-DoF pneumatic soft actuators for complex MIS (refer to Section 1.3, Problem Statement), we encountered several limitations, which can be summarized as follows

1. Complex interaction between surgical instrument and soft actuator
   - ① Inter-chamber interference: The potential interference between multiple antagonistic air-chamber pairs has not been fully explored.
   - ② Endoscope dimensions and shape: Our study did not extensively investigate the impact of varying the external diameters and shapes of the inserted endoscopes on the actuator performance.
   - ③ Frictional consistency: While friction has been identified as a key factor, the consistency of friction over prolonged use and under varied conditions remains uncharted.

2 Stiffness Modulation in Multi-DoF Soft Actuator
   - ① Discrepancy in Stiffness Prediction: Our current FEA model exhibits limitations in accurately simulating the stiffness of the soft actuator under high-load conditions, showing discrepancies between predicted and experimentally observed stiffness values. This limitation restricts our ability to precisely predict and control stiffness.
   - ② Limited Scope of Practical Testing: While we have conducted preliminary tests in a physical simulator to approximate real-world conditions, these experiments fall short of fully validating the stiffness modulation functionality in actual surgical scenarios. Such scenarios are complex and vary significantly, necessitating extensive validation to ensure the practical applicability and reliability of the actuator in clinical settings.

3 Load Sensing and Stiffness Adjustment for Soft Actuator in MIS
   - ① Limited Directions of Active-Sensing Scheme: The current active-sensing scheme is limited in scope, as it does not adequately cover different directions of multi-DoF soft actuators.

② Lack of Closed-Loop Feedback Controller: The absence of a closed-loop feedback controller for achieving the desired angle and stiffness restricts precise control, limiting the actuator's performance and versatility.

1.6. Contribution

The significant contributions of this Ph.D. project can be summarized as follows:

1. Our study elucidated the role of cross-sectional shapes in pneumatic chambers, revealing their influence on the bending properties, response dynamics, and stiffness adjustability of soft actuators. The study also emphasized the pivotal role of frictional forces stemming from chamber interactions as a key determinant of actuator performance. Furthermore, our findings underscore the delicate balance between actuator design nuances and resultant operational performance. In the MIS, this research highlights the potential for heightened surgical precision, emphasizing the need for designs that augment patient safety and procedural efficiency. Finally, the study serves as a crucial reference for future innovations in soft actuator design and applications as MIS technology continues to evolve. (Chapter 2)
2. This study also elucidated the mechanism of stiffness modulation in multiple antagonistic chambers by constructing an FEA simulation model for soft actuators used in single-port transvesical prostatectomy. The model examined the effects of stress distribution across the hollow center duct structure of a soft actuator on stiffness modulation. This methodological approach enhances our understanding of the mechanical behavior of actuators for precise stiffness modulation and advances the design of soft actuators for complex MIS. Furthermore, the study assessed the impacts of different stiffness modulation strategies on key performance metrics of the soft actuator, including tip-bending angle, response dynamics, and tip force. (Chapter 3)
3. We addressed the challenge of inaccurate predictions in existing studies [47] by proposing a load active-sensing scheme and an environment exploration strategy to optimize the instantaneous load estimation from a NN. By investigating the optimal exploration sequence, the estimation error was reduced to less than 0.01N, and the successful estimation rate increased to 80%. This method not only helps surgeons select suitable stiffness levels for soft actuators based on accurate external load predictions but also provides engineers with reliable signals for designing improved feedback controllers. Furthermore, an inverse dynamics model for stiffness was proposed, enabling surgeons to easily adjust the stiffness to resist varying external loads and maintain a stable surgical view during MIS procedures. This model offers a valuable foundation for future research into stiffness or impedance control of soft actuators. (Chapter 4)
4. We devised a preliminary master-slave framework to validate the practical relevance of our research. Initial surgical simulations highlighted the potential of the actuator, demonstrating its ability to enhance surgical precision and safety in MIS such as transvesical prostatectomy. (Chapter 5)

1.7. Thesis Structure

Chapter 2 explores the complex interaction between the soft actuator and surgical instruments, specifically focusing on how cross-sectional pneumatic chamber designs influence bending properties, response dynamics, and stiffness adjustability, ultimately impacting the maneuverability and control of soft actuators. In Chapter 3, the mechanism of stiffness modulation in Multi-DoF soft actuators is examined through the construction, validation, and analysis of a FEA simulation model. Chapter 4 introduces a neural network-based load active-sensing scheme and stiffness adjustment method for MIS-support pneumatic soft actuators with antagonistic chambers. Chapter 5 presents a preliminary master-slave framework to validate the practical relevance of the research, confirming the potential of our actuator to improve surgical precision and safety in MIS. Finally, Chapter 6 provides a comprehensive discussion of the research results and contributions, offers conclusions, and outlines potential directions for future research.

2. Chamber Shapes Influence Soft Actuators

2.1. Preface

Chapter 2 delves into the impact of cross-sectional pneumatic chamber designs on the interaction between soft actuators and endoscopes, significantly influencing actuator performance. We elucidate the profound effects of chamber shapes on bending properties, response dynamics, and stiffness adjustability, identifying frictional forces as a pivotal factor in actuator functionality. Our findings underscore the necessity for design enhancements to improve surgical precision and ensure patient safety. Portions of this chapter were previously published in the journal article titled 'Effects of Chamber Shapes on Maneuverability and Control Property of Endoscope-Support Soft Actuators,' contributing substantially to ongoing innovations in soft actuator design for minimally invasive surgeries (MIS).

2.2. Introduction

In minimally invasive surgery (MIS), the integration of soft actuators with soft surgical instruments like endoscopes is advantageous due to their compact size, low hardness, and bidirectional bending capabilities [12]. This integration aims to reduce the stiffness of internal instruments during procedures and prevent relative sliding, thereby ensuring stable functionality. Despite these benefits, current designs have several limitations: they have not yet been implemented in actual surgeries, cannot accommodate conventional endoscopes, are costly, and lack adaptability for various surgical scenarios [12].

An alternative method for using soft actuators in MIS is to employ them as bidirectional bending access channels for instruments [17]. These actuators feature broad internal channels that can hold both surgical instruments and endoscopes, facilitating interactions between the two. By increasing degrees of freedom (DoF) and range of motion, soft actuators allow MIS to access difficult body areas, ensuring safe navigation among organs.

Companies like Ambu Inc. and Olympus Corp. have developed flexible soft endoscopes with a single DoF for lens rotation and an access channel for surgical tools, which are used in procedures such as thoracoabdominal and bladder surgeries. However, their limited DoF restricts maneuverability in complex surgeries like transcystic resection of the prostate [13], which requires precise navigation, posture maintenance, and surgical operations. The necessity for multiple DoF is clear. Furthermore, these endoscopes cannot adjust stiffness according to surgical conditions, reducing stability and increasing operational challenge. Enhancing their DoF involves complex and costly modifications to their mechanical and control systems, affecting reliability and usability. Soft actuators used as bidirectional bending access channels for MIS instruments [17] can complement these endoscopes by improving DoF and range of motion for more procedures.

Determining the material properties of soft actuators, specifically those used as bidirectional bending access channels for MIS instruments, is challenging. These actuators are often made from elastomeric materials like silicone rubbers, with a shore hardness of 10-30A [19]. In contrast, mainstream endoscopes from companies like Ambu Inc. and

Olympus Corp. are made of stiffer materials to prevent damage, ensure water resistance, and transmit signals, resulting in an overall stiffness of around 50A. This significant difference in material properties can create challenge during interaction. Factors such as contact surface area, endoscope stiffness, and friction are crucial determinants. Friction affects the actuator's bending and response properties [12] and can cause relative sliding between components due to stiffness disparity, leading to actuation delays and influencing other key actuator properties.

The necessity for soft actuators to adjust stiffness to maintain a stable surgical view in dynamic environments is crucial. A bilateral symmetrical air chamber design has been recognized as an effective solution, supported by research [21], [29]. This design ensures real-time adaptability and is noted for its efficiency and practicality. It's important to emphasize that interactions between the endoscope and soft actuator, due to differences in material properties, might influence stiffness adjustability, an area that requires further exploration.

The design of soft actuators must consider the specific constraints imposed by the MIS environment and equipment. The size and materials of MIS instruments are inherently limited, particularly regarding the outer and inner diameters and materials of the actuator. These constraints highlight the importance of another key component: the cross-sectional chamber. Among various influential variables, the shape of the chamber is crucial in modulating the interaction between the actuator and the endoscope, thus affecting the overall performance of the actuator-endoscope system. Previous studies [11], [17], [22], [23], [24] have examined the effects of different chamber shapes, such as circular [17], [22], rectangular [17], semicircular [24], [25], and fake crescent [24], [26], on the bending properties of soft actuators. However, the broader implications for enhancing the navigational process of endoscopes during MIS [17] remain unknown.

A notable gap exists in our holistic understanding of the broad implications of these chamber shapes. While the prevailing literature extensively explores bending properties, it has largely overlooked the significance of chamber shapes in the interaction dynamics between the endoscope and the soft actuator [11], [12], [24]. These interactions are crucial in determining bending properties, response properties, and stiffness adjustability—the latter optimized by a bilateral symmetrical air chamber design. Therefore, it is imperative to investigate the influence of chamber shapes on these interactions.

Moreover, the influence of chamber shape, especially during endoscope insertion, on response properties and stiffness adjustability remains underexplored. Addressing this knowledge gap is crucial and opens an avenue to amplify the benefits of innovations like the bilateral symmetrical air chamber design. A more comprehensive exploration of chamber shapes could clarify their impact on both response properties and stiffness adjustability, ultimately enhancing the maneuverability and control of endoscopic instruments in MIS scenarios.

Central to our study is the interaction between the soft actuator and endoscope, a dynamic crucial for enhancing the efficiency and safety of MIS procedures. Our research aimed to understand how the design of cross-sectional pneumatic chambers affects critical attributes such as bending properties, response properties, and stiffness adjustability, which influence the maneuverability and control of endoscope-supporting soft actuators [49].

Specifically, we focused on optimizing multi-DoF control of the endoscope by designing a soft actuator. Our goal was to refine control over the existing DoF to ensure a more effective range of motion. This nuanced approach seeks to elevate the functionality of both individual soft actuators and the composite endoscope-soft actuator system. By delving deeper into the mechanisms of interaction, we envision significant potential in broadening design parameters and enhancing the response and stiffness adaptability of soft actuators. This approach distinguishes our research from conventional studies, offering a unique perspective. To further emphasize this distinctiveness and provide a clear understanding of how our research advances the field, we have included a comparison table (Table 2.1) juxtaposing key aspects of this research with previous related studies.

Table 2.1 Proposed Study vs. Previous Studies

Features	Proposed Study	Previous Studies	References
Focus	Interaction dynamics between pneumatic chamber designs and endoscope-soft actuator systems, with an emphasis on friction as a pivotal factor.	Primarily focused on bending characteristics and basic functionality of soft actuators.	[12]; [17]; [22];
Design Innovation	Bilateral symmetrical air chamber design with hollow spaces, optimized for integrating with clinical endoscopes and enhancing maneuverability.	Traditional designs emphasizing limited functionality, lacking integrated space for endoscopes.	[17]
Chamber Shapes	Extensive exploration of seven diverse chamber shapes to determine their impact on actuator performance and identify optimal designs for specific surgical needs.	Focus on limited chamber shapes, neglecting the potential of diverse designs to enhance actuator functionality and surgical efficiency.	[Proposed Study]; [24]; [25];
Objective	Enhancing bending property, response property, and stiffness adjustability in soft actuators for improved the maneuverability and control property of endoscope.	Focus on bending and physical properties of soft actuators.	[Proposed Study]; [49];

To elucidate our approach, we modeled endoscope-supporting soft actuators with a simplified structure and a single degree of freedom (DOF). A notable feature of our design is its innovative antagonistic structure that enhances stiffness adjustability. Specifically, our design includes bilateral symmetrical air chambers separated by hollow spaces. This hollow space serves a dual purpose: it provides a structural novelty and an insertion channel

for endoscopes and other surgical instruments. Unlike conventional antagonistic structures in soft actuators [29], where chambers are positioned adjacently without intervening space, our configuration minimizes interference between chambers due to spatial separation.

For a comprehensive study, finite element analysis (FEA) simulations were conducted to model seven distinct pneumatic chamber shapes: circular, semicircular, square, rectangular, fake crescent, long fake crescent, and crescent. FEA is a valuable tool in soft actuator research [26], [31], [32], [33], [35], [40], offering advantages such as cost-effectiveness, design flexibility, and predictive accuracy [34], [36], [50]. FEA provides in-depth insights into the internal structural dynamics of soft actuators during bending. It examines the effects of various parameters, including chamber shape, material properties, and boundary conditions, guiding the optimized design of soft actuators for medical robotics applications.

Through meticulous finite element analysis (FEA) and prototype testing, we investigated the interactions induced by different chamber shapes in soft actuators. Understanding these interactions and their influence on properties such as bending, response, and stiffness adjustability is essential for advancing the design of soft actuators for endoscopic applications.

Furthermore, our study revealed that friction plays a pivotal role in these interactions. Actuators with wider chamber widths generated larger frictional forces, enhancing component interactions. This increased friction improved bending properties, response properties, and stiffness adjustability. These findings underscore the critical importance of chamber shape and friction in design, suggesting new avenues for enhancing soft actuator performance in MIS applications.

2.3. Methods

2.3.1 Hypothesis

Our primary hypothesis suggests that friction forces at the interface between the actuator and the endoscope are pivotal for the performance of the actuator. Intuitively, one might expect that reducing friction would enhance performance by decreasing resistance; however, increased friction could also yield benefits. The actuator's control performance is intricately linked to its bending properties, which are influenced by the patterns of deformation induced by shape and the distribution of internal stress.

Building on this hypothesis, our experimental methods and analysis were designed to explore the complex relationships between the design nuances of soft actuators and their performance metrics.

2.3.2 Design for Soft Actuators

To enhance our understanding of the impact of chamber shapes on soft actuator performance, we broadened our study to include a more diverse array of chamber shapes compared to earlier research [11], [27]. Figure 2.1 illustrates the pneumatic chamber shapes we investigated: circular, square, fake crescent, semicircular, rectangular, long fake crescent, and crescent. The details of each chamber's parameters are provided in Table 2.2.

To ensure consistency, all chambers were designed with uniform cross-sectional areas and lengths. Each chamber's cross-sectional center was aligned with the midpoint of the outer wall of both the soft actuator and the endoscope tube.

Table 2.2 The parameters of soft actuator.

chamber name	S (mm^2)	W_c (mm)	W_t (mm)	H_c (mm)	L (mm)
circular	6.282 (2π)	2.828	6.000	2.828	100.000
semicircular	6.282 (2π)	4.000	6.000	2.000	100.000
square	6.282 (2π)	2.507	6.000	2.507	100.000
rectangular	6.282 (2π)	6.283	6.000	1.000	100.000
fake crescent	6.282 (2π)	3.107	6.000	2.000	100.000
crescent	6.282 (2π)	9.037	6.000	1.000	100.000

The soft actuator was comprised of two symmetrical pneumatic chambers, along with a strain-limiting fiber, and encased within a soft silicone body (radius: 8.25 mm, length: 120 mm). The endoscope was housed in a silicone tube (radius: 4.25 mm, length: 140 mm, thickness: 1 mm). The base of the actuator (radius: 8.25 mm, length: 20 mm) was fixed. This configuration of the silicone tube allows it to function as an end effector on a steerable catheter, enhancing the surgeon's ability to reach locations inaccessible to the endoscope alone. Additionally, a strain-limiting fiber (major radius: 8.65 mm, minor radius: 0.4 mm, axial pitch: 2 mm, 59 turns) with helical restraint was incorporated externally to further enhance functionality.

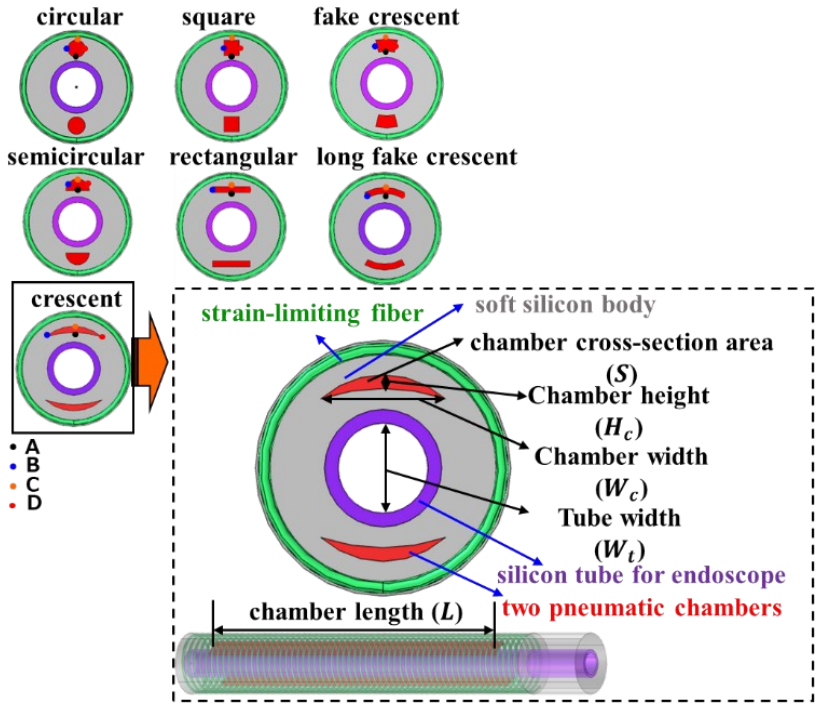

Figure 2.1 Investigated pneumatic chamber designs and parameters

2.3.3 FEA Modelling

A quasi-static numerical finite element model was developed using COMSOL Multiphysics 6.0® to investigate the effect of different cross-sectional shapes of pneumatic chambers on the bending and response properties of soft actuators. The modeling process is as follows:

- Modeling Software and Interface

The Solid Mechanics Interface of the Structural Mechanics Module in COMSOL Multiphysics 6.0® was used to model the soft actuators.

- Simulation Conditions

Boundary Load conditions were used to simulate the input air pressure, accurately representing the physical application of pressure within the pneumatic chambers during actual usage.

- Geometry and Parameters

The geometry of the numerical model is shown in Figure 1. The parameters of the soft actuator (Supplementary Material Table S2.1) were based on the designed geometry, with the only variation being the cross-sectional shape of the pneumatic chamber.

- Boundary Constraints

A fixed boundary constraint was applied to the terminal cylinder surface (radius: 8.5 mm, length: 20 mm) of the silicone body.

- Material Modeling

A third-order incompressible Yeoh model was used to model the hyperelastic silicone body. This model was chosen for its accessibility in the FEA software and its proven performance under high strains. The material parameters were determined using a nonlinear least-squares optimization method with the Levenberg-Marquardt algorithm by fitting the experimental data.

- Model Specifications

The strain energy density function (W_{siso}) of the Yeoh Model is presented as (2.1).

$$W_{siso} = c_1(\overline{I_1} - 3) + c_2(\overline{I_1} - 3)^2 + c_3(\overline{I_1} - 3)^3 \tag{2.1}$$

where I_1 denotes the strain invariant. The coefficients for Dragonskin 10 MEDIUM and Dragonskin 30 were implemented from the Soft Robotics Materials Database (Marechal et al., 2021) with the following values: $c_1 = 0.0547$ MPa, $c_{12} = 0.0002$ MPa, $c_3 = 0$ MPa for Dragonskin 10 MEDIUM and $c_1 = 0.1536$ MPa, $c_{12} = 0.0016$ MPa, $c_3 = 0$ MPa for Dragonskin 30. The densities of both materials were the same at 1070 $\mathrm{kg/m^3}$.

- Actuator and Fiber Modeling

The strain-limiting fiber (major radius: 8.65 mm, minor radius: 0.483 mm, axial pitch: 2 mm, 59 turns) with helix restraint was externally added to the actuator. Modeled as a linear elastic material, it had a Young's modulus of E=31067 MPa, a Poisson's ratio of υ=0.36, and a density of 1440 kg/m³. This fiber is crucial for limiting strain and emulating real-world operational conditions.

- Meshing Strategy

All actuator components were meshed using solid tetrahedral quadratic hybrid elements. For the thin-fiber windings, a combination of tetrahedral quadratic hybrid elements and quadratic beam elements was used to ensure precise representation of their physical characteristics.

2.3.4 Measurement in FEA Simulation

A series of FEA simulations were performed to investigate the bending behavior of all soft actuators with different cross-sectional shapes of the pneumatic chambers using the COMSOL Multiphysics software. Simulations were conducted for each soft actuator with only one pneumatic chamber, and the pressure loads were varied in the range of 0-200 kPa. The measurement method for the soft actuator in the FEA simulations is shown in Figure 2.2(a).

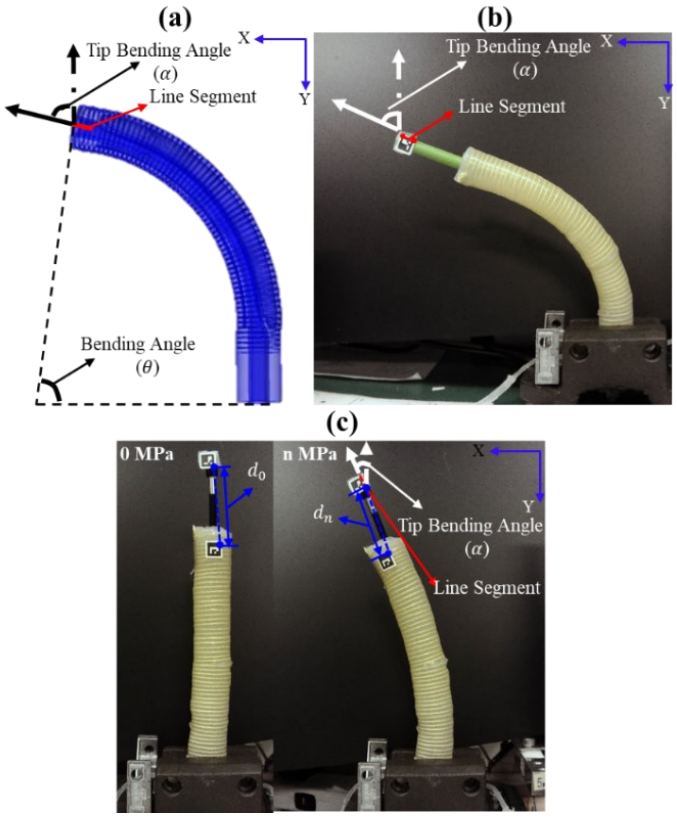

Figure 2.2 Assessment of soft actuator (a) with FEA simulations (b) for free bending (c) and for bending with inserted endoscope

The tip bending angle (α) of all soft actuators was determined from the results of the deformed shape at each pressure. To analyze the influence of different cross-sectional shapes of pneumatic chambers on the tip bending angle (α), the change ratios of chamber length R_L, chamber width (R_w), chamber height (R_H), and chamber cross-sectional area (S_c) were measured at all pressures. These ratios were defined by equation (2.2).

$$R_L(n) = \frac{L(n) - L(0)}{L(0)} \times 100\%, R_w(n) = \frac{w_c(n) - w_c(0)}{w_c(n)} \times 100\%,$$
$$R_H(n) = \frac{H_c(n) - H_c(0)}{H_c(n)} \times 100\%, R_C(n) = \frac{s_c(n) - s_c(0)}{s_c(n)} \times 100\% \quad (2.2)$$

L is the chamber length, w_c is the chamber width, H_c is the chamber height, S: the cross-sectional area of the chamber, and n is the air pressure.

Tube widths (W_t) were measured at various pressures. At the same time, we also measured the stress distribution of the cross-sectional of each soft actuator.

A previous study reported that the bending angle is proportional to the increased volume of the chamber (ΔV), as shown by (2.3) [35].

$$\alpha \propto \Delta V \quad (2.3)$$

2.3.5 Measurement of Free Bending in Prototype Experiments

To confirm the results from the FEA simulations, we conducted prototype experiments to assess the bending characteristics of soft actuators with different pneumatic chamber shapes (circular, rectangular, long fake crescent, and crescent) under various pressure conditions. The soft actuators were fabricated using molds printed with a 3D-printer (Ultimaker 2 Extended+, Ultimaker B.V., Netherlands) using PLA filament. Dragonskin 10 MEDIUM (Smooth-On, Inc., US) was used to fabricate the main bodies of the soft actuators. Dragonskin 10 MEDIUM consisted of two parts mixed together at a 50:50 mass ratio. The mixture was subjected to vacuum for 15 min to de-air and then slowly poured into appropriate molds. Dragonskin 10 MEDIUM was used as the final coating to fix the strain-limiting fibers (Kevlar thread; major radius:8.65 mm, minor radius,0.483 mm; axial pitch,2 mm; number of turns,59; CS Hyde Co., USA) with helix restraint. A silicon tube (major radius:4 mm; minor radius:3 mm; Dragonskin 30, Smooth-On, Inc., US) was placed in the middle of the soft actuators. The experimental measurement technique is illustrated in Figure 2.2(b).

For precise measurement of the tip bending angle of each actuator, a cylinder (radius: 3.25 mm, length: 45 mm) was placed atop each actuator. The actuators were arranged vertically, and an ArUco marker was attached to the top of the cylinder. The bending event was recorded using a camera (USB8MP02G-SFV, ELP camera, Ailipu Technology Co., Ltd., CN), and the tip bending angle was determined by employing two-dimensional marker detection with OpenCV and Python 3.8.12, defined by two points on the right-hand side of the image. To ensure safety, the air pressure input was capped at 200 kPa.

2.3.6 Measurement of Free Bending in Prototype Experiments

The bending properties and relative sliding between the soft actuators (circular, rectangular, long fake crescent, and crescent) and the endoscope (radius: 3.9/2 mm, hardness: 80A, Sanko, JP) were assessed through prototype experiments. To evaluate the effects of relative sliding and mutual interference during insertion, a measurement method was developed, as shown in Figure 2.2(c). Two ArUco markers were placed at the top of the soft actuator and endoscope, and the apparatus was held vertically. The measurement procedure was identical to that used for free bending in the prototype experiments. The sliding distance (d_s) is defined by equation (2.4).

$$d_s = d_n - d_0 \tag{2.4}$$

where d_n is the distance between the tip of the soft actuator and the tip of the endoscope at n kPa, d_0 is the distance between the tip of the soft actuator and the tip of the endoscope at 0 kPa.

Building on the hypothesis that highlights friction's impact on actuator performance, we conducted an experiment to investigate its effects. We applied a lubricant (CaineZero® Jelly, Fujifilm Corp, JP) to minimize friction between the outer wall of the endoscope and the inner wall of the tube. We then compared the bending properties under conditions of high friction (without lubricant) and low friction (with lubricant). The experimental setup for measuring bending properties, control performance, and stiffness adjustability of the soft actuator was consistent with that described in the prototype experiments.

Further, to explore the hypothesis that chamber shape affects actuator control performance, we evaluated soft actuators with various cross-sectional shapes (circular, rectangular, long fake crescent, and crescent) using typical Proportional Integral Differential (PID) controllers. Control gains were determined through trial and error to achieve no overshoot and quick recovery. The control settings for the circular, fake crescent, long fake crescent, and crescent soft actuators were P = 0.220, I = 0.130, D = 0.100; P = 0.200, I = 0.105, D = 0.100; P = 0.150, I = 0.140, D = 0.100; and P = 0.100, I = 0.107, D = 0.100, respectively. We set the target angle at 30° with a maximum input air pressure of 200 kPa for all actuators. Control was executed using an Arduino UNO (Arduino Uno Rev3, ARDUINO CC., USA) with an SMC ITV0030-2ML air pressure regulator (SMC

Pneumatics Ltd., UK), adjusting air pressure from 0 kPa to 200 kPa. Angular position and velocity were captured at 100 Hz using an Adafruit BNO055 nine-axis sensor. The discrepancy between the actual and desired angles was input into the PID controller to adjust the air pressure. We also measured the maximum bending angle using identical PID parameters across all actuator designs.

To assess stiffness adjustability, we set three target angles for the actuators (0°, 45°, and 90°) and applied varying weights (0.2N, 0.4N, 0.6N, 0.8N, 1N, Tokyo Garasu Kikai Co., Ltd., JP) atop the circular, rectangular, long fake crescent, and crescent actuators to simulate different loads. For a target angle of 0°, equal air pressure was applied on both sides of the chamber to increase stiffness. For target angles of 45° and 90°, the opposite chamber was subjected to 30 kPa, while the bending chamber received 0-200 kPa to achieve the specified angle. Consistent with the friction conditions set in our bending property experiments, we also examined the effects of friction on stiffness adjustability at a 0° angle to further understand how friction influences the stiffness adjustability of soft actuators.

2.3.7 Test for the Soft Actuator in the Bladder Model with the Flexible Endoscope

The practicality and operability of the soft actuators were evaluated using a bladder model into which a flexible endoscope (Ambu® aScopeTM 4 Broncho Slim 3.8/a1.2, Ambu Inc., DK) was inserted (as shown in Figure 2.3(a)). The bending of the soft actuators (circular, fake crescent, long fake crescent, and crescent) was managed using a controller (Logitec Extreme3D Pro, Logicool Co. Ltd., JP). For comparative purposes, additional tests were conducted using only the flexible endoscope without any soft actuators (illustrated in Figure 2.3(b)). The bladder model was crafted from Dragonskin 10 MEDIUM (Smooth-On, Inc., US), and a square paper was positioned in the upper part of the prostate model to assess the maximum surgical area accessible by all soft actuators. Additionally, to further evaluate the practicality and operability of the soft actuator with a crescent cross-sectional pneumatic chamber, a target surgical area labeled "L, A, R" was designated on the bladder model (shown in Figure 2.3(c)). Three individuals without prior experience in developing soft robots and controllers participated in the experiments to verify the practicality and operability of the soft actuator and controller system.

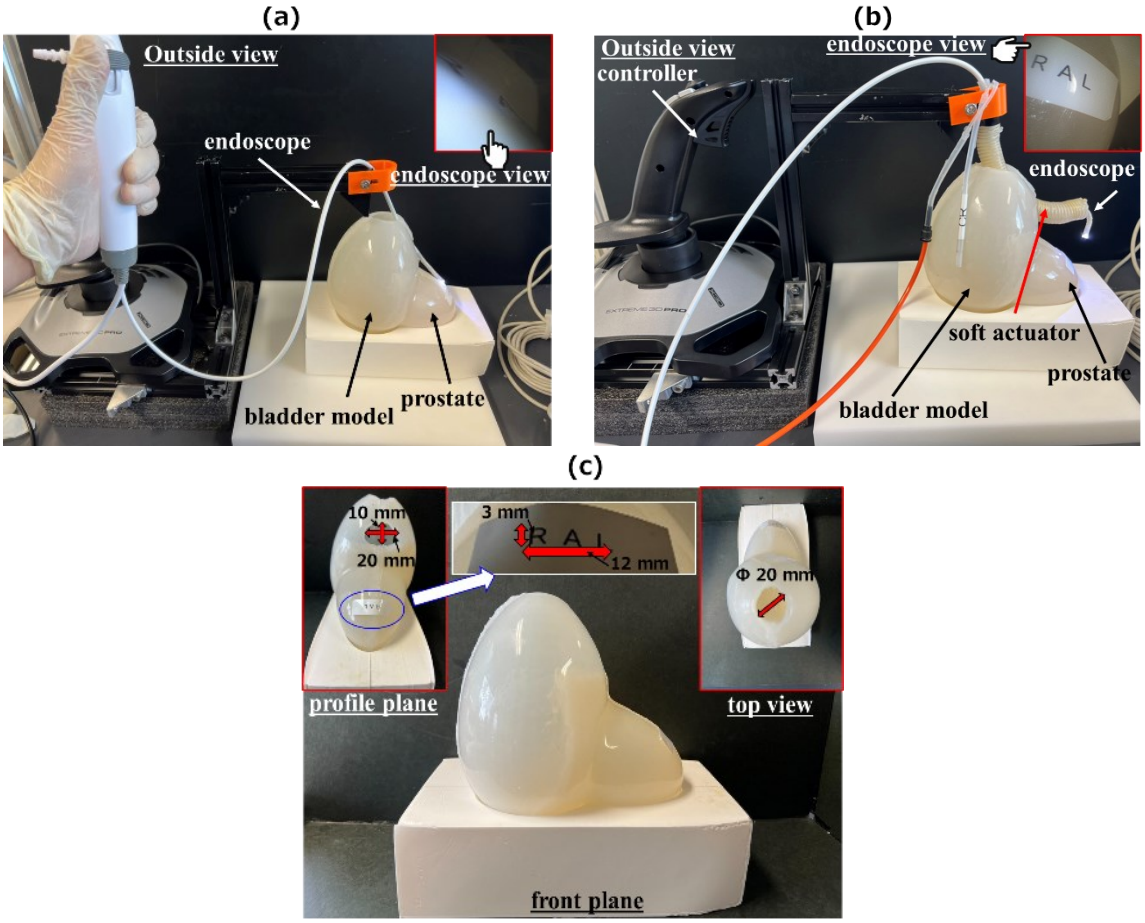

Figure 2.3 (a) Image of testing for flexible endoscope without soft actuator in bladder model (b) Image of testing for soft actuator when inserting flexible endoscope in bladder model (c) Image of bladder model

2.4. Results

2.4.1 FEA Simulations

This research explored how tip bending angles vary under different air pressures across a range of pneumatic chamber shapes, including circular, semicircular, square, rectangular, fake crescent, long fake crescent, and crescent. As illustrated in Figure 2.4(a), the soft actuator with a crescent cross-section demonstrated the greatest tip bending angle. The sequence of bending angles from highest to lowest was: crescent >> rectangular > long fake crescent >> semicircular > fake crescent > square > circular. These results indicate that the cross-sectional shape has a significant impact on bending performance.

The hollow design used for inserting the endoscope led to significant expansion of the pneumatic chamber on the hollow side. As depicted in Figure 2.4(d), tube widths in the middle of each soft actuator's chamber expanded at air pressures ranging from 0 to 110 kPa, with the crescent-shaped chamber showing the largest increase in tube width.

Stress distribution across the cross-section of all soft actuators at air pressures of 80 kPa and 110 kPa is shown in Figure 2.4(e). The findings identified a low-stress region at the bottom of each chamber, most notably within the crescent-shaped chamber which displayed the broadest low-stress area. To explore the impact of low stress on the change in tip bending angle ($\Delta\theta$), stress measurements were taken at points A, B, C, and D (referenced in Figure 2.1) of the inflated chambers at various tip bending angles and are documented in the Figure S2.5. The data demonstrated that a wider chamber width (rectangular, long fake crescent, and crescent) correlated with reduced stress at point A, while a circular chamber experienced higher stress at points A, B, C, and D compared to other soft actuators at equivalent tip bending angles.

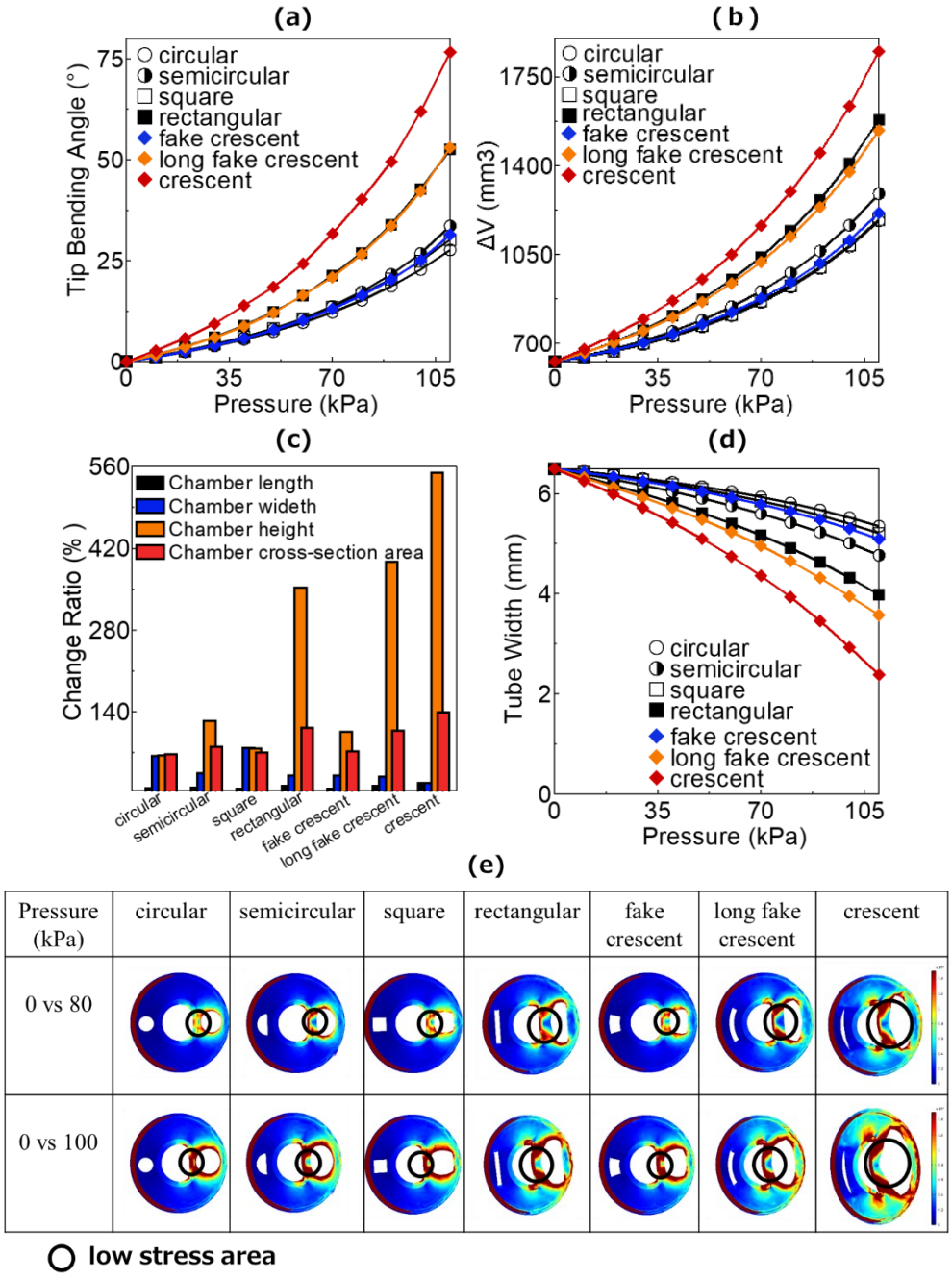

Figure 2.4 (a) The variation of tip bending angle under 110 kPa (b) The variation of ΔV under 110 kPa (c) Change ratio at 110 kPa (d) The variation of tube width under 110 kPa (e) The stress distribution of cross-section of all soft actuator at 80kPa and 110 kPa

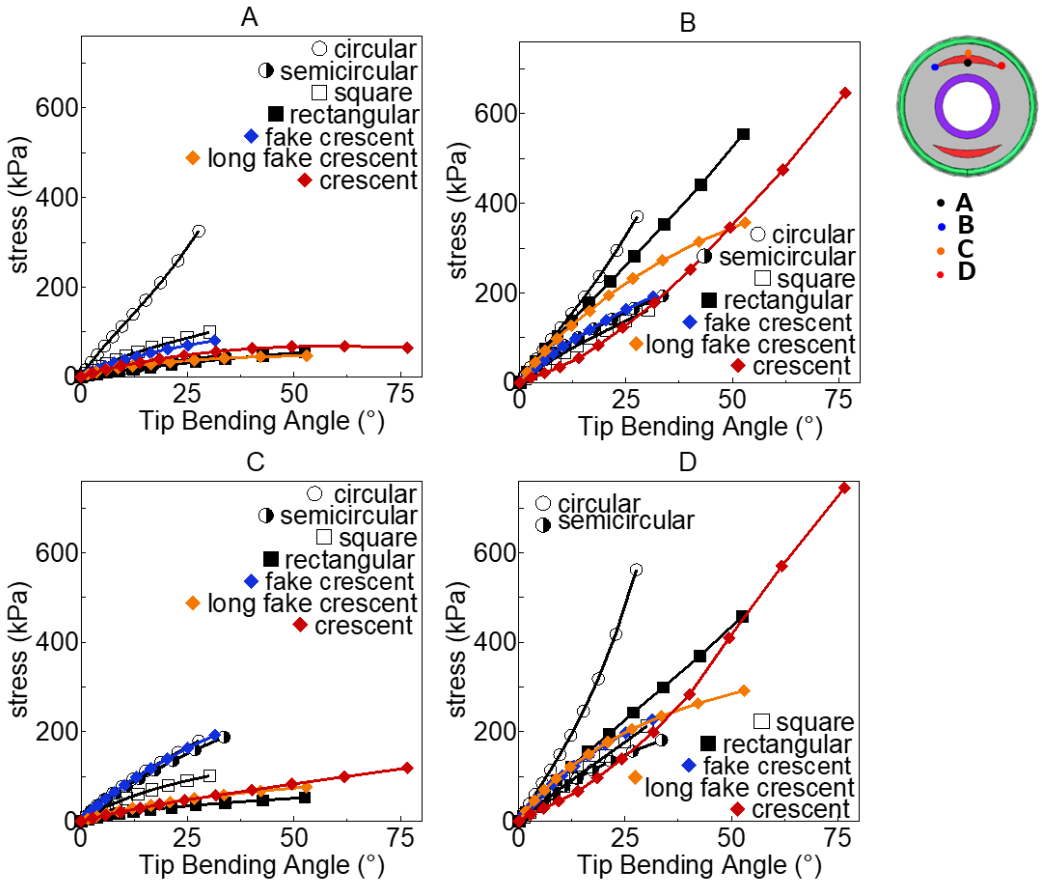

Figure 2.5 The variation of stress in A, B, C, D under different tip bending

2.4.2 Prototype Experiments for Free Bending

Four soft actuators with pneumatic chambers of differing cross-sectional shapes (circular, fake crescent, long fake crescent, and crescent) were selected for prototype testing based on tip bending angle results from the FEA simulations. A comparison of tip bending angle variations at 110 kPa between the simulations and prototype experiments is detailed in Figure 2.6. The crescent-shaped chamber demonstrated the largest tip bending angle, following the order: crescent > long fake crescent > fake crescent > circular. The bending performance observed in the prototype experiments aligned with the FEA simulations, validating their accuracy. However, the prototype experiments indicated more pronounced bending than the simulations predicted, likely due to the material properties listed in the Soft Robotics Materials Database [50] for the Yeoh model, a finding consistent with prior observations [50].

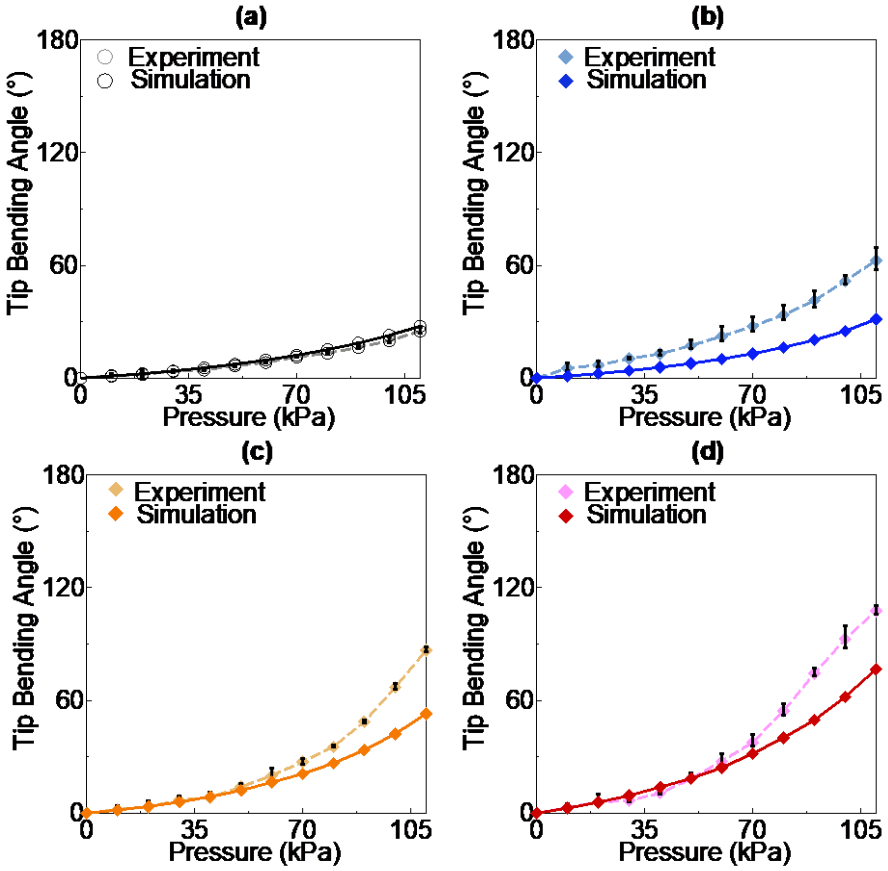

Figure 2.6 Air pressure variation of tip bending angle under 200 kPa on FEM simulations and Prototype experiments test for free bending angle (a)circular, (b)fake crescent, (c) long fake crescent, (d) crescent

2.4.3 Prototype Experiments for Bending Property, Control Performance, and Stiffness Adjustability of the Soft Actuator

Figure 2.7 illustrates the variation in tip bending angle of the endoscope when inserted into soft actuators with different chamber shapes—circular, rectangular, fake crescent, long fake crescent, and crescent—at 200 kPa in prototype experiments conducted under high- and low-friction conditions. The crescent-shaped chamber showed the largest tip bending angle of the endoscope (crescent > long fake crescent > fake crescent > circular), mirroring the results of free bending experiments.

Our hypothesis suggested that low-friction conditions would improve actuator deformation and bending properties due to decreased resistance from the endoscope. Conversely, we also explored the potential beneficial effects of increased friction on these properties. Our experimental results shed light on this distinction. As indicated in Figure 2.7, all soft actuators, regardless of chamber shape, exhibited more pronounced tip-bending angles under high-friction conditions than under low-friction conditions. This underscores the critical role of increased friction between the outer wall of the endoscope and the inner wall of the tube.

Moreover, Figure 2.8 demonstrates that the crescent-shaped chamber consistently had the shortest sliding distance under both high and low friction conditions. This suggests that maximizing friction can reduce sliding, thereby impacting the bending properties of the actuator. These observations support the initial assumptions stated in our hypotheses.

Figures 2.9(a) and (b) display the step responses of soft actuators with different cross-sectional chamber shapes (circular, rectangular, fake crescent, long fake crescent, and crescent) under conditions of free bending and endoscope insertion, managed by PID controllers. Table 2.3 lists the performance metrics and PID gains for each actuator. The chambers with broader widths, specifically the long fake crescent and crescent, showed faster response times in metrics like rise and settling times. The comparable response times between the crescent and long fake crescent chambers can be attributed to their similar widths.

Table 2.3 Performance characteristics and PID gains of soft actuators

	Without endoscope			With endoscope		
	$T_r(s)$	$T_d(s)$	$T_a(s)$	$T_r(s)$	$T_d(s)$	$T_a(s)$
Circular	6.111	2.061	8.443	6.382	2.828	8.773
Fake crescent	6.042	1.568	7.819	6.182	2.108	7.903
Long fake Crescent	3.882	1.540	5.374	4.021	1.954	5.815
Crescent	4.508	1.329	5.808	5.029	1.781	6.246

$T_r(s)$: rising time, $T_d(s)$: delay time, $T_a(s)$: settling time.

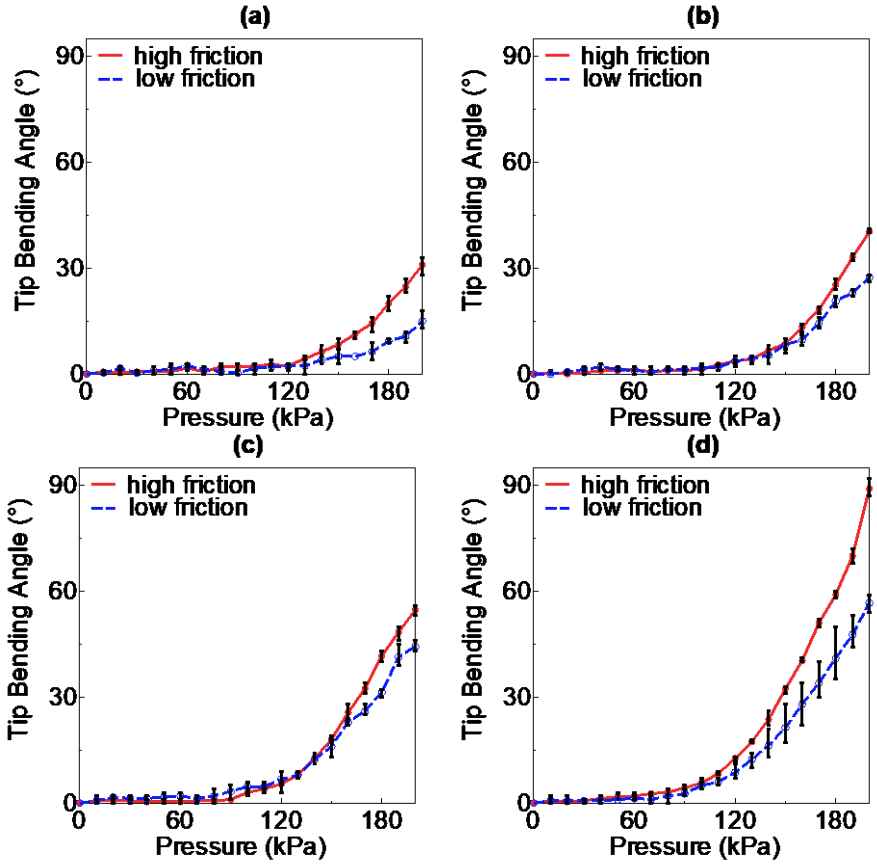

Figure 2.7 Air pressure variation of tip bending angle under 200 kPa when inserting endoscope on high friction and low friction with (a)circular, (b)fake crescent, (c) long fake crescent, (d) crescent

Our findings confirmed our hypothesis, illustrating the complex relationship between chamber shape and actuator performance. Specifically, the impact of chamber shape on control performance closely mirrored its influence on bending properties. This connection is further demonstrated by the deformation patterns and internal stress distribution shown in Figure 2.4(e).

Figure 2.10(a) displays the variation in stiffness adjustability under a load of 1 N. With the target angle set at 0°, only the actuators with crescent and long fake crescent chamber shapes were capable of supporting a 1 N load. As the target angle increased, the load-bearing capacity of all actuators diminished. The crescent-shaped actuator exhibited superior stiffness adjustability, managing to bend to all targeted angles (0°, 45°, and 90°) under a 0.6 N load. Further details from Figure 2.11 indicate that increased friction conditions enhance stiffness adjustability across all actuator chamber shapes: circular, rectangular, fake crescent, long fake crescent, and crescent. This emphasizes the critical role of friction in influencing actuator performance.

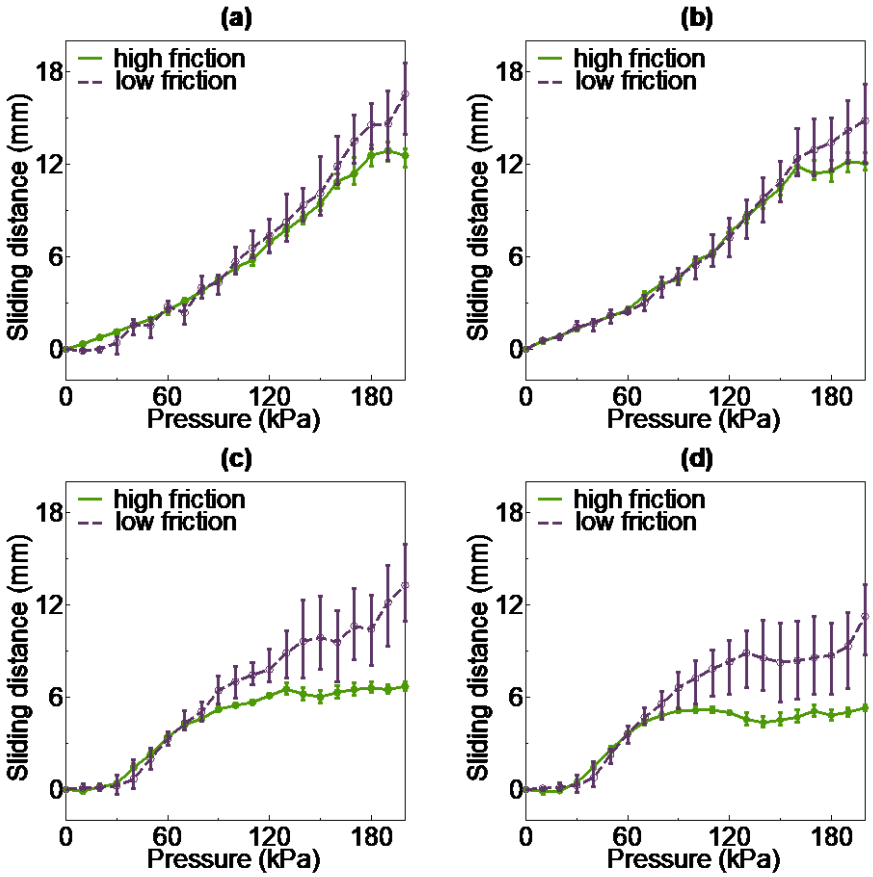

Figure 2.8 Air pressure variation of sliding distance under 200 kPa when inserting endoscope on high friction and low friction with (a)circular, (b)fake crescent, (c) long fake crescent, (d) crescent

To address the issue of unstable shaking observed in soft actuators, we increased the pressure in the opposite chamber to 30 kPa, which effectively enhanced stiffness as depicted in Figure 2.9(c). However, maintaining the opposite chamber at < 30 kPa did not eliminate the unstable shaking, and the prototype performance remained suboptimal. Further assessments on the maximum bending angle with respect to the PID controller parameters outlined in Table 2.2 are shown in Figure 2.9(b) for free bending. Only the actuator with the crescent-shaped chamber performed effectively at 50, 75, and 100 kPa under the specified PID controller settings. In contrast, the other actuators were unable to achieve the target bending angle without encountering issues like overshoot, steady-state errors, or prolonged settling times exceeding 10 seconds.

In experiments with the crescent chamber-shaped actuator, increasing the air pressure in the opposite chamber beyond 30 kPa reduced the maximum tip bending angle to 75°. Consequently, 75° was chosen as the target angle for subsequent tests, the outcomes of which are illustrated in Figure 2.10(b). To reduce the observed unstable shaking, we enhanced the stiffness of the soft actuators by raising the pressure in the opposite chamber to 30, 40, and 50 kPa. While this strategy stabilized the actuator, it increased the rising,

delay, and settling times by about 40% compared to tests conducted without the endoscope. However, pressures exceeding 50 kPa in the opposite chamber rendered the soft actuator uncontrollable with the existing PID controller settings.

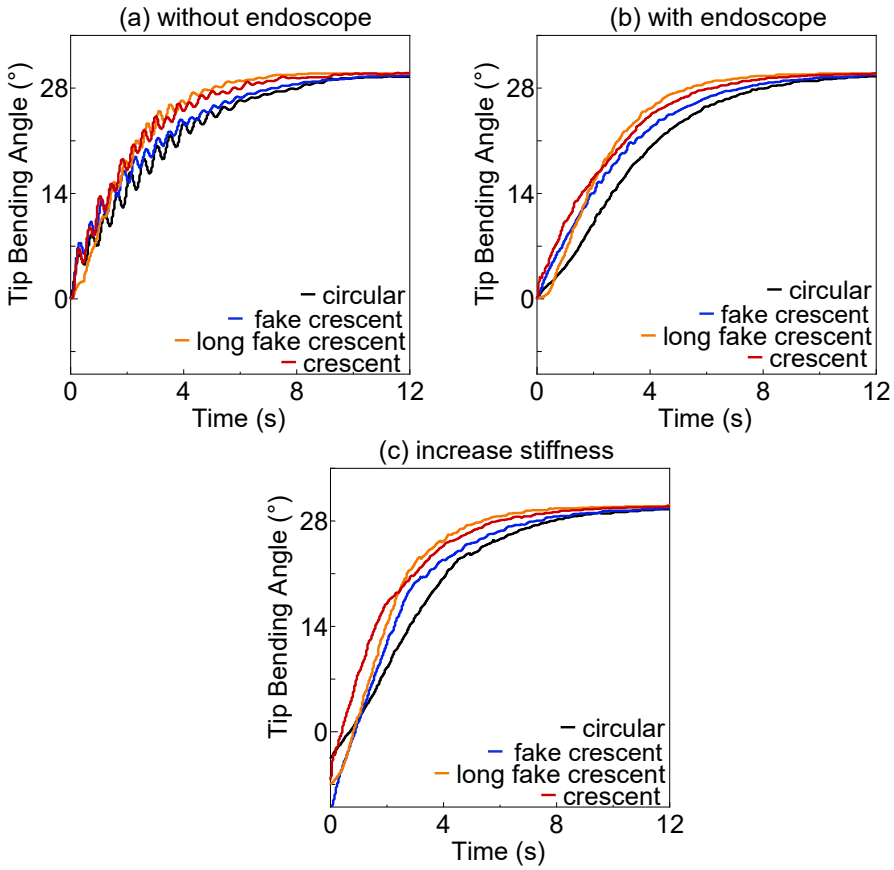

Figure 2.9 Performance of soft actuators with different pneumatic chamber (a) without endoscope (b) with endoscope (c) increase stiffness

For all soft actuators tested (circular, fake crescent, long fake crescent, and crescent), pressurizing the opposite chamber below 30 kPa failed to eliminate the issue of unstable shaking. However, the stability improved when the endoscope was inserted, due to increased stiffness, although this also caused an increase in the rising, delay, and settling times of the actuator. The timing issues intensified further when air pressure was applied to the opposite chamber during endoscope insertion. Applying more than 40 kPa in the opposite chamber hindered the soft actuator from achieving the target angle of 75°. Figure 2.10(c) illustrates the stress distribution of the crescent-shaped actuator at 80 kPa with various pressures in the opposite chamber. We observed that higher pressure in the opposite chamber decreased the tube width, leading to earlier contact between the tube and the endoscope, thereby limiting chamber expansion. Despite these adjustments, the low-stress area remained largely consistent with the conditions observed during free bending (Figure 2.4).

Figure 2.10(d) presents the surgical areas achievable by different soft actuators, with the crescent-shaped chamber providing the largest surgical area, which was six times greater than that provided by the endoscope alone. This indicates that such an actuator design can significantly enhance the maneuverability of an endoscope, providing a wider surgical field. These findings emphasize the critical role of chamber shape in influencing performance metrics and practical utility, enriching our understanding of how pneumatic chamber design impacts soft actuator performance.

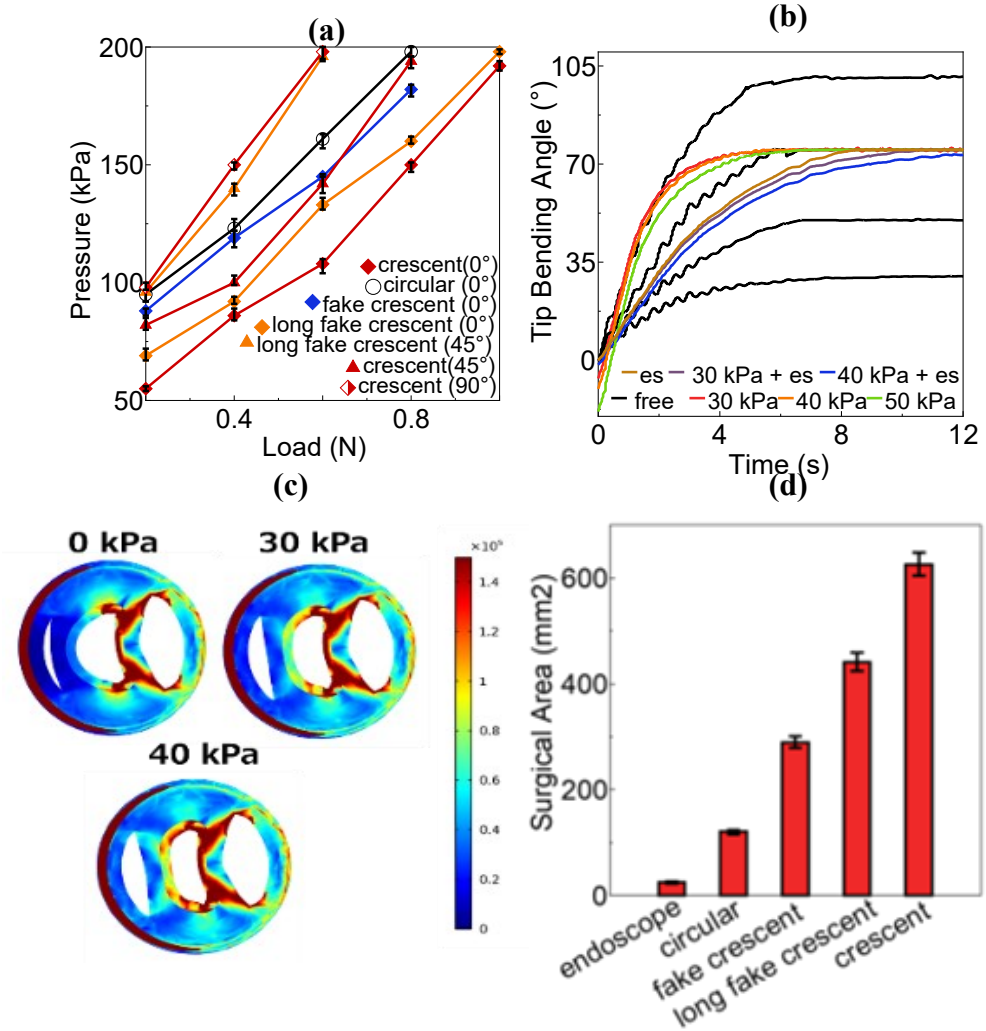

Figure 2.10 (a) The variation of stiffness adjustability under 1 N (b) Performance of soft actuators with crescent chamber (c) The stress distribution of cross-section of soft actuator with crescent chamber at 80 kPa (d) The surgical area for all soft actuators at 200 kPa

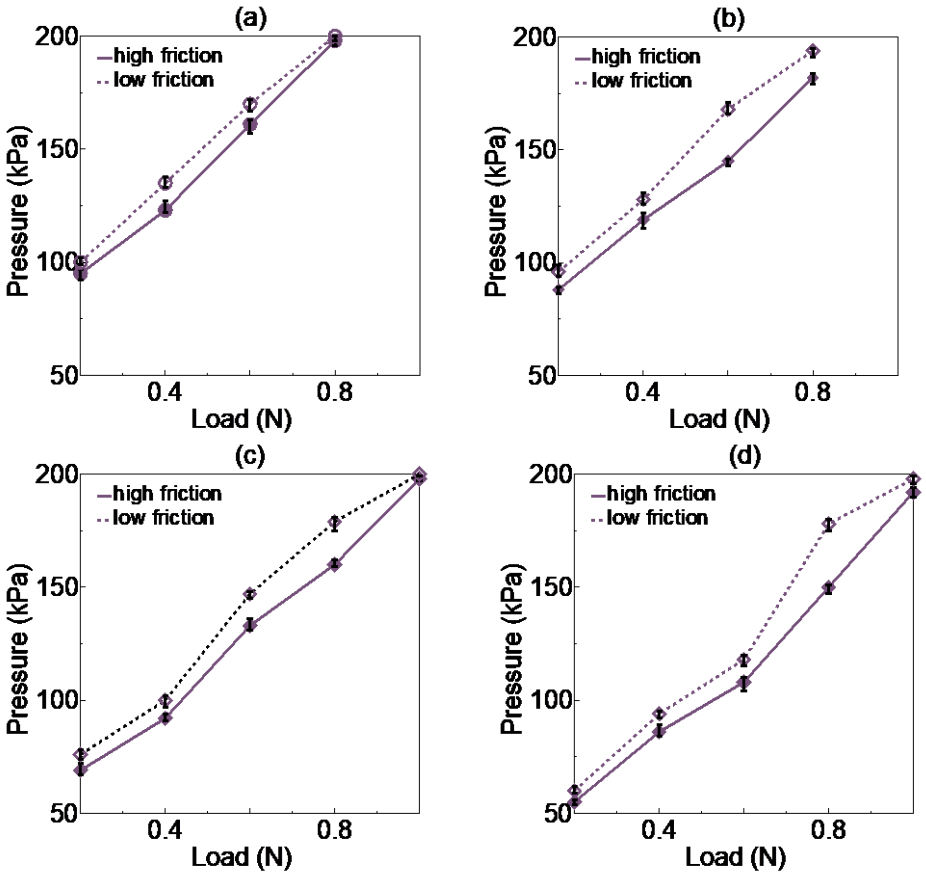

Figure 2.11 The variation of stiffness adjustability under at 0° with 1 N (a)circular, (b)fake crescent, (c) long fake crescent, (d) crescent

2.4.4 Prototype Experiment for the Soft Actuator in a Bladder Model with Flexible Endoscope

In the bladder model experiment, we evaluated the performance of a flexible endoscope both with and without the integration of a crescent-shaped chamber soft actuator. Operating the flexible endoscope alone proved challenging, yielding a limited view of only 5 mm × 5 mm of the target surgical area, where only "L, A" were visible. Conversely, when equipped with the crescent-shaped chamber actuator, the bronchoscope achieved over 90° of bend and exhibited an "S" shaped two-degree freedom, enhancing its inherent bending capabilities. This setup enabled rapid navigation over the prostate area (completed in 0.2 minutes by an inexperienced individual across 10 trials) and provided a stable, expansive view of the target surgical area (25 mm × 25 mm, displaying "L, A, R"). This configuration substantially improved the maneuverability and viewing range of the endoscope. The crescent-shaped chamber actuator offered a surgical field six times larger than that achievable with the endoscope alone.

2.5. Discussion

In our study on integrating endoscopes with soft actuators, we found that friction plays a pivotal role in the interaction between the soft actuator and the endoscope, significantly impacting actuator performance. Actuators with broader chamber widths, such as the crescent and long fake crescent designs, showed increased friction, which enhanced their functionality.

2.5.1 Bending Property

Our FEA simulations demonstrated that the crescent-shaped chamber achieved the most substantial tip bending angle (Figure 2.4(a)). For a target angle of 15°, while the circular chamber required about 80 kPa, the crescent-shaped chamber needed only 40 kPa, suggesting a potential 50% reduction in air pressure for the circular chamber, thus enhancing safety. The main factor behind the increased tip bending angle was the growth in chamber volume (ΔV), largely driven by the increase in the chamber's cross-sectional area (Figure 2.4(c)).

Moreover, the change in chamber height significantly exceeded the change in width (Figure 2.4(c)). This occurred because the hollow part was more susceptible to compression, causing the chamber to expand toward the hollow part of the soft actuator (tube) rather than outward and sideways, as the outer part was strongly reinforced by the nylon fiber. A broader chamber width resulted in a low-stress area in the direction of the hollow part (Figure 2.4(e)), facilitating the chamber's expansion towards the tube and increase in height while gaining a larger cross-sectional area. The crescent-shaped chamber, having the widest width, displayed the largest low-stress area and tip bending angle. Furthermore, the crescent chamber exhibited the lowest stress at points A, B, C, and D under a low tip-bending angle (Figure 2.5), indicating it is more conducive to rapid and significant deformations by air pressure than other chambers. In contrast, the soft actuator with a circular chamber showed the highest stress at these points at the same tip bending angle, indicating greater challenge in deforming rapidly and significantly under air pressure.

During bending, the endoscope experienced relative sliding with the soft actuator. Due to the endoscope's inherent stiffness, which surpasses that of the soft actuator, it resisted the bending motion. Consequently, the input air pressure in the inflated pneumatic chamber primarily elongated the chamber in the direction of the endoscope, leading to relative sliding rather than genuine bending.

Delving deeper into the design intricacies, a wider chamber width, as seen in the crescent-shaped soft actuator, facilitated a more pronounced expansion of the pneumatic chamber in the actuator's hollow region. This design results in increased contact pressure on the endoscope, intensifying the friction between the endoscope's outer wall and the tube's inner wall. Our friction tests, shown in Figure 2.9, confirm this observation, highlighting that increased friction can significantly reduce the sliding distance between the endoscope and the soft actuator. Essentially, heightened friction restricts the elongation of the inflatable chamber towards the endoscope, promoting greater expansion towards the hollow section, and thereby yielding a sharper tip bending angle of the endoscope.

However, this design efficiency comes with inherent challenge. Despite their effectiveness, crescent-shaped actuators tend to compress the tube (Figure 2.4(d) and (e)),

posing potential difficulties during surgical procedures that require frequent instrument changes. While lubricants or low-friction tubes might alleviate this issue, they could slightly compromise bending efficiency. Circular-chambered actuators, although possibly less effective in bending capability, may offer a balanced solution due to their structural attributes.

Our research investigates the influence of cross-sectional shapes of pneumatic chambers on the bending properties of soft actuators, a critical factor in enhancing the functionality of tools used in MIS. The findings demonstrate that crescent-shaped chambers exhibit improved bending properties and require lower operational air pressure, thereby increasing safety and efficiency in surgical settings. This observation aligns with established principles [31], underscoring the importance of actuator design in medical applications.

Additionally, our study highlights the role of friction in actuator performance, emphasizing the need to control the interaction between the actuator and the endoscope. This aspect of our research provides insights into material and design considerations for soft actuators, contributing to the broader field of soft robotics and surgical technology as discussed in previous works [33], [40]. By focusing on these specific design elements, our study enhances the understanding of how soft actuators can be optimized for MIS, advancing the development of more effective medical robotic tools.

2.5.2 Stiffness Adjustability

Second, in exploring stiffness adjustability, we found that bilateral symmetrical air chambers are essential in soft actuator design. These chambers optimize the design by enhancing stiffness adjustability, as demonstrated by the actuator with the crescent cross-sectional chamber (Figure 2.10(a)). This increased stiffness improves the actuator's resilience against external pressures and refines the PID controller's performance, as shown in Figures 2.9 and 2.10(b). This capability underscores the potential of these soft actuators to maintain a steady posture when deployed within the human body, demonstrating their invaluable utility in various surgical procedures.

Based on our findings, detailed in Figure 2.11, it is evident that friction plays a central role in the performance of soft actuators. Under high-friction conditions, soft actuators with various cross-sectional chamber shapes—circular, rectangular, fake crescent, long fake crescent, and crescent—demonstrated enhanced stiffness adjustability. Given the significance of these observations, future research should focus on effectively integrating frictional behavior into actuator design. This could involve refining the structural design of actuators, exploring materials with specific frictional properties, and devising control strategies that leverage frictional dynamics.

Although these findings highlight the potential of soft actuators, they introduce certain constraints. Notably, when the air pressure in the opposing chamber exceeded 30 kPa, the tip-bending angle of the soft actuator was reduced by over 25% compared to its performance during free bending. Additionally, there is a risk of chamber rupture due to the opposing air chamber encroaching on the internal tube spaces. During bending, the high internal pressure causes the air chambers on either side to exert forces against each other,

as shown in Figure 2.10(c). These insights are crucial for ensuring the safe and effective application of soft actuators in surgical environments.

In our study on soft actuators for MIS, we identified stiffness adjustability as a key factor influencing their performance and safety, aligning with current trends in soft robotics and surgical technology. The interaction dynamics between soft actuators and endoscopes, particularly regarding material stiffness and friction, are central to this finding. Echoing previous research [12], [19], we emphasize the critical role of material properties in these interactions. Furthermore, our introduction of bilateral symmetrical air chambers, supported by previous studies [21], [29], represents a significant advancement in enhancing stiffness adjustability. This design not only bolsters resilience against external pressures but also optimizes control performance, crucial for the efficacy and safety of soft actuators in surgical applications. Overall, our findings contribute to a deeper understanding of soft actuator design in MIS, underscoring the importance of integrating material and structural considerations for improved surgical outcomes.

2.5.3 Response property

As previously discussed, actuators with wider chambers, such as the crescent and long fake crescent designs, have significantly improved bending properties and frictional force. This improvement directly leads to faster response times, which are crucial in surgical applications.

Regarding the response properties, our empirical data (Table 2.2) reveal that a soft actuator with a crescent cross-sectional chamber shape is superior in terms of delay time and overall bending properties. Although the rising and settling times were marginally surpassed by the long fake crescent design, the overall performance of the crescent actuator was remarkable. Its stability, as illustrated in Figure 2.10(b), is a defining trait. The pronounced friction in this design ensures stable endoscope-tube interactions, substantially reducing the risk of overshoot.

At the other end of the spectrum, soft actuators with lower friction profiles, such as those with circular and fake crescent cross sections, present certain challenge. Their predisposition to increased sliding distances results in unstable interactions between the tube and endoscope. This instability not only leads to overshoot but also complicates the calibration of the PID controller to its optimal parameters. Furthermore, the bending capabilities of these low-friction actuators are somewhat constrained and often fall short when tasked with achieving more pronounced desired angles.

Our research elucidates the intricate interplay between chamber design, stiffness adjustability, and control properties of soft actuators. The crescent-chambered actuator offers improved stiffness and control, particularly when modulating the air pressure in the opposing chamber. Based on our data, as shown in Figure 2.10(b) and detailed in Table 2.4, there is a critical threshold for maintaining the air pressure in the opposing chamber between 30 and 50 kPa. Beyond this range, the efficacy of the PID controller is diminished.

Table 2.4 The performance characteristics and PID gains of the soft actuator with a crescent chamber

name	air pressure in the opposite chamber (kPa)	$T_r(s)$	$T_d(s)$	$T_a(s)$
Antag_0	0	4.497	1.967	5.200
Antag_30	30	2.513	0.960	3.514
Antag_40	40	2.634	1.000	3.594
Antag_50	50	3.074	1.040	4.358
endoscope (es)	0	5.640	2.400	6.810
Antag_30 + es	30	6.240	2.490	8.010
Antag_40 + es	40	7.560	2.640	9.660

$T_r(s)$: rising time, $T_d(s)$: delay time, $T_a(s)$: settling time.

For endoscopes with a radius exceeding 3.9/2 mm, increasing the air pressure above 30 kPa in the opposite chamber is not recommended. The primary concern is the risk of premature tube-endoscope contact due to heightened pressure. Such interactions can restrict the expansion of the inflated chamber, compromising both the tip's bending range and the PID controller's control capabilities.

Our study's exploration of soft actuators in MIS reveals crucial insights into the role of chamber design and frictional dynamics in enhancing response properties. We discovered that actuators with wider chambers, such as the crescent design, exhibit significantly improved bending properties and frictional forces, leading to faster and more reliable response times. This improvement is particularly significant in the precise and demanding environment of MIS, where the speed and accuracy of actuator response directly impact surgical outcomes.

These findings contribute to the evolving field of soft robotics in surgical technology and align with the broader pursuit of more effective and responsive surgical aids. The interplay between chamber design, frictional forces, and response characteristics underscores the importance of considering these factors in the development of next-generation soft robotic systems for MIS, reaffirming our study's relevance and contribution to the field.

It is evident that design intricacies and functional outcomes are intertwined. The chamber shape and frictional dynamics are paramount, emphasizing their role in optimizing soft actuators for MIS applications.

Finally, we observed that the soft actuator notably enhanced the maneuverability and bending radius of the endoscope, as evidenced in Figure 2.10(d). This improved freedom allows the endoscope to navigate around obstructions with ease, reducing the risk of potential organ damage due to collisions and ensuring a stable surgical view. These capabilities underscore the potential of soft actuators in facilitating more intricate MIS procedures.

2.5.4 Contribution

1. Exploration of Chamber Shapes: Our research emphasizes the significance of cross-sectional shapes in pneumatic chambers and their impact on the bending characteristics, response dynamics, and stiffness adjustability of soft actuators.

2. Focus on Frictional Forces: We highlight the crucial role of frictional forces arising from chamber interactions, which are vital in determining actuator performance.

3. Design and Performance Interplay: Our findings underline the intricate balance between the nuances of actuator design and their effects on operational performance.

4. Progress in MIS: The study accentuates the potential for enhanced surgical precision in minimally invasive surgery (MIS), stressing the importance of designs that boost patient safety and procedural efficiency.

2.5.5 Limitation and Future Work

1. Inter-chamber Interference: The possible interference among multiple antagonistic air chamber pairs has not been thoroughly investigated.

2. Endoscope Dimensions and Shape: Our research did not comprehensively examine how variations in the external diameters and shapes of the inserted endoscopes affect actuator performance.

3. Frictional Consistency: Although identified as a critical factor, the consistency of frictional forces over extended use and under various conditions has yet to be explored.

2.6. Conclusion

While the significance of chamber design in soft actuators for MIS is well acknowledged, our findings uncover an unexpected benefit. A wider chamber width not only affects interactions with the endoscope but also amplifies pressing and friction forces, improving the range of motion and precision for maneuvering endoscopic instruments.

Among the designs evaluated, the soft actuator featuring a crescent-shaped chamber stood out. Its substantial chamber width coupled with a bilateral symmetrical air chamber configuration yields excellent bending and response capabilities without compromising patient safety. The adjustable stiffness of this design provides flexibility, making it applicable to diverse surgical procedures.

These insights refine our understanding of crucial factors in designing endoscope-supporting soft actuators and will guide future research. The next phase involves animal testing to further evaluate the practical utility of endoscopes paired with crescent-shaped soft actuators. We anticipate that our continued research will underscore the potential advantages of soft actuators in advancing MIS techniques.

3. Stiffness Modulation in Multi-DoF Soft Actuator

3.1. Preface

Chapter 3 investigates the mechanisms of stiffness modulation within multi-DoF soft actuators under the specific conditions of single-port MIS, where the hollow central passage significantly influences the internal stress distribution during the inflation of multiple antagonistic chambers. This chapter presents the construction, validation, and analysis of a Finite Element Analysis (FEA) simulation model to elucidate how inflating specific chambers generates bending moments, affects deformation responses to external loads, and modifies the actuator's stiffness. Our findings further detail how this inflation process impacts the bending moment and geometrical moment of inertia and alters the tensile and compressive regions within the hollow central passage, further influencing the actuator's stiffness. This research is currently under review and is being prepared for publication under the title "Stiffness Modulation in 3-DoF Pneumatic Soft Actuator for Single-Port Transvesical Prostatectomy," slated for May 2024.

3.2. Introduction

A key feature of soft actuators is their ability to modulate stiffness based on the specific demands of the surgical environment. This adaptability allows the actuator to conform to surrounding biological structures, enhancing both safety and efficacy. Enhanced stiffness offers the resistance needed to counteract external loads from organs or tissues, ensuring stable control of integrated surgical instruments. Reduced stiffness, however, enables navigation through unstructured or sensitive areas, allowing the actuator to navigate tight spaces or delicate tissues without causing undue stress or damage. [20], [21]. Various design and innovative methodologies have been explored to achieve adjustable stiffness [12], [27], [28]. Among these, shape memory alloy (SMA)-based actuators can modulate the stiffness of flexible endoscopes during operation, countering external pressures from surrounding organs, thus improving maneuverability and maintaining a steady surgical view in MIS [27], [28]. However, incorporating SMAs into soft actuators can lead to increased size and weight, potentially reducing the space available for the hollow central duct, which is used for inserting surgical instruments. This reduction may limit size and require larger incisions. Additionally, the need for heat or electrical energy to activate SMAs poses concerns regarding safety and practicality.

Pneumatic soft actuators with antagonistic chambers have been employed to enable stiffness modulation without requiring additional equipment [21], [29]. However, few studies have examined stiffness modulation in multi-DoF and multi-sectional contexts [12], [29]. Compared to antagonistic structures that incorporate rigid components [30], pneumatic antagonistic chambers undergo substantial deformation, causing notable changes in the internal stress distribution of the structure [20], [21], [29]. In actuators with a hollow central duct designed for inserting surgical instruments in single-port surgery, inflating multiple antagonistic chambers introduces complexities into internal stress distribution and the structure of the hollow central duct. These complexities make it difficult to predict the impact of inflation on stiffness modulation. Direct measurement of internal stresses may provide a better understanding of the structural changes within

pneumatic soft actuators during the inflation of antagonistic chambers; however, measuring these stresses presents significant challenge and may be overlooked. Finite element analysis (FEA) allows for the examination of internal stresses and structural changes in soft actuators [20], [31], [32], particularly regarding their bending properties and performance metrics [33], [34], [35], [36]. However, limited studies have explored their application, especially concerning stiffness modulation in soft actuators.

We aimed to understand the mechanism of stiffness modulation in multiple antagonistic chambers by constructing, validating, and analyzing an FEA simulation model of a soft actuator used in single-port transvesical prostatectomy [51]. The soft actuator consists of three antagonistic pairs within its three-sectional, hollow-centered body, necessitating a detailed exploration of stiffness modulation in complex structures. We conducted stiffness modulation experiments using both the simulation model and a prototype to cross-validate and investigate the effects of various antagonistic chambers on stiffness modulation. This involved identifying effective configurations for enhanced and reduced stiffness scenarios. A central hypothesis of our study is that the stress distribution within the multiple antagonistic chambers, along with the hollow central duct structure, significantly influences stiffness modulation. These factors and their combinations were the key focus of the FEA simulation model analysis. Additionally, we explored how effective stiffness modulation affects critical traits of soft actuators, such as tip bending/force and time response [12], [20]. Moreover, we confirmed the perturbation-resisting properties of various configurations on stiffness modulation within the bladder–prostate model for single-port transvesical prostatectomy.

3.3. Materials and Methods

In this section, we describe the structural design and fabrication of the soft actuator, which is essential for our prototype experiments and the development of the FEA simulation model. We the discuss the stiffness evaluation conducted through FEA simulations and prototype experiments, focusing on the performance of the actuator (i.e., tip bending/force and time response). Additionally, we examined the perturbation-resisting properties of stiffness modulation in the bladder–prostate model.

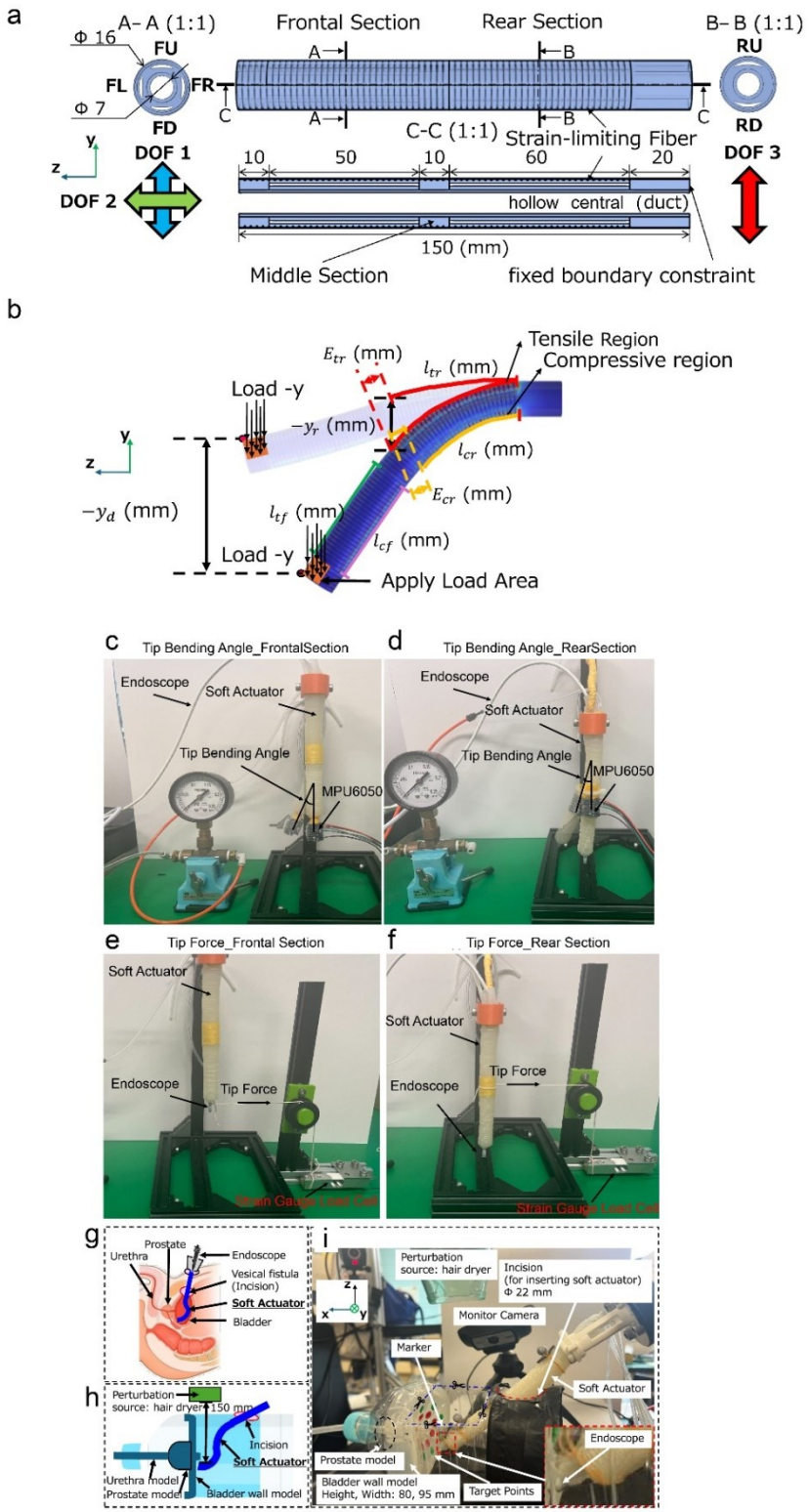

Figure 3.1 (a) Structural Design and Parameterization of 3-DoF Pneumatic Soft Actuator, (b) FEA Simulation Setup for Investigating 3-DoF Pneumatic Soft Actuator, (c-f) Experimental Setup for Evaluating: (c) Tip Bending Angle Frontal Section, (d) Tip Bending Angle Rear Section, (e) Tip Force Frontal Section, (f) Tip Force Rear Section, (g)

Schematic of Single-Port Transvesical Prostatectomy, (h) Schematic of Perturbation Resistance Experiment in Bladder–Prostate Model, and (i) Photograph of Perturbation Resistance Experiment Setup in Bladder–Prostate Model

3.3.1 Structure and Fabrication for Soft Actuator in Prototype Experiments

We constructed and fabricated a 3-DoF pneumatic soft actuator for transvesical prostatectomy support [51] to investigate stiffness modulation. Figure 3.1(a) illustrates the structure and parameters of the soft actuator, which contains six air chambers: frontal up (FU), frontal down (FD), frontal left (FL), frontal right (FR), rear up (RU), and rear down (RD). The frontal section, comprising four symmetrical pneumatic chambers, contains two pairs of antagonistic mechanisms (FU-FD and FL-FR), providing two DoFs. This design was tailored to support surgical operations in transvesical prostatectomy, including probing, suturing, and stripping. The rear section, with two symmetrical pneumatic chambers (RU-RD), exhibits a singular antagonistic mechanism, offering an additional degree of freedom. This part was primarily designed for tasks such as bending and securing MIS instruments in the bladder during transvesical prostatectomy. The middle section connects the front and rear sections. We set the center point of cross-section of pneumatic chamber to align with the center of outer wall of soft actuator and hollow central area (duct) (radius: 4.5 mm, length: 150 mm, thickness: 1 mm) for the MIS instruments. A strain-limiting fiber (radius: 0.4 mm, axial pitch: 1 mm, number of turns: 70) with a round restraint was added externally.

The main body of the soft actuator was constructed using Dragonskin 10 MEDIUM (Smooth-On, Inc., US). Dragonskin 10 MEDIUM was applied as the final coating to secure the strain-limiting fibers. A silicon duct made of Dragonskin 30 (Smooth-On, Inc., US) was centrally positioned within the soft actuator to accommodate the MIS instruments. The fabrication methodology adopted aligned with that used in our previous studies [20], [21].

3.3.2 FEA Simulation Model for Soft Actuator

In this study, we used FEA to investigate the adaptive mechanics and stiffness modulation of soft actuators with multiple antagonistic air-chamber pairs.

- Actuator Geometry

The design of the actuator featured a silicone body with an inner diameter of 7 mm, an outer diameter of 16 mm, and a total length of 150 mm, as illustrated in Figure 3.1(a). The soft actuator was modeled using the solid mechanics interface of the structural mechanics module in COMSOL Multiphysics 6.0®.

- Actuator Materials

The materials used in the actuator were Dragonskin 10 MEDIUM and Dragonskin 30, as described in the soft robotics materials database [50]. Their properties were defined using the Yeoh model coefficients: $c_1 = 0.0547$ MPa, $c_2 = 0.0002$ MPa, for $c_3 = 0$ MPa, and for Dragonskin 10 MEDIUM, and $c_1 = 0.1536$ MPa, $c_2 = 0.0016$ MPa, and $c_3 = 0$ MPa for Dragonskin 30. Both materials had a density of 1070 $\mathrm{kg/m^3}$. The strain-limiting fiber

within the actuator was modeled using a linear elastic material with a Young's modulus of $E = 31067$ MPa, a Poisson's ratio of $\upsilon = 0.36$, and a density of 1440 $\mathrm{kg/m^3}$.

- Physics of Model

In our simulations conducted with COMSOL Multiphysics 6.0®, the physics of the model were set to emulate the hyperelastic behavior of the silicone body using a third-order incompressible Yeoh model. The parameters for this model were obtained using a nonlinear least-squares optimization method. The strain energy density function (W_{siso}) of the Yeoh model is defined by Equation (3.1):

$$W_{siso} = c_1(\overline{I_1} - 3) + c_2(\overline{I_1} - 3)^2 + c_3(\overline{I_1} - 3)^3 \tag{3.1}$$

where I_1 is the first moment of inertia.

- Boundary Conditions

Boundary load conditions were applied to simulate the input air pressure. Additionally, a fixed boundary constraint was set on the terminal cylindrical surface of the silicone body.

- Mesh and Computation Time Consideration

The meshing and computation times for the simulation were carefully optimized to balance accuracy and computational efficiency. To reduce computational demand, a symmetry constraint was applied. The mesh, composed of tetrahedral elements, was constructed using the default fine-sized mesh settings in the software [52].

3.3.3 Stiffness Evaluation Experiment Via FEA Simulation

To determine the effective configurations for both enhanced and reduced stiffness of the soft actuator, we systematically evaluated the stiffness of each combination derived from inflating the six chambers, resulting in 64 unique combinations. When one chamber was inflated, a pressure of 30 kPa was applied. The specific setup of the experiment is illustrated in Figure 3.1(b), where l_{tr} and l_{cr} represent the lengths of the tensile and compressive regions in the rear section, respectively. Additionally, E_{tr} and E_{cr} denote the extensions in the lengths of the tensile and compressive regions in the frontal section. Upon achieving the desired inflation, a load ranging from 0 to 0.2 N was uniformly applied to the upper surface of the soft actuator, targeting an area of 261.3 $\mathrm{mm^2}$. This area, precisely calculated using COMSOL Multiphysics, corresponds to a segment of the surface of the actuator where no air chambers are inflated, ensuring a consistent application of the load directly along the negative y-direction. This setup, based on the simulation's parameters, facilitates reproducibility and reliability by closely adhering to the designed structural responses of the actuator, allowing for an accurate assessment of stiffness modulation under controlled load conditions. The resulting deflection ($-y_d$), oriented in the negative *y*-direction, was quantified under varying load -*y* conditions. The overall stiffness (K_d) of the soft actuator was then computed in the -*y*-direction using Equation (3.2).

$$K_d = \frac{-y\ load}{-y_d} \tag{3.2}$$

We employed Spearman's correlation analysis [53] to assess the relationship between individual air-chamber inflations and the resulting deflection in the negative y-direction ($-y\ deflection$) of the soft actuator. This analysis was chosen for its effectiveness in identifying the strength and direction of a monotonic relationship between ranked variables without assuming linearity. Through this approach, we aimed to discern the effects of variations in air-chamber inflation on changes in actuator stiffness by examining deflection as a proxy measure. We analyzed data from five load conditions (0.04, 0.08, 0.12, 0.16, and 0.20 N) across 64 unique combinations of air-chamber inflations, resulting in 320 distinct experimental setups. Each setup, representing a different configuration of air-chamber inflation, was assessed for its corresponding deflection in the negative y-direction, totaling 320 data pairs of independent variables (combinations of load conditions and air-chamber configurations) and their associated deflections as dependent variables. These deflections were chosen owing to the inherent variability of stiffness in soft actuators—directly influenced by both the applied load and the resulting deformation of the actuator. This comprehensive dataset was used in Spearman's correlation analysis to discern the nonlinear associations between the ranked variables, providing insight into the complex interplay between air chamber inflation and changes in actuator stiffness.

To validate our hypothesis regarding the impact of stress distribution and the hollow central duct structure on stiffness (K_d), we used our FEA simulation model to examine the frontal, rear, and middle sections of the soft actuator. The cross sections at the center of these sections were analyzed under various inflation conditions to assess how these factors influence actuator stiffness. For a quantitative analysis of the relationship between stress distribution and K_d, we systematically measured stress at 12 specific points within the actuator, considering a range of external loads across 64 inflation scenarios. This approach allowed us to precisely evaluate the effects of different inflation states on stress patterns and the structural behavior of the hollow central duct, shedding light on their collective role in stiffness modulation.

3.3.4 Stiffness Evaluation via Prototype Experiments

During the experimental phase of the stiffness prototype, we focused on validating the FEA simulation results. This validation process assessed the consistency of stiffness modulation trends between simulation and prototype testing across eight selected configurations from a pool of 64 possible combinations. Our selection criteria for these configurations were based on their potential to exhibit a range of stiffness modulation capabilities, from enhanced to reduced stiffness.

The stiffness prototype experiments were conducted to evaluate the response of the soft actuator under different load conditions. In these experiments, we applied varying

loads of 0.12 N, 0.16 N, 0.22 N, 0.56 N, and 1.06 N to the soft actuator. These load levels were chosen to broadly represent the range of operational conditions the actuator might encounter [12]. Our FEA simulation model in COMSOL Multiphysics was optimized for soft actuator applications within a specific range of operational loads up to 0.2 N. This operational load limit is primarily due to the inherent complexities involved in simulating hyperelastic materials and the unique geometry of the actuator. Specifically, our actuator design incorporates flat, thin, crescent-shaped chambers, enhancing maneuverability and control as demonstrated in previous studies [20], and enabling larger air ducts while maintaining a small diameter of the soft actuator. These flat chambers (with a thickness = 1 mm), as illustrated in Figure 3.1(a), have sharply defined edges at their boundaries, complicating the mesh generation process and accurately predicting the material's response to the applied loads. Beyond a load of 0.2 N, the simulation's ability to capture the nonlinear behavior of these materials and the intricate actuator geometry decreases, leading to potential inaccuracies and computational complexities. These complexities often cause convergence difficulties, as the solver struggles to find a stable solution within a reasonable computational time [19]. Additionally, higher load levels can induce deformations and stress distributions that are outside the validated ranges of the material models used, further increasing the potential for simulation inaccuracies [19]. Nonetheless, the results from the stiffness prototype experiments under the 0.12 and 0.16 N load conditions were crucial in validating the accuracy and effectiveness of our FEA simulation model in predicting the stiffness of the actuator.

To further assess the predictive capability of the model and demonstrate its applicability to surgical scenarios, the prototype experiments were extended to higher loads (0.22 N, 0.56 N, and 1.06 N). This extension aimed not to validate the exact predictions of the model at these loads but to examine whether the observed trends in stiffness modulation under lower loads persist under increased loads. Demonstrating consistent behavior across various loads emphasizes the comprehensive utility of the model in capturing essential actuator dynamics and affirms its relevance for surgical applications.

Due to the practical limitations of the experimental setup, the loads were applied using weights, as depicted in Figure 3.1(b), rather than the idealized load application possible in the simulations. In our simulations, loads were applied in a highly controlled and uniformly distributed manner across the surface of the actuator, mirroring ideal conditions that maximized the accuracy of our predictions regarding stress distribution and actuator deformation. This contrasts with the prototype experiments, in which loads were applied using weights, resulting in line contacts. Although practical and reflective of real-world conditions, this method introduces variances in the distribution of forces across the actuator surface compared to the simulation. To measure the deflection of the actuator under these applied loads accurately, we used a motion-capture system (Mars 1.3 HW, Beijing NOKOV Science & Technology Co., Ltd., CN). Markers were placed on the actuator, allowing precise tracking and measurement of movements and deformations.

3.3.5 Assessment of Tip-Bending Angle, Time Response, and Tip Force in Soft Actuators

Building on our insights from the FEA simulation concerning effective air chamber pairs for both enhanced and reduced stiffness configurations, we initiated prototype experiments to assess the three primary performance metrics of the soft actuator:

- Tip-Bending Angle: This measures the ability of the actuator to navigate through constrained spaces and complex anatomical pathways.
- Time Response: This evaluates the adaptability of the actuator to dynamic conditions, demonstrating its real-time responsiveness and efficiency.
- Tip Force: This indicates the force exerted at the tip of the actuator, crucial for procedures requiring precise manipulation or force application.

All evaluations were performed using a flexible endoscope (Ambu® aScope™ 4 Broncho Slim, diameter: 3.8 mm) inserted into the soft actuator. This approach closely aligns our study with real-world clinical settings and serves as a robust benchmark for assessing the efficiency of soft actuators.

In our experimental setup, leveraging the results from previous stiffness modulation experiments, we first inflated specific chambers using effective stiffness configurations (no-inflation, enhanced stiffness, and reduced stiffness). Then, we selected the FD chamber as the primary actuator chamber for the frontal section, progressively increasing air pressure to induce tip bending and tip force in the soft actuator. We chose the RD chamber for the rear section with the same objectives. This approach allowed for a nuanced exploration of the effect of stiffness modulation on key performance metrics across tip bending/force and time responses.

The tip-bending angle was evaluated, as shown in Figures 3.1(c) and 3.1(d). The setup uses an Arduino UNO (Arduino Uno Rev3, ARDUINO CC., USA) as the main control unit. The air pressure, controlled by an SMC AW20-01BE-B (SMC Co., Ltd., JP), was varied in two phases: inflation from 0 to 180 kPa and deflation from 180 to 0 kPa. During these inflation and deflation phases, the tip-bending angles of both the frontal and rear sections were recorded at 100 Hz using an MPU6050 six-axis sensor.

For the time response, we used the same actuator and control setup to examine the response of the actuator to frequency-modulated air pressure variations. Over a 15-s duration, we systematically altered the frequency of air pressure variations within the chambers of the actuator, ranging from 0 to 0.5 Hz, while maintaining a maximum air pressure of 180 kPa. This allowed us to monitor the real-time impact of these frequency changes on air pressure and the resulting angular deviations in the frontal section of the soft actuator. By observing how the actuator responded to different frequencies of air pressure changes, we assessed its dynamic behavior and responsiveness.

Finally, for the assessment of the tip force, we followed the schematics shown in Figures 3.1(e) and 3.1(f). Measurements were taken during both the inflation (0-180 kPa) and deflation (180-0 kPa) processes. The tip forces of the frontal and rear sections were continuously recorded at 50 Hz using a dedicated strain-gauge load cell.

3.3.6 Perturbation-Resisting Experiment in Bladder–Prostate Model

To assess the impact of the stiffness configurations on the execution of the single-port transvesical prostatectomy (refer to Figure 3.1(g)), we designed and fabricated a bladder–prostate model for a prototype experiment (refer to Figures 3.1(h) and 3.1(i)). This model, fabricated from silicone material (Dragonskin 10 MEDIUM, Smooth-On, Inc., US), closely simulates the properties of the prostate and bladder. The soft actuator was introduced into this model through a designated circular opening, replicating the surgical entry point for instruments in a single-port MIS procedure, as shown in Figures 3.1(h) and 3.1(i). The actuator, secured to a robotic arm (myCobot 320-M5, Elephant Robotics Co. Ltd., CN), maintained a fixed position throughout the experiment.

Incorporating the results from previous stiffness evaluation experiments, we first inflated specific chambers using effective stiffness configurations (no-inflation, enhanced stiffness, and reduced stiffness). To simulate an external disturbance, a hair dryer (3 Ion Jet Hair Dryer, 1500 W, Yamada Denki Co., LTD., JP) was positioned 150 mm from the actuator and delivered a consistent airflow for 10 s to mimic a constant noise impact. As described earlier, an endoscope provides real-time visual feedback within the actuator (Figures 3.1(h) and 3.1(i)). Markers were placed on top of the soft actuator to monitor its deformation in the x-, y-, and z-directions under these conditions using the NOKOV motion-capture system. Additionally, a monitor camera (C390e, WEB camera, Logicool Co. Ltd., JP) was used to observe the actuator externally.

3.4. Results

3.4.1 FEA Simulation Results on Stiffness Modulation of Soft Actuators

In the FEA simulation comprising 64 unique combinations, the results showed that inflating the FD and RU chambers to 30 kPa was an effective strategy for enhancing the stiffness of the soft actuator. This strategy, referred to as enhanced stiffness in this study, is shown in Figure 3.2(a). Conversely, inflating the four chambers—FU, FL, FR, and RD—excluding FD and RU to 30 kPa was the most effective method for reducing the stiffness of the soft actuator (see reduced stiffness in Figure 3.2(a)). Across all combinations, a consistent trend was observed: as the load increased, so did the stiffness of the actuator.

Figure 3.2(a) displays the stiffness outcomes when each chamber was individually inflated to 30 kPa. These results were compared with a scenario in which all chambers were uninflated, referred to as the no-inflation configuration. The analysis revealed that individually inflating the FD and RU chambers resulted in greater stiffness than the "none inflation" condition, emphasizing their role in enhancing stiffness. In contrast, other chambers demonstrated decreased stiffness compared to the "none inflation" condition, indicating their contribution to stiffness reduction. The order of stiffness, from highest to lowest, was as follows: enhanced stiffness > FD > RU > no-inflation > FL=FR > FU > RD > reduced stiffness. However, the RU configuration displayed a unique pattern in its relative stiffness within the 0 to 0.12 N load range, diverging from behaviors noted under loads greater than 0.12 N. Furthermore, in stiffness prototype experiments conducted under high-load conditions (Figure 3.2(c)), the order of stiffness intensity across eight configurations remained consistent with both FEA simulation model predictions and stiffness prototype experiment results with low-load conditions (Figure 3.2(a)).

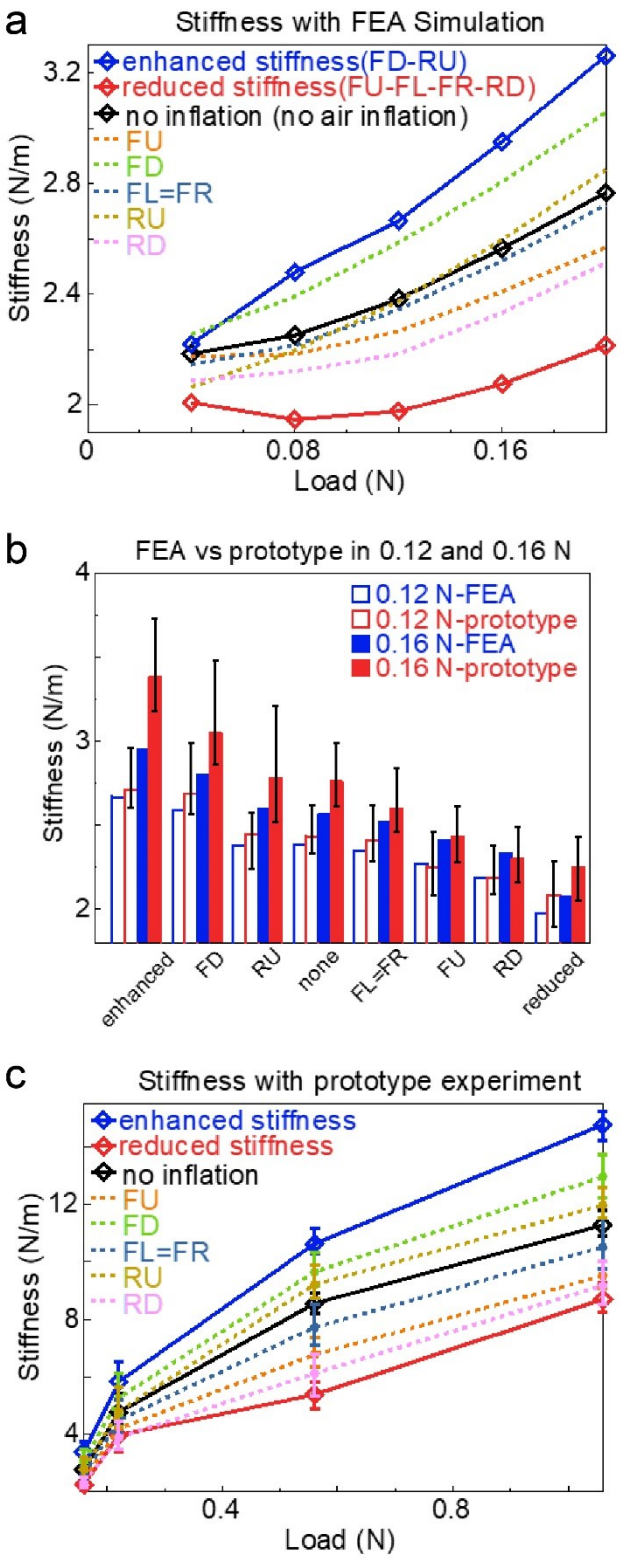

Figure 3.2 Stiffness Modulation Analysis (a) with FEA, (b) with FEA and Prototype Experiment, and (c) Under High Load with Prototype Experiment

To validate the outcomes of the FEA simulation, stiffness prototype experiments were conducted for the eight configurations. Under the 0.12 and 0.16 N load conditions, the order of stiffness intensity among eight configurations, as predicted by FEA simulations, aligned with stiffness prototype experiment results (Figure 3.2(b)). Although there was some variance in the exact stiffness values, the maximum deviation observed between the simulated and experimentally measured stiffness values for each configuration did not exceed 0.6 N/m. This measure indicates the upper limit of the difference and provides a clear gauge of the predictive capacity of the simulation model within its operational constraints. The distinction between low-load and high-load experimental conditions is due to the operational constraints of our FEA simulation model, which is calibrated for accurate performance up to a load of 0.2 N. Beyond this threshold, computational limitations arise, leading to potential inaccuracies.

Spearman correlation analysis further quantified the individual contributions of each chamber to overall deflection under loads ranging from 0 to 0.2 N, with detailed findings documented in Table 3.1. This analysis confirmed that the FD and RU chambers were negatively correlated with increased deflection, supporting the stiffness enhancements observed in Figure 3.2(a). Specifically, the FD chamber's correlation (-0.250) was significantly lower than the RU chamber's (-0.020), highlighting FD as a key contributor to stiffness improvement. Conversely, the RD chamber demonstrated the highest positive correlation (0.340) across all configurations, emphasizing its role in reducing stiffness.

Table 3.1 Spearman correlation of individual air chambers to soft actuator deflection

		Correlation	P-Value
	Load	0.860	0.000
Frontal Section	FU	0.220	0.000
	FD	-0.250	0.000
	FL	0.007	0.410
	FR	0.007	0.410
Rear Section	RU	-0.020	0.083
	RD	0.340	0.000

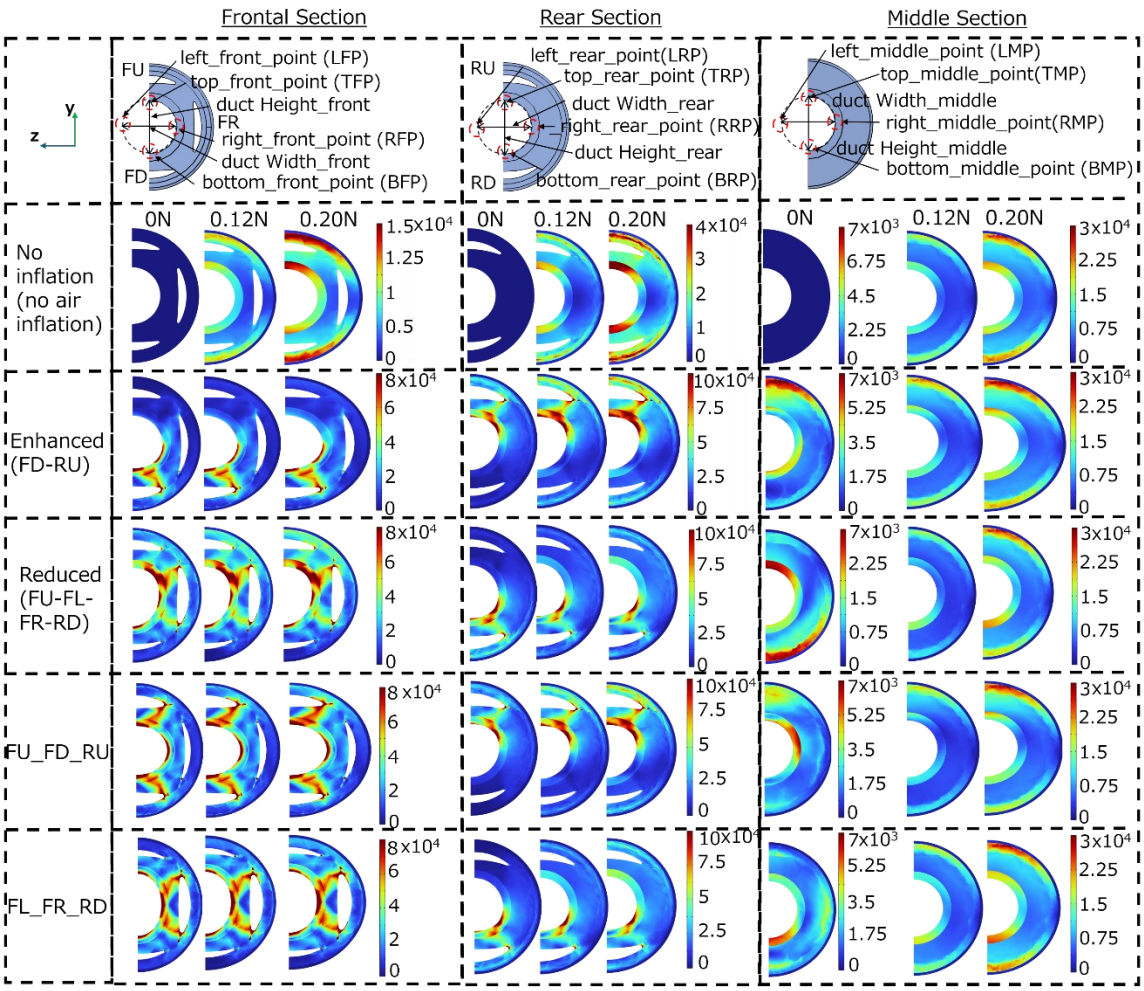

Figure 3.3 Comparative Stress Distribution Patterns Across Midsections of Frontal, Rear, Middle Sections for No Inflation, Enhanced Stiffness, Reduced Stiffness, FU-FD-RU, and FL-FR-RD Configurations.

Figure 3.3 presents the stress distribution in the cross sections of the actuator (frontal, rear, and middle sections) for the non-inflation, enhanced stiffness (FD-RU), reduced stiffness (FU-FL-FR-RD), FU-FD-RU, and FL-FR-RD configurations for direct comparisons. These examinations were carried out under three different applied loads: 0 N, 0.12 N, and 0.2 N. The stress responses of the actuator at four positions in each section were quantified (top, middle left, middle right, bottom) in Figures 3.4, and three-dimensional geometric changes of the hollow central duct in each section were investigated (width, height, and width-to-height aspect ratio) in Figures 3.5. This analysis aids in understanding the adaptation of the structural dimensions of the actuator to varying external loads, offering a detailed perspective on its mechanical adaptability and resilience.

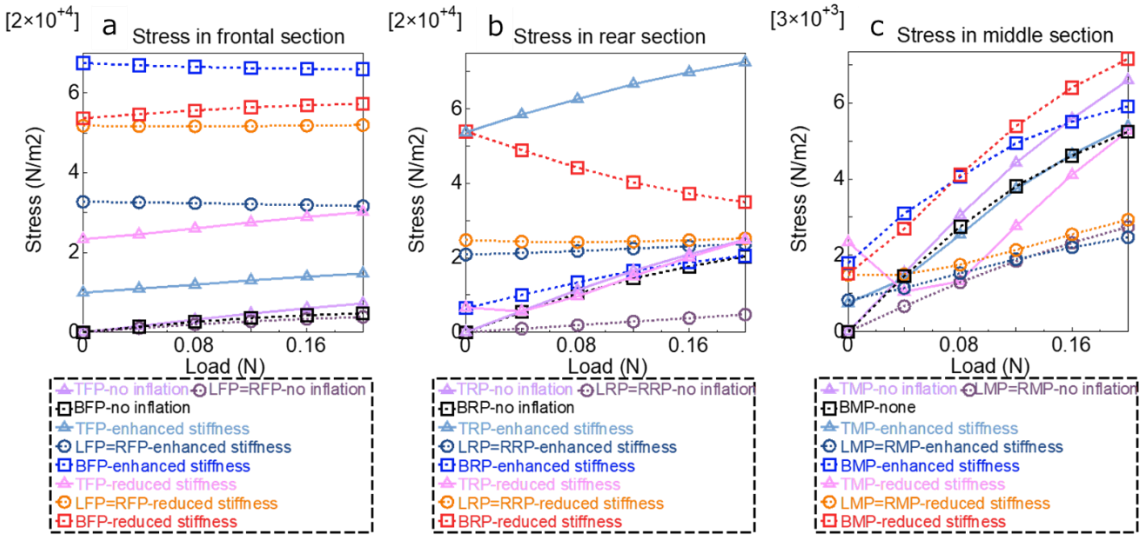

Figure 3.4 Stress in (b) Frontal Section, (c) Rear Section, (d) Middle Section

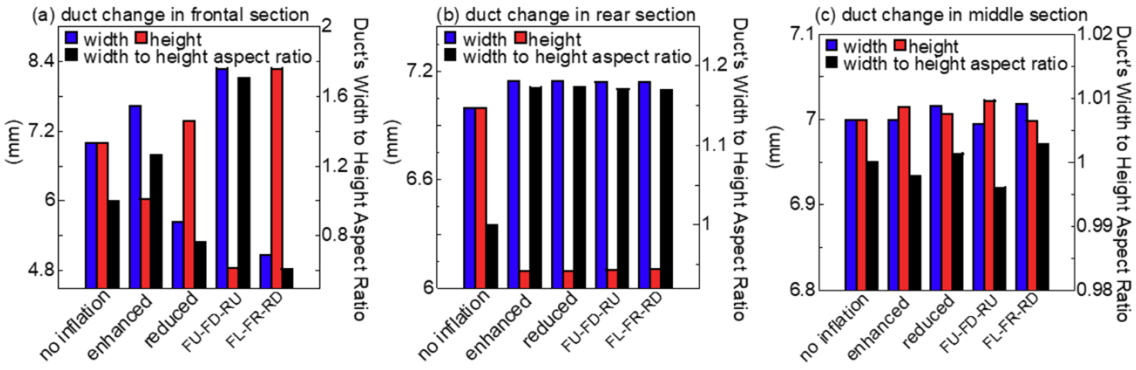

Figure 3.5 Dimensional Change Impacts: Hollow Central Duct Change in (e) Frontal Section, (f) Rear Section, and (g) Middle Section.

- Hollow Central Duct Stress Analysis

Our examination of the hollow central duct of the soft actuator under various configurations revealed distinct stress patterns across different load conditions, as shown in Figures 3.4.

Frontal Section: In the enhanced stiffness configuration, the stress at the bottom front point (BFP) position was consistently higher than those in other configurations across all load conditions. Conversely, in the reduced stiffness configuration, the top frontal point (TFP), left frontal point (LFP), and right frontal point (RFP) exhibited higher stress levels than the other configurations, regardless of the load condition. Although there was an increasing trend in stress with increasing load levels in the frontal section, this increase was not pronounced.

Furthermore, the FU-FD-RU configuration in the frontal section demonstrated increased stress at the TFP and BFP due to the inflation of the FU and FD chambers.

Additionally, the longitudinal compression of the hollow central duct contributed to the increased stress at the LFP and RFP. Finally, the FL-FR-RD configuration experienced elevated stress at the LFP and RFP following inflation of the FL and FR chambers. The lateral compression of the hollow central duct led to increased stress at the TFP and BFP.

Rear Section: Under the 0 N load condition (Figure 3.4(c)), the stress at the top read point (TRP) in the enhanced stiffness configuration and at the bottom rear point (BRP) in the reduced stiffness configuration was equivalent and highest. However, as the load increased, the stress at the TRP in the enhanced stiffness configuration increased significantly, far surpassing the stress at the BRP in the reduced stiffness configuration, which decreased with increasing load levels. Additionally, stress levels at the BRP in the enhanced stiffness configuration and at the TRP in the reduced stiffness configuration remained consistent and gradually increased with the load, but these values were substantially lower than those at the TRP in the enhanced stiffness configuration and at the BRP in the reduced stiffness configuration. Moreover, no significant differences were noted in the stress at the left rear point (LRP) and right rear point (RRP) between the enhanced and reduced stiffness configurations.

Furthermore, the FU-FD-RU configuration in the rear section demonstrated increased stress at the TRP due to the inflation of the RU chamber. Additionally, the FL-FR-RD configuration experienced elevated stress at the BRP following inflation of the RD chamber.

Middle Section: Under the 0 N load condition, the stress at the top middle point (TMP) in the reduced stiffness configuration was the highest among the configurations. The stress at the bottom middle point (BMP) in the enhanced stiffness configuration was high, second only to that at the TMP in the reduced stiffness configuration. The stress levels across all the configurations increased with increasing load levels. Furthermore, the order of stress differences at the TMP, left middle point (LMP), right middle point (RMP), and BMP among the different configurations, initially observed at the 0 N load condition, shifted dynamically as the load increased. This reveals a changing sequence in stress distribution across the configurations in response to increasing load levels.

Moreover, the FU-FD-RU configuration in the middle section reported higher stress levels at the TMP, LMP, and RMP than in the non-inflation and enhanced stiffness configurations. Additionally, the FL-FR-RD configuration exhibited greater stress at the BMP than the non-inflation and reduced stiffness configurations.

To further understand the relationship between actuator stiffness (K_d) and stress distribution resulting from inflation across 64 different conditions, we applied the Spearman correlation analysis for its effectiveness in nonlinear analysis. Detailed results are presented in Table 3.2. We measured the stress at a 0.12 N load condition across 12 specific points (termed Point Name_P) within the soft actuator. Consequently, for the Spearman correlation analysis, the independent variables were the internal stresses measured at these points under a 0.12 N load condition across the 64 different inflation configurations. The dependent variable was the actuator stiffness observed when subjected to a specific external load of 0.12 N.

This analysis indicates that BFP_P, TRP_P, and BMP_P are positively correlated with increased stiffness. Specifically, BFP_P showed a significantly higher correlation

(0.750) than TRP_P (0.450), emphasizing BFP's key role in enhancing stiffness. Conversely, BRP_P displayed the highest negative correlation (-0.410), highlighting its substantial impact on reducing stiffness. Moreover, stress in the middle section (TMP_P, LMP_P, RMP_P, and BMP_P) exhibited lower correlations and higher P-values than those in the frontal and rear sections, suggesting that stress at the frontal and rear sections has a more pronounced influence on stiffness than stress in the middle section.

Table 3.2 Spearman correlation of individual air chamber's air pressure to soft actuator deflection

		Correlation	P-Value
Frontal Section	TFP_P	-0.350	0.003
	LFP_P	-0.380	0.002
	RFP_P	-0.380	0.002
	BFP_P	0.750	0.000
Rear Section	TRP_P	0.450	0.000
	LRP_P	-0.389	0.001
	RRP_P	-0.389	0.001
	BRP_P	-0.410	0.002
Middle Section	TMP_P	-0.386	0.001
	LMP_P	-0.140	0.270
	RMP_P	-0.140	0.270
	BMP_P	0.140	0.260

- Dimensional Change Impacts

Our observations revealed distinct dimensional changes in the hollow central duct under a 0 N load, as depicted in Figures 3.5. Across all configurations, dimensional changes in the hollow central duct did not exhibit significant variations with increasing load within the 0.2 N range, as confirmed in Supplementary Information, Figures 3.6. These figures show that the dimensional differences among configurations remain consistent under load conditions up to 0.2 N. Therefore, we selected the 0.12 N condition as a representative baseline for our analysis, providing a clear understanding of how different configurations affect the hollow central duct's dimensions without the complicating factor of load-induced deformation.

Frontal Section: The enhanced stiffness configuration displayed the widest width and largest width-to-height aspect ratio compared to both the non-inflation and reduced stiffness configurations. Notably, the FU-FD-RD configuration surpassed all other configurations (63 configurations) in terms of width and width-to-height aspect ratio. Conversely, the reduced stiffness configuration had the tallest height and smallest width-

to-height aspect ratio compared to the non-inflation and enhanced stiffness configurations. The FL-FR-RD configuration exhibited the highest height and smallest width-to-height aspect ratio among all configurations.

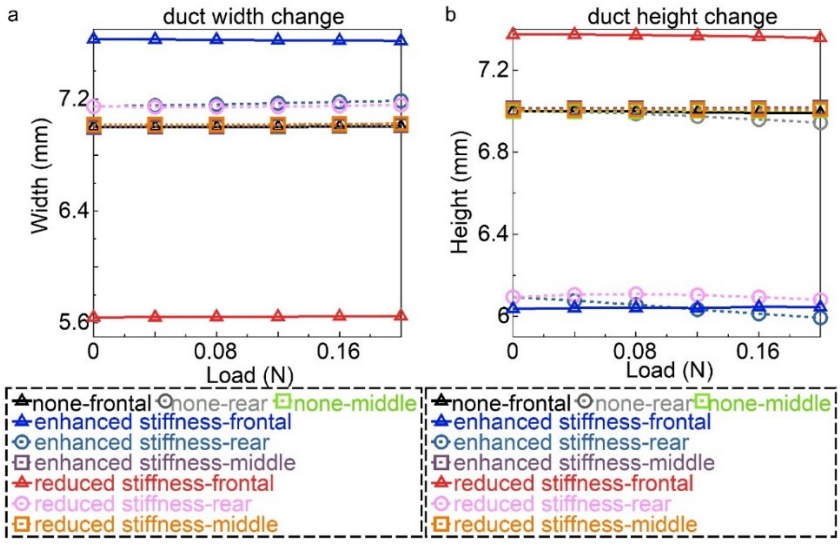

Figure 3.6 Dimensional Change Across Different Loads: (a) Duct Width Change and (b) Duct Height Change

Rear Section: Configurations such as enhanced stiffness, reduced stiffness, FU-FD-RU, and FL-FR-RD showed both greater width and a larger width-to-height aspect ratio than the no-inflation configuration. Similarly, the heights in these configurations were smaller than those in the no-inflation configuration.

Middle Section: The enhanced stiffness configuration exhibited the highest height and smallest width-to-height aspect ratio compared to the non-inflation and reduced stiffness configurations. The FU-FD-RD configuration showed the highest height and smallest width-to-height aspect ratio among all configurations. In contrast, the reduced stiffness configuration displayed the widest width and largest width-to-height aspect ratio compared to the non-inflation and enhanced stiffness configurations. The FL-FR-RD configuration had the widest width and largest width-to-height aspect ratio among all configurations. However, the differences in width, height, and width-to-height aspect ratio among the different configurations in the middle section were significantly smaller than those observed in the frontal and rear sections.

3.4.2 Results of Tip-Bending Angle, Time Response, and Tip Force in Soft Actuators

- Tip-Bending Angle

In Figures 3.7(a), (c), and (e), the x-axis represents air pressure variations in the FD chamber (frontal section). Similarly, Figures 3.7(b), (d), and (f) detail the rear section, with the x-axis emphasizing air pressure changes in the RD chamber.

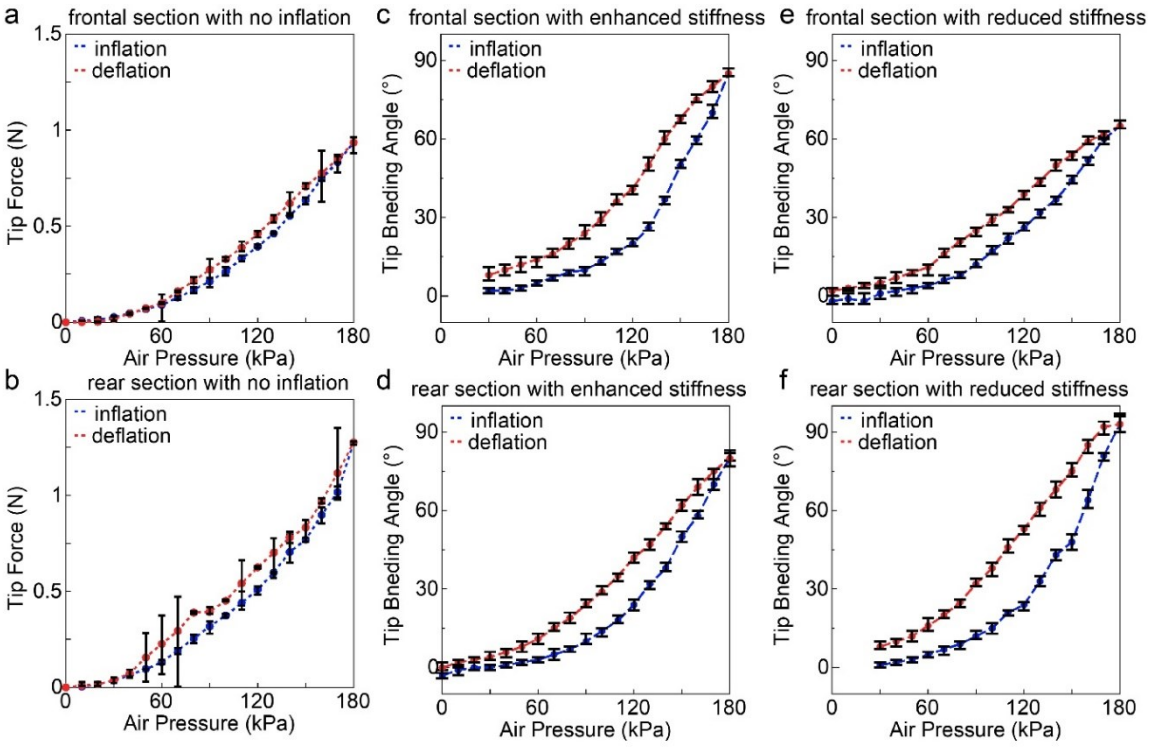

Figure 3.7 Bending Property: (a) Frontal Section and (b) Rear Section with No Inflation, (c) Frontal Section and (d) Rear Section with Enhanced Stiffness, (e) Frontal Section and (f) Rear Section with Reduced Stiffness

For the no-inflation configuration (Figures 3.7(a) and 4(b)), both the frontal and rear sections displayed maximum tip-bending angles exceeding 90°, with exact measurements being 91° and 94°, respectively. A significant pneumatic hysteresis in the soft actuator was evident when comparing the angles during inflation and deflation. At identical air pressure levels, this hysteresis resulted in angle differences surpassing 30°.

Under the enhanced stiffness configuration (Figures 3.7(c) and 3.4(d)), the frontal section's maximum tip-bending angle decreased slightly to 85° compared to the no-inflation configuration. Though there was a marginal improvement in pneumatic hysteresis, it remained relatively subtle. However, the rear section exhibited a notable decrease in its maximum tip-bending angle, reaching 80°. There was also a marked reduction in pneumatic hysteresis, with the angle differences between inflation and deflation at identical pressures being only 14°.

Regarding the reduced stiffness configuration (Figures 3.7(e) and 4(f)), the frontal section's maximum tip-bending angle significantly declined to 65° compared to the non-inflation state. The pneumatic hysteresis also improved, with angle differences of only 13° at consistent pressures. However, the rear section under this setup did not display any considerable shifts in the maximum tip-bending angle or pneumatic hysteresis.

- Time Response

Figures 3.8(a)–(c) present the real-time tip-bending angle of the soft actuator across three configurations (no-inflation, enhanced stiffness, and reduced stiffness) at a frequency of 0.5 Hz. Figures 3.8(d)–(f) show the maximum tip-bending angles and corresponding rising times across frequencies from 0.1 to 0.5 Hz. Under static conditions at a maximum air pressure of 180 kPa, the soft actuator is expected to achieve a tip-bending angle of 90°, termed the "desired angle." Rising time is characterized by the time taken for the angle to shift from 9° (10% of the desired angle) to 81° (90% of the desired angle).

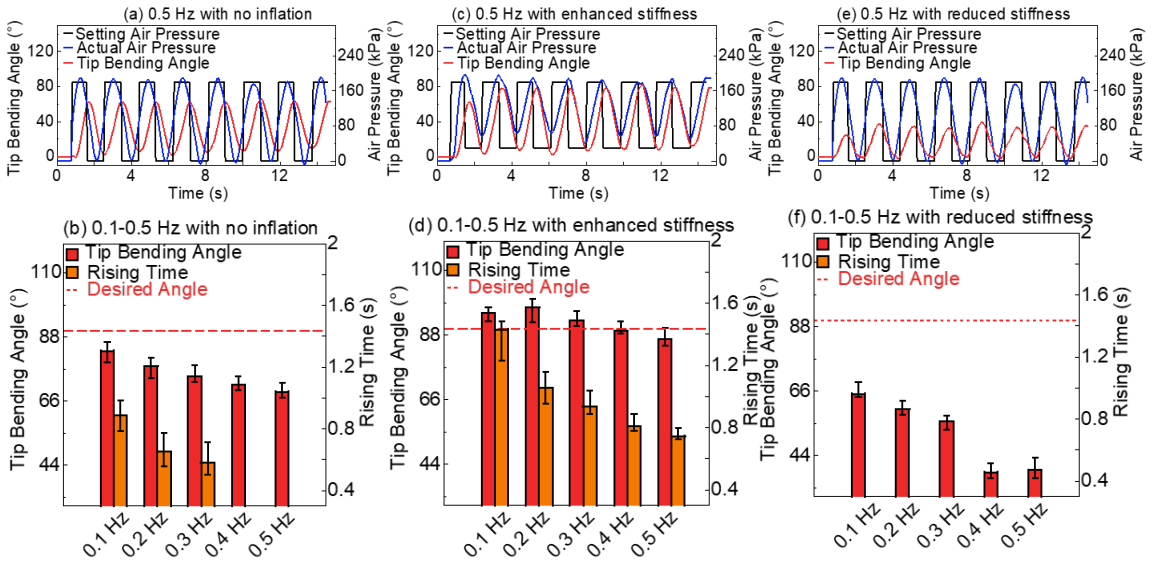

Figure 3.8 Response Property: (a) 0.5 Hz and (b) 0.1–0.5 Hz with No Inflation, (c) 0.5 Hz and (d) 0.1–0.5 Hz with Enhanced Stiffness, (e) 0.5 Hz and (f) 0.1–0.5 Hz with Reduced Stiffness

In the no-inflation configuration, the soft actuator failed to reach the desired 90° angle under air pressure frequency variations from 0.1 to 0.5 Hz, as indicated in Figures 3.8(a) and (b). Specifically, at 0.1 Hz, the angle peaked at 85°. At 0.5 Hz, the tip-bending angle exhibited a phase lag exceeding 0.5 s compared to the actual air pressure, as depicted in Figures 3.5(a).

In the enhanced stiffness configuration, the actuator consistently reached the 90° mark at frequencies from 0.1 to 0.4 Hz. At 0.5 Hz, the actuator achieved an angle of 85°, as shown in Figures 3.8(c) and (d). As the frequency increased, the rising time decreased correspondingly. Although a phase lag persisted at 0.5 Hz, as observed in Figure 3.8(c), it was reduced, registering a time difference of less than 0.3 s between the peaks of the tip-bending angle and the actual air pressure.

For the reduced stiffness configuration, the actuator consistently underperformed and did not reach the 90° target across frequencies from 0.1 to 0.5 Hz. At 0.1 Hz, the maximum angle reached was 65°. However, at 0.5 Hz, as illustrated in Figure 3.8(e), the phase lag between the tip-bending angle and actual air pressure was notably smaller, with a discrepancy of approximately 0.15 s.

- Tip force

Figure 3.9 shows the tip force evaluation for the no-inflation, enhanced stiffness, and reduced stiffness conditions. In the no-inflation configuration, the soft actuator exhibited a notable tip force in both the frontal and rear sections. The frontal section reached a maximum tip force of 0.93 N, while the rear section achieved 1.28 N, as depicted in Figures 3.7(a) and (b). A significant observation is the hysteresis with air pressure, with a disparity of over 0.13 N in tip force identified when comparing the inflation and deflation processes at consistent air pressures.

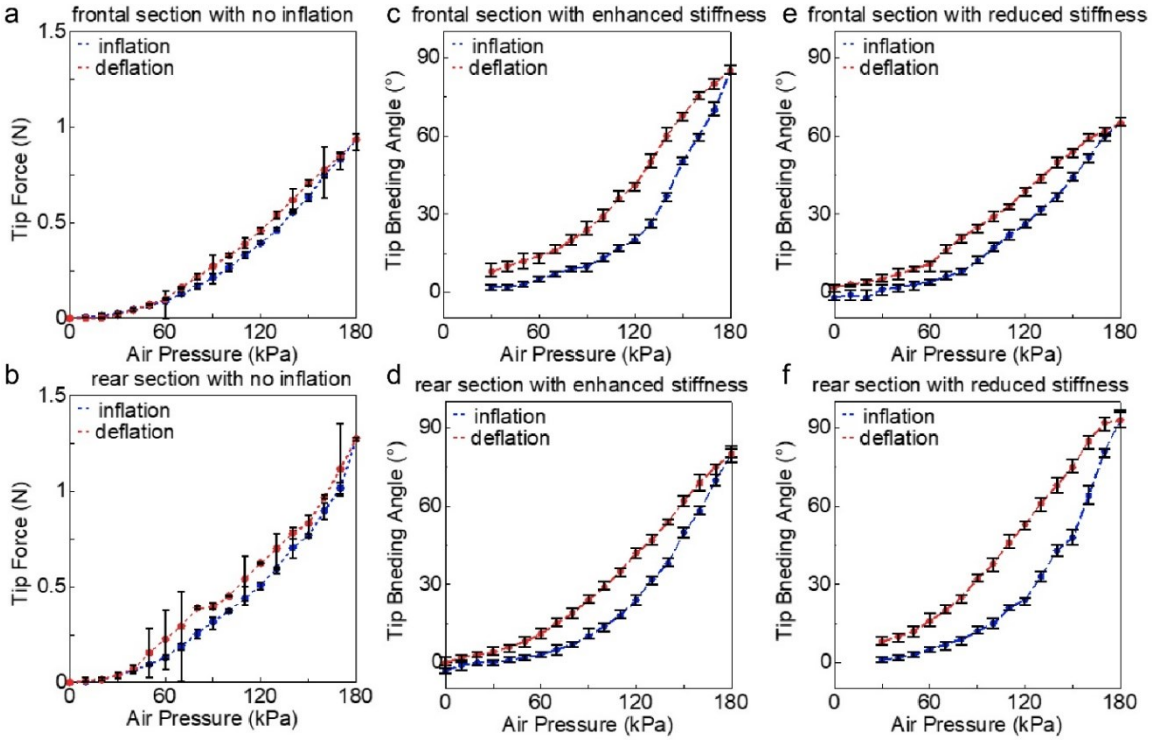

Figure 3.9 Tip Force: (a) Frontal Section and (b) Rear Section with No Inflation, (c) Frontal Section and (d) Rear Section with Enhanced Stiffness, (e) Frontal Section and (f) Rear Section with Reduced Stiffness

Under the enhanced stiffness configuration, the frontal section saw a marginal decrease in its maximum tip force to 0.86 N relative to the no-inflation configuration. The observed hysteresis was slightly improved but not significantly different from that of the non-inflated configuration. Conversely, the rear section recorded a more pronounced reduction in its maximum tip force to 1.02 N. Notably, the hysteresis displayed a marked improvement, with a maximum disparity of 0.09 N between inflation and deflation tip forces at identical air pressures.

In the reduced stiffness configuration, the maximum tip force of the frontal section significantly decreased to 0.6 N. This configuration showed a pronounced improvement in hysteresis relative to the no-inflation setup, with a mere 0.03 N difference between the

inflation and deflation tip forces at consistent air pressures. Meanwhile, the rear section maintained stability, with its maximum tip force and hysteresis closely mirroring those of the no-inflation configuration.

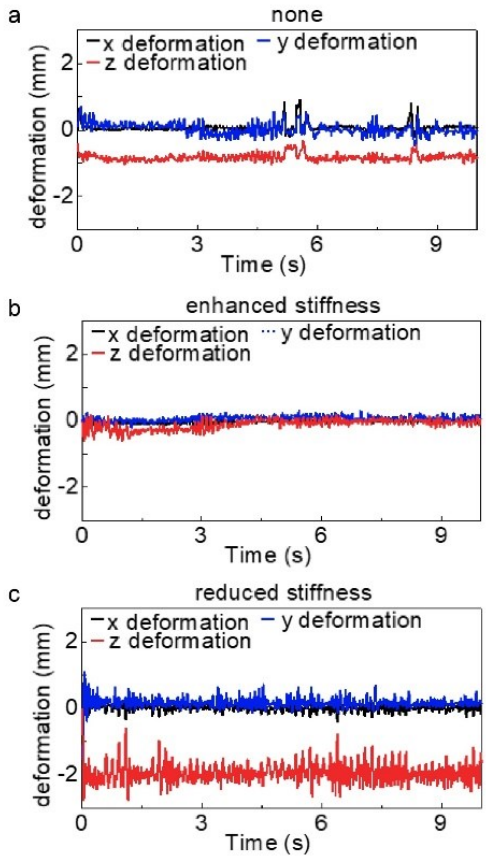

Figure 3.10 Deformation Response Under Noise with (a) No Inflation, (b) Enhanced Stiffness, and (c) Reduced Stiffness

3.4.3 Results of Perturbation-Resisting Experiment in Bladder–Prostate Model

In the prototype experiment using a bladder–prostate model to assess the impact of effective stiffness configurations on single-port transvesical prostatectomy, deformation responses in the x-, y-, and z-directions were meticulously recorded and are presented in Figures 3.10(a), (b), and (c). The introduction of perturbation from the hair dryer significantly amplified z-direction deformation across all configurations and induced erratic movement in the x- and y-directions. Specifically, the enhanced stiffness configuration exhibited the least deformation in the z-direction, measuring less than 0.6 mm (mean: 0.10 mm, standard deviation: 0.15 mm). The no-inflation configuration showed slightly greater deformation, close to 1 mm (mean: 0.82 mm, standard deviation: 0.117 mm), while the reduced stiffness configuration experienced the most significant deformation, nearing 2 mm (mean: 1.93 mm, standard deviation: 0.33 mm). In terms of x- and y-directional movements, the reduced stiffness configuration exhibited the most

pronounced fluctuations, with amplitude variations exceeding 1 mm. This was followed by the no-inflation configuration, while the enhanced stiffness configuration displayed the least amount of oscillation.

Endoscopic and external monitoring camera observations demonstrated that the enhanced stiffness configuration significantly outperformed the others in terms of visual field stability. The reduced and no-inflation configurations experienced more pronounced and frequent tremors.

3.5. Discussion

In this study, we constructed an FEA simulation model for a soft actuator with a complex structure to clarify the mechanism of stiffness modulation in multiple antagonistic chambers. We focused on the internal stress distribution and hollow central duct structure resulting from the inflation of multiple antagonistic chambers and their impact on stiffness modulation.

- FEA Simulation Model

The observed consistency in stiffness trends across all configurations in our FEA simulations and prototype experiments highlights the effectiveness of the FEA model for studying stiffness modulation within soft actuators equipped with multiple antagonistic chambers (Figure 3.2). Designed for enhanced maneuverability and control, the crescent-shaped flat thin chambers of our actuator present substantial computational challenge, notably in terms of mesh generation and predicting the material response under applied loads. Consequently, our FEA model was tuned for simulations with a certain accuracy up to a load of 0.2 N. Predicting the nonlinear behavior of hyperelastic materials and complex geometries becomes challenging, limiting the broader application of the model. The extension of the prototype experiments to higher loads (0.22 N, 0.56 N, and 1.06 N) was not aimed at direct model validation but rather at confirming that the stiffness modulation trends observed at lower loads persisted under these increased conditions.

Discrepancies observed in stiffness measurements under the same load conditions (0.12 and 0.16 N), not exceeding a difference of 0.6 N/m, indicate variance between FEA simulations and experimental outcomes (refer to Figure 3.2(b)). This variance stems from different load application methods; simulations apply loads uniformly across surface contacts, while prototype experiments use line contacts with weights. Despite these differences limiting direct numerical comparisons, the consistency in stiffness trends between the simulations and experiments affirms the robustness and reliability of the simulation model within its operational parameters.

- Stiffness Analysis of Evaluation

The simulation results support our hypothesis that internal stress distribution and hollow central duct structure, influenced by chamber inflation, are critical for stiffness modulation. Our findings confirm that specific chamber inflation effectively alters the internal stress distribution of the actuator. In each section of the soft actuator, the stiffness evaluation experiment was conceptualized as a beam-bending scenario (Figures 3.11(a-f)). Previous

research [54] has established that the bending moment and geometrical moment of inertia of a beam directly influence its slope, as calculated using Equation (3.3).

$$\theta = \frac{1}{EI}\int M\,dx \tag{3.3}$$

Here, θ: slope, M: bending moment, E: Young's modulus, I: geometrical moment of inertia, and dx: infinitesimal length of the beam along the x-axis (neutral axis)—all shown in Figure 3.12(a).

Previous research [54] also established that both Young's modulus (E) and the geometrical moment of inertia (I) significantly influence the flexural stiffness (K) of a beam, as outlined by Equation (3.4). Equation (3.3) can express E and I in terms of the integral of bending moment over a length ($\int M\,dx$) and slope (θ), subsequently incorporating these into Equation (3.4).

$$K = EI = \frac{\int M\,dx}{\theta} \tag{3.4}$$

When evaluating the flexural stiffness (K_{cs}) of soft actuators under various inflation configurations at different sections, Equation (3.5) is used, where "c" denotes different configurations, including enhanced stiffness (e) and reduced stiffness (r), and "s" signifies sections of the soft actuator, including frontal (f), rear (r), and middle (m) sections. "M_L" represents the bending moment induced by external loads (L), "θ_{cs}" the slope under L for different configurations, "I_{cs}" the geometrical moment of inertia for different configurations, and "M_{cs}" the bending moment exerted on the soft actuator due to external load (L) for different inflation configurations. Depending on the specific inflation configuration, M_{cs} may be larger or smaller than M_L, indicating a variable influence of inflation on the resistance of the actuator to bending moments.

$$K_{cs} = \frac{\int M_L\,dx}{\theta_{cs}} = \frac{\int M_L\,dx}{\frac{1}{EI_{cs}}\int M_{cs}\,dx} \tag{3.5}$$

For soft actuators in a non-inflated configuration, stiffness (K_L) is calculated using Equation (3.6), where "I_L" represents the geometrical moment of inertia in a non-inflated configuration. The stiffnesses of the different configurations relative to the non-inflated configuration ($\frac{K_{cs}}{K_L}$) were evaluated using Equation (3.7). A higher value of $\frac{K_{cs}}{K_L}$ indicates higher stiffness for that configuration. It can be observed from Equation (7) that $\frac{K_{cs}}{K_L}$ is primarily influenced by the ratios of $\frac{I_{cs}}{I_L}$ and the values of M_{cs}; higher $\frac{I_{cs}}{I_L}$ and lower M_{cs} indicate higher stiffness.

$$K_L = \frac{\int M_L\, dx}{\theta_L} = \frac{\int M_L\, dx}{\frac{1}{EI_L}\int M_L\, dx} \tag{3.6}$$

$$\frac{K_{cs}}{K_L} = \frac{\frac{\int M_L\, dx}{\frac{1}{EI_{cs}}\int M_{cs}\, dx}}{\frac{\int M_L\, dx}{\frac{1}{EI_L}\int M_L\, dx}} = \frac{I_{cs}}{I_L}\frac{\int M_L\, dx}{\int M_{cs}\, dx} \tag{3.7}$$

The ratios of $\frac{I_{cs}}{I_L}$, $\frac{M_{cs}}{M_L}$, and values of M_{cs} for various configurations are summarized in Table 3.3.

Table 3.3 Summary of Bending Moment and Geometrical Moment of Inertia on Each Section (see Supplementary Information for details of calculation)

		$\frac{I_{cs}}{I_L}$	$\frac{M_{cs}}{M_L}$
Frontal	Enhanced	$\frac{I_{ef}}{I_L} = 1.05$	$\frac{M_{ef}}{M_L} = \frac{M_L - M_{qf}}{M_L} = \frac{1.37 \times 10^{-4}}{2.9 \times 10^{-4}} = 0.47$
	Reduced	$\frac{I_{rf}}{I_L} = 0.79$	$\frac{M_{rf}}{M_L} = \frac{M_L + M_{qf}}{M_L} = \frac{4.50 \times 10^{-4}}{2.9 \times 10^{-4}} = 1.55$
Rear	Enhanced	$\frac{I_{er}}{I_L} = 1.01$	$\frac{M_{er}}{M_L} = \frac{M_L + M_{qr}}{M_L} = \frac{3.07 \times 10^{-4}}{2.9 \times 10^{-4}} = 1.05$
	Reduced	$\frac{I_{er}}{I_L} = 1.01$	$\frac{M_{rr}}{M_L} = \frac{M_L - M_{qr}}{M_L} = \frac{2.77 \times 10^{-4}}{2.9 \times 10^{-4}} = 0.96$

Middle	Enhanced	$\frac{I_{em}}{I_L} = 1.00$	$\frac{M_{em}}{M_L} = \frac{M_L - M_{qm}}{M_L} = \frac{2.89 \times 10^{-4}}{2.9 \times 10^{-4}}$
	Reduced	$\frac{I_{rm}}{I_L} = 1.00$	$\frac{M_{rm}}{M_L} = \frac{M_L + M_{qm}}{M_L} = \frac{2.91 \times 10^{-4}}{2.9 \times 10^{-4}} = 1.01$

Detailed information on all the bending moments, geometrical moments of inertia, and additional relevant parameters, including their comprehensive calculations, can be found in below.

- Frontal Section

Chamber inflation significantly alters the geometry of the hollow central duct in the frontal section. In the enhanced stiffness configuration, inflating the FD chamber modifies the cross-sectional shape of the duct, increasing its width and decreasing its height, resulting in an ellipse with its major axis parallel to the neutral axis. This transformation leads to a greater geometrical moment of inertia (I_{ef} is calculated using Equation (3.8), enhancing stiffness as $\frac{I_{ef}}{I_L}$ (I_L is calculated using Equation (3.9) exceeds one. Additionally, this inflation induces a counteractive bending moment ($-M_{qf}$) against the bending moment induced by external loads (M_L is calculated using Equation (3.10), effectively reducing the total bending moment (M_{ef} is calculated using Equation (3.11) compared to other configurations. Spearman's correlation analysis confirmed this observation, showing a positive correlation between FD chamber inflation, stress at the BFP, and stiffness. Conversely, the reduced stiffness configuration involves inflating the FU, FL, and FR chambers, which decreases the width and increases the height of the cross-section of the hollow central duct. This adjustment forms an ellipse with its major axis perpendicular to the neutral axis, resulting in a lower geometrical moment of inertia (I_{rf} is calculated using Equation (3.12). This change suggests a reduction in stiffness as $\frac{I_{rf}}{I_L}$ falls below one. Furthermore, the combined inflation of the FU, FL, and FR chambers introduces a bending moment (M_{qf}) that favors downward bending and deformation, resulting in a higher bending moment (M_{rf} is calculated using Equation (3.13) compared to other configurations. The impact of this scenario on stiffness was confirmed by Spearman's correlation analysis, which revealed a negative correlation between the inflation of the FU, FL, and FR chambers, stress at TFP, and stiffness (see Tables 3.2 and 3.3).

$$I_{ef} = \frac{\pi}{4}(a_{eo}^3 b_{eo} - a_{ei}^3 b_{ei}) = 3.24 \times 10^{-9}\ [m^4]$$

a_{eo}: 0.0083 [m], b_{eo}: 0.0075 [m],

a_{ei}: 0.0038 [m], b_{ei}: 0.0030 [m];

(3.8)

$$I_L = I_{em} = I_{rm} = \frac{\pi}{64} \times (d_o^4 - d_i^4) = 3.09 \times 10^{-9}\ [m^4]$$

d_o: 0.0160[m], d_i: 0.0070 [m];

(3.9)

$$M_L = L \times l_1 \left(l_2 + l_3 + l_4 + l_5 + \frac{l_1}{2} \right) = 2.9 \times 10^{-4}\ [Nm]$$

L: 0.2 [N], l_1: 0.01 [m], l_2: 0.05 [m], l_3: 0.06 [m], l_4: 0.06 [m], l_5: 0.02 [m];

(3.10)

$$M_{ef} = M_L - M_{qf} = L \times l_1 \left(l_2 + l_3 + l_4 + l_5 + \frac{l_1}{2} \right) - q_f \cdot l_2 \left(l_3 + l_4 + l_5 + \frac{l_2}{2} \right) = 1.37 \times 10^{-4}\ [Nm]$$

q_f: 0.0027 [N], l_1: 0.01 [m], l_2: 0.049 [m], l_3: 0.06 [m], l_4: 0.06 [m], l_5: 0.02 [m];

(3.11)

$$I_{rf} = \frac{\pi}{4}(a_{ro} b_{ro}^3 - a_{ri} b_{ri}^3) = 2.44 \times 10^{-9}\ [m^4]$$

$a_{ro} = e_{rf}$: 0.0082 [m], b_{ro}: 0.0073 [m],

a_{ri}: 0.0037 [m], b_{ri}: 0.0028 [m];

(3.12)

$$M_{rf} = M_L + M_{qf} = L \times l_1 \left(l_2 + l_3 + l_4 + l_5 + \frac{l_1}{2} \right) + q_f \cdot l_2 \left(l_3 + l_4 + l_5 + \frac{l_2}{2} \right) = 4.50 \times 10^{-4}\ [Nm]$$

q_f: 0.027 [N], l_1: 0.01 [m], l_2: 0.052 [m], l_3: 0.06 [m], l_4: 0.06 [m], l_5: 0.02 [m];

(3.13)

The selection of L at 0.2 N represents the maximum load applied in simulations to effectively compare differences across configurations. The values of q_f,q_r, and q_m were derived from the forces generated at the corresponding positions when the chambers were inflated to 30 kPa, as measured by our FEA simulation model.

All the relevant parameters were selected from the results of the FEA simulation model when the chambers were inflated to 30 kPa.

- Rear Section

In the rear section, inflating the RU chamber for the enhanced stiffness configuration produced a higher bending moment (M_{er}) is calculated using Equation (3.14), promoting downward bending and deformation, which suggests reduced stiffness. M_{qf} significantly exceeded M_{qr}, indicating that the bending moments have a less pronounced effect on

deformation in the rear section compared to the front section. In contrast, for the reduced stiffness configuration, inflating the RD chamber resulted in a lower bending moment (M_{rr}) is calculated using Equation (3.15), indicating enhanced stiffness. These findings seem to contradict the results of the Spearman's correlation analysis. Additionally, inflating the RU chamber in the enhanced stiffness setup altered the geometry of the hollow central duct by flattening the upper part, increasing its width, and reducing its height, transforming its cross-section from circular to triangular with the base above the neutral axis, as shown in Figure 3.11 right. Similarly, inflating the RD chamber in the reduced stiffness configuration modified the lower part of the duct, creating a base-below-the-neutral-axis triangular cross-section, as depicted in Figure 3.11(d) right. Despite the geometric similarities of the hollow central ducts in both configurations, with the neutral axis bisecting their centroids, the different base positions yielded identical geometrical moments of inertia ($I_{er} = I_{rr}$). The complex cross sections in the rear of the enhanced- and reduced stiffness configurations were complex. Consequently, I_{er} ($= I_{rr}$) was calculated using CAD software (Autodesk Inventor Professional 2024, USA) as detailed in Equation (3.16).

$$M_{er} = M_L + M_{qr} = L \times l_1 \left(l_2 + l_3 + l_4 + l_5 + \frac{l_1}{2}\right) + q_r \cdot l_4 \left(l_5 + \frac{l_4}{2}\right) = 3.07 \times 10^{-4}\ [Nm]$$

L: 0.2 [N], q_r: 0.0027 [N], l_1: 0.01 [m], l_2: 0.05 [m], l_3: 0.064 [m], l_4: 0.06 [m], l_5: 0.02 [m];

(3.14)

$$M_{rr} = M_L - M_{qr} = L \times l_1 \left(l_2 + l_3 + l_4 + l_5 + \frac{l_1}{2}\right) - q_r \cdot l_4 \left(l_5 + \frac{l_4}{2}\right) = 2.77 \times 10^{-4}\ [Nm]$$

L: 0.2 [N], q_r: 0.0027 [N], l_1: 0.01 [m], l_2: 0.05 [m], l_3: 0.058 [m], l_4: 0.06 [m], l_5: 0.02 [m];

(3.15)

$$I_{er} = I_{rr} = 3.15 \times 10^{-9}\ [m^4]$$

(3.16)

All the relevant parameters were selected from the FEA simulation model results when the chambers were inflated to 30 kPa.

- Middle section

The middle section, acting as an adjacent non-inflated area, predominantly experiences stress variations due to inflations in both the frontal and rear sections. In the enhanced stiffness configuration, notable stress changes at the BMP position resulted from inflating the FD chamber, which produced a bending moment (M_{em} is calculated using Equation (3.17) lower than the base moment (M_L), thereby thus enhancing stiffness. Spearman's correlation analysis supported this finding, showing a positive correlation between the stress at the BMP and reduced stiffness. Conversely, the reduced stiffness configuration caused primary stress changes at the TMP due to inflating the FU, FL, and FR chambers. This action produced a bending moment (M_{rm} is calculated using Equation (3.18) higher

than M_L, promoting bending and deformation, and thus reducing stiffness, as indicated by a negative correlation between stress at TMP and stiffness in the Spearman analysis.

$$M_{em} = M_L - M_{qm} = L \times l_1 \left(l_2 + l_3 + l_4 + l_5 + \frac{l_1}{2} \right) - q_m \cdot l_3 \left(l_4 + l_5 + \frac{l_3}{2} \right) = 2.89 \times 10^{-4}\ [Nm]$$

L: 0.2 [N], q_m: 0.0009 [N], l_1: 0.01 [m], l_2: 0.05 [m], l_3: 0.06 [m], l_4: 0.06 [m], l_5: 0.02 [m];

(3.17)

$$M_{rm} = M_L + M_{qm} = L \times l_1 \left(l_2 + l_3 + l_4 + l_5 + \frac{l_1}{2} \right) + q_m \cdot l_3 \left(l_4 + l_5 + \frac{l_3}{2} \right) = 2.91 \times 10^{-4}\ [Nm]$$

L: 0.2 [N], q_m: 0.0012 [N], l_1: 0.01 [m], l_2: 0.05 [m], l_3: 0.06 [m], l_4: 0.06 [m], l_5: 0.02 [m];

(3.18)

All the relevant parameters were selected from the FEA simulation model results when the chambers were inflated to 30 kPa.

In the following discussion, we explore how the internal stress distribution and state of the hollow central duct, influenced by the inflation of various chambers, affect the stiffness modulation across the frontal, rear, and middle sections of the soft actuator.

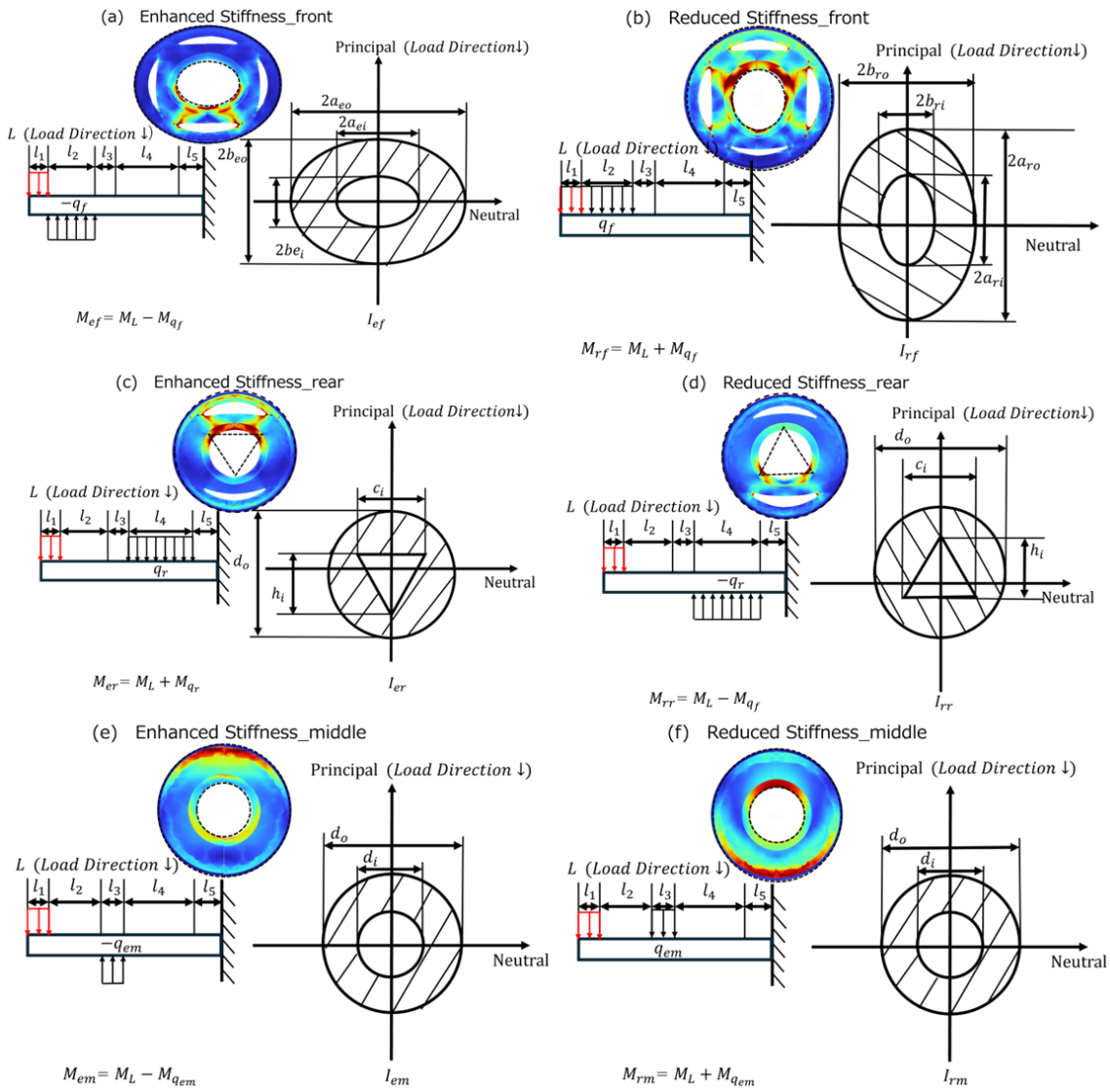

Figure 3.11 Analysis of Bending Moment and Geometrical Moment of Inertia with (a) Enhanced Stiffness Front, (b) Reduced Stiffness Front, (c) Enhanced Stiffness Rear, (d) Reduced stiffness Rear, (e) Enhanced Stiffness Middle, (f) Reduced Stiffness Middle,

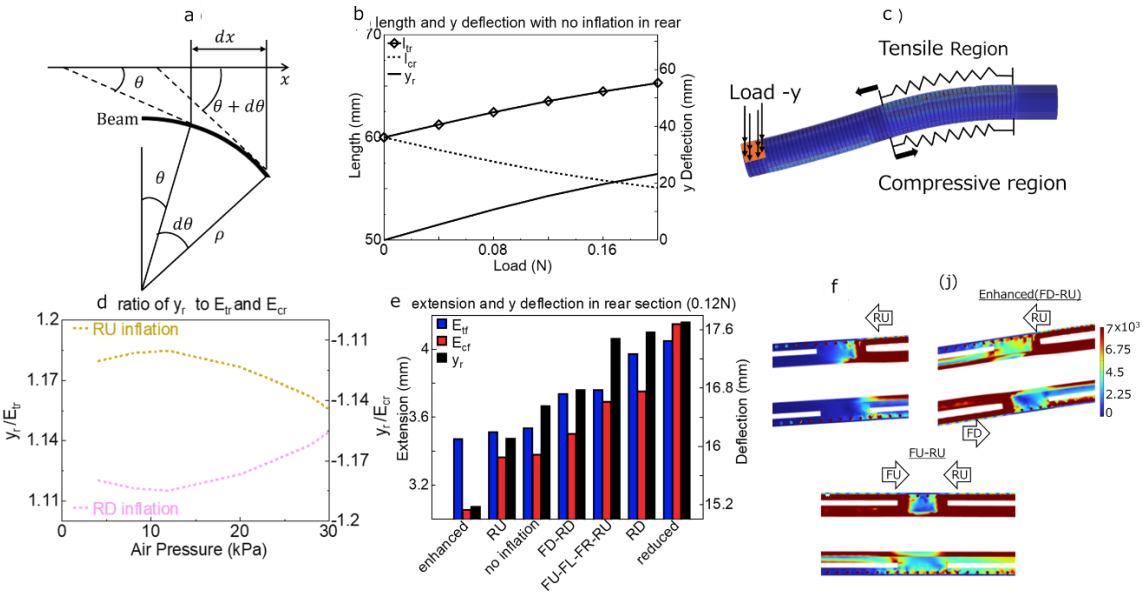

Figure 3.12 Impact of Chamber Inflation on Rear Section Extension and Stiffness: (a) Parameters on Beam Bending (b) Changes in Length for Tensile and Compressive Regions Under Load, (c) Spring Model in Rear Section, (d) Ratio of y deflection to Extension in Tensile and Compressive Region, (e) Comparison of y deflection with Extension on Tensile and Compressive Region (0.12 N), and (f) Comparative Analysis of Inflation Impact on Rear Section Geometry

- Front Section

In the frontal section, actively inflating specific chambers to alter the stress distribution and geometry of the hollow central duct, thereby generating bending moments either opposing or aligning with the external load and achieving higher or lower geometrical moments of inertia, is crucial for enhancing or reducing stiffness. These factors have a synergistic effect on stiffness modulation. Spearman correlation analysis revealed that stress at the BFT (associated with opposing bending moments to the external load and increased geometrical moments of inertia) was positively correlated with stiffness. Conversely, stress at the TFP (linked to bending moments aligned with the external load and reduced geometrical moments of inertia) was negatively correlated with stiffness.

Despite the FU-FD-RU configuration having the widest duct cross-section, indicating the highest geometrical moment of inertia (as illustrated in Figure 3.5(a)), its stiffness was less than that of the enhanced configuration due to the absence of a bending moment that opposes the external load.

In contrast, the FL-FR-RD configuration exhibited a higher stiffness than the reduced stiffness configuration, despite its lower geometrical moment of inertia. This enhanced stiffness arises from the lack of bending moments in alignment with the external loads, thereby increasing resistance to deformation.

- Rear Section

In the rear section, when comparing the bending moments of configurations with enhanced stiffness ($M_{er} = 3.07 \times 10^{-4}$ $[Nm]$) and reduced stiffness ($M_{er} = 2.77 \times 10^{-4}$ $[Nm]$)to the bending moment induced by external loads ($M_L = 2.9 \times 10^{-4}$ $[Nm]$ in Table 3.3, the minimal variance in bending moments between different configurations in the rear section is primarily due to the positioning of the inflation chambers near the fixed end. The proximity of these chambers to the fixed end limits their mechanical leverage, as a shorter distance from the pivot point reduces their capacity to generate significant bending moments compared to inflation chambers in the frontal section. This minimal variance in bending moments between the configurations is quantified by the ratios $\frac{M_{er}}{M_L}$ and $\frac{M_{rr}}{M_L}$, demonstrating the limited influence of these moments on stiffness modifications in the rear section. This aligns with the Spearman correlation analysis, which shows that, unlike the frontal section, stress at the BRT in the rear section, associated with counteracting bending moments to the external load, does not positively correlate with stiffness. Additionally, the rear section, which contains only two inflatable chambers, maintains similar geometrical attributes regardless of inflation, resulting in consistent geometric moments of inertia across various inflations. Consequently, geometrical moments of inertia did not significantly influence differences in stiffness observed across the configurations.

In the rear section without inflation, we observed that as y increased, the deflection in the rear section (y_r, refer to Figure 3.2) under external loads (refer to Figure 3.12(b)) and the length of the tensile region (l_{tr}) could increase, while the length of the compressive region (l_{cr}) could decrease.

In contrast, in the frontal section, the extension of both the tensile (l_{tf}) and compressive (l_{cf}) regions showed minimal changes in response to y-deflection during bending, as substantiated in Figure 3.13(a).

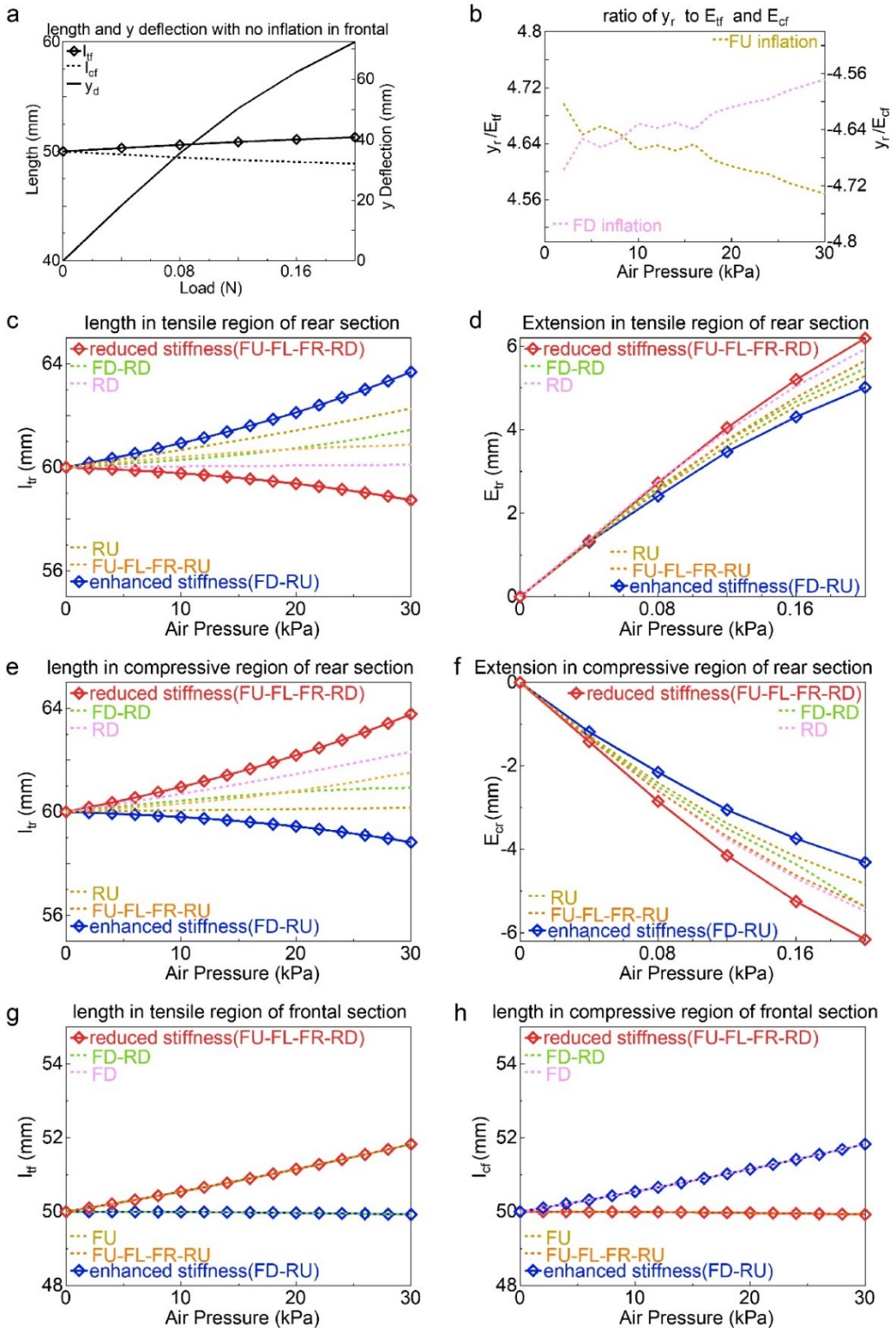

Figure 3.13 Detailed Extension Analysis and Its Effect on Stiffness (a) Changes in Length for Tensile and Compressive Regions Under Load in Frontal Section (b) Ratio of y deflection to Extension in Tensile and Compressive Region at frontal Section (c) Changes on Length for Tensile Region with Air Pressure (d) Changes on Extension for Tensile

Regions Under Loads (e) Changes in Length for Compressive Region with Air Pressure (f) Changes in Extension for Compressive gRegions Under Loads (g) Changes on Length for Tensile Region with air pressure in Frontal Section, and (h) Changes on Length for Compressive Region with air pressure in Frontal Section

Consequently, during the bending process under external loads in the rear section, the tensile region can be conceptualized as a spring being stretched, while the compressive region behaves similarly to a spring being compressed. This conceptual model aided in understanding the differential mechanical responses of these regions to external loads (Figure 3.12(c)).

During inflation of the RU and RD chambers in the rear section, we observed deflections in the y-direction (y_r), as well as corresponding stretching of the tensile region (l_{tr}) and compressive region (l_{cr}). Additionally, the ratios ($\frac{y_r}{E_{tr}}$ and $\frac{y_r}{E_{cr}}$) approach values of approximately 1.13 and -1.13, respectively, and continue to converge toward 1 or -1, as illustrated in Figure 3.12(d). This behavior suggests that, in the conceptual spring model, compared to the no-inflation configuration—where the springs in both the tensile and compressive regions remain at their original length of 60 mm prior to applying external loads—inflation in the rear section induces pretension in these springs, effectively setting them to new initial conditions. This influences their response under load and leads to altered mechanical behavior when external loads are applied. However, in the frontal section, the ratio was approximately 4.8, suggesting that inflation primarily causes bending rather than significant extension in these regions (refer to Figure 3.13(b)). Consequently, this does not lead to the formation of pretension, which would alter mechanical behavior under the same inflation.

In contrast, in the frontal section, the ratio remained constant at 4.8, suggesting that inflation did not significantly extend to these regions (refer to Figure 3.13(b)).

When the RU chamber was inflated, it significantly extended l_{tr} beyond its original length of 60 mm, creating pretension in the tensile region, as shown in Figure 3.13(c). This pretension (Δx) leads to an increase in the spring force (F_{ru}) compared to the non-inflated configuration (F_n), which is mathematically described in Equation (3.19). The enhanced spring force counteracted the mechanical extension caused by the external loads, thereby effectively reducing the extent of extension (E_{tr}). This mechanism helps maintain the structural integrity of the tensile region under stress, as observed in the smaller E_{tr} correlating with reduced y-deflection, indicating enhanced stiffness (Figure 3.12(e) and 3.13(d)).

$$\frac{F_{ru}}{F_n} = \frac{k \times (l_r + \Delta x)}{k \times l_r} \tag{3.19}$$

k: represents the assumed spring constant.

In contrast, inflation of the RD chamber resulted in the extension of l_{cr} beyond 60 mm, as shown in Figure 3.13(e), inducing a pretension (Δx) that increased the spring force in the compressive region, here denoted as $-F_{rd}$, as detailed in Equation (3.20). This increased spring force supported the compressive behavior under bending loads, enhancing E_{cr}. The resulting dynamics are such that a larger E_{cr} leads to greater y-deflection, as observed in Figure 3.12(e) and 3.13(f), implying reduced stiffness. This demonstrates that while the increased spring force helps maintain the structural configuration, it translates to reduced stiffness due to the nature of the compressive response.

$$\frac{-F_{rd}}{-F_n} = \frac{-k(l_r + \Delta x)}{-k \times l_r} \tag{3.20}$$

k: represents the assumed spring constant.

Spearman correlation analysis further validated these observations, indicating that stress at the TRP, which is associated with increased l_{tr}, correlates positively with stiffness. Conversely, stress at the BRP, which is associated with increased l_{cr}, correlated negatively with stiffness, suggesting a reduction in stiffness.

Chamber inflation in the frontal section can compress or stretch the rear section. When both inflation chambers are in either the tension or the compression region, they inhibit extension in the rear section. If they are not in the same region, they enhance the extension (Figure 3.11(a)), impacting the stiffness. However, the inflation in the rear section had a negligible effect on the lengths (l_{tr} and l_{cr}) of the frontal section (refer to Figures 3.13(g) and 3.13(h)).

The impact of RU chamber inflation on stiffness is intricately linked to the external load applied. At a 0.12 N load, the stiffness of the RU configuration aligns with or is slightly lower than that of the uninflated configuration (as depicted in Figure 3.2(a)). However, as the load increases beyond 0.12 N, the stiffness of the RU configuration exceeds that of the uninflated setup. We infer that, at lower loads, the length does not reach a point at which it can sufficiently resist the external load. With increasing load, the length gradually increased, gaining the capacity to effectively counteract the external load.

- Middle section

The middle section, situated between areas unaffected by inflation, experienced stress changes primarily due to inflation in the frontal and rear sections. This inflation creates bending moments that either counteract or complement the external load, resulting in stiffness variations. However, the bending moments induced by chamber inflation M_{qm} in the middle section had a significantly lower impact than those in the frontal (M_{qf}) and rear (M_{qr}) sections, indicating a lesser role in resisting external loads. Moreover, the influence of chamber inflation on the geometry of the hollow central duct within the middle section was minimal, suggesting that the bending moments play a limited role in adjusting the stiffness. Spearman's correlation analysis revealed that stress at the BMT (associated with

opposing bending moments to the external load) showed a modest positive correlation with stiffness. Conversely, stress at the TMP (linked to bending moments aligned with the external load) showed a slight negative correlation with stiffness.

Our analysis indicated that stress changes in the middle section were primarily caused by inflation activities in the frontal section. FEM simulations suggested that stress induced by inflation in the frontal section surpassed that in the rear section, impacting the middle section more significantly. Comparing the enhanced and reduced stiffness configurations, it was clear that increased inflation led to a more pronounced influence and distinct stress variation in the middle section (refer to Figure 3.12(f)).

Building on our insights from the FEA simulation concerning effective air chamber pairs for both enhanced and reduced stiffnesses, our next objective was to quantify how effective stiffness modulation affects the tip-bending angle, time response, and tip force.

- Tip-Bending Angle

In the non-inflation configuration (Figures 3.7(a) and (b)), the observed bending angles for both the frontal and rear sections exceeded 90°. This suggests the potential of the soft actuator to enhance the field of view and operational space for endoscopic surgery. The frontal section, exhibiting a maximum tip-bending angle of 91°, effectively offers the surgeon a 180° viewing and operational range due to its symmetrical chamber configuration. This range can facilitate crucial surgical maneuvers, particularly in MIS. Furthermore, the 94° bending angle of the rear section highlights the capability of the soft actuator to navigate and access the surgical target area, such as the prostate, during prostatectomy by bending around the bladder.

In the enhanced stiffness configuration (Figures 3.7(c) and (d)), the diminished tip-bending angle in the rear section was likely due to inflation of the opposite chamber, the RU chamber. Its expansion occupied a significant portion of the hollow central space that housed the endoscope. This inflation physically restricts the expansion of the RD chamber and hinders actuator bending [20]. Moreover, the inflation of the counteracting RU chamber exerts a bending tendency in the opposite direction. At an inflation pressure of 30 kPa in the RU chamber, this counter-bending effect minimizes the differences in tip-bending angles at identical pressures during both inflation and deflation phases, thereby ameliorating pneumatic hysteresis. While the performance of the frontal section also reflects an overall increased stiffness, the effects are comparatively subtle, manifesting as minor reductions in both tip-bending angle and pneumatic hysteresis.

In the reduced stiffness configuration (Figures 3.7(e) and (f)), inflation of the opposite chamber (FU) and adjacent chambers (FL and FR) substantially reduced the available space in the central hollow region. The inserted endoscope, compressed by these chambers, further limits the expansion of the FD chamber, thereby affecting actuator bending [15]. Additionally, inflation of the FU chamber, which drives bending in the opposite direction to that of the FD chamber, further restricts the maximum tip-bending angle. This counteraction resulted in pronounced improvements in pneumatic hysteresis. By contrast, the rear section remained relatively unaffected, maintaining its performance metrics from the non-inflation configuration.

The observed outcomes highlight the importance of selecting appropriate stiffness configurations for MIS applications. Surgeons must carefully consider both bending angles and pneumatic hysteresis when choosing between enhanced- and reduced stiffness strategies, ensuring the actuator aligns with the specific requirements of the surgical procedure.

- Time Response

Our investigation of the time response of the soft actuator in three configurations (enhanced stiffness, reduced stiffness, and no-inflation) revealed significant effects of stiffness and chamber dynamics on responsiveness.

In the enhanced stiffness configuration (Figure 3.8(d)), the actuator consistently achieved the target angle across a frequency range of 0.1-0.5 Hz. While increased stiffness is a contributing factor, a crucial element is the sustained minimum air pressure of 30 kPa in the FD chamber. This pressure threshold mitigated the inertia observed at lower pressures, enabling better performance during higher-frequency cycles, as shown in Figure 4. For instance, the importance of this factor was further emphasized at a 0.5 Hz frequency. In the initial cycle at a 0.5 Hz frequency, starting from zero pressure, the actuator did not achieve the desired angle. However, subsequent cycles beginning at the 30 kPa threshold demonstrated improved performance, reaching the targeted angles. Conversely, in the non-inflation configuration (Figure 3.8(a)), the lack of a minimum pressure base resulted in the inconsistent ability of the actuator to reach the desired angle.

The reduced stiffness configuration (Figure 3.8(e)) further compromised performance due to the concurrent inflation of the adjacent chambers (FU, FL, and FR), limiting the bending ability and reducing the maximum tip-bending angle. Notably, this configuration exhibited a reduced phase lag between the tip-bending angle and air pressure changes, with a discrepancy of approximately 0.15 s.

Our analysis suggests that while stiffness modifications influence the behavior of the actuator, specific pneumatic chamber configurations play a more decisive role. In practical MIS scenarios, while modulating stiffness is essential, the accompanying time response must also be considered. Under circumstances requiring increased stiffness coupled with a superior response, the enhanced stiffness configuration proved effective. This multifaceted understanding of the actuator, derived from both chamber configurations and stiffness parameters, provides the necessary insights for optimizing MIS applications.

- Tip Force

When assessing tip force variations, we found a clear correlation with the tip-bending angle across the different configurations. For the no-inflation configuration, the ability of the soft actuator to exert approximately 1 N of tip force in both the front and rear sections shows potential utility in MIS scenarios. These forces are substantial for tasks such as tissue manipulation, cutting, and retraction during surgery. The presence of hysteresis with air pressure (similar to the tip-bending angle experiments) suggests that soft actuator performance is not solely governed by the current input air pressure, underscoring the

importance of understanding these dynamics for precise actuation during MIS. For the enhanced stiffness configuration, the recorded reduction in tip force within the rear section can be attributed to the inflation of the opposite chamber, RD. This inflation likely induced an antagonistic force or resistance, resulting in the observed decrease in tip force. More importantly, the improvement in hysteresis highlights the potential benefits of such configurations in terms of consistent force application, which can be crucial for delicate surgical procedures. More intricate dynamics are observed in the reduced stiffness configuration. The pronounced decline in the frontal section's maximum tip force can be traced to interference from the opposing chamber, FU, and the adjacent chambers, FL and FR. Their concurrent inflation may limit the ability of the actuator to effectively generate force. Despite the reduction in tip force in the reduced stiffness configuration, we observed a notable improvement in hysteresis. This finding suggests that this configuration may be particularly advantageous in scenarios where consistent and predictable actuation is more critical than higher tip force.

The intertwined nature of the tip force and bending angle is crucial for determining the suitability of an actuator for MIS. The challenge lies in tailoring the stiffness of the actuator to meet the dynamic requirements of MIS while balancing efficiency and patient safety.

- Results of Perturbation-Resisting Experiment in a Bladder–Prostate Model

The results of the experimental outcomes using a bladder–prostate model to evaluate the impact of effective stiffness configurations on single-port transvesical prostatectomy showed that stiffness modulation plays a pivotal role in the ability of the actuator to withstand and adapt to external disturbances.

The results indicate that noise significantly increases z-direction deformation across all configurations, causing erratic oscillations in the x- and y-directions. Notably, the enhanced stiffness configuration showed the least deformation in the z-direction (under 0.6 mm), indicating superior resistance to vertical disturbances. This characteristic is particularly advantageous for maintaining operational stability and precision during surgical tasks. Conversely, the reduced stiffness configuration, with the highest deformation nearing 2 mm, suggests higher flexibility, which could be beneficial for navigating through constrained or highly irregular spaces such as maneuvering around organs or navigating through tissue passages.

Endoscopic and monitor camera observations, provided additional qualitative insights. The reduced stiffness configuration exhibited significant visual field instability, indicating its susceptibility to disturbances. However, this flexibility could be beneficial in specific surgical scenarios requiring delicate navigation through soft or sensitive tissues, where minimizing force exertion on the surrounding environment is crucial. The enhanced stiffness configuration demonstrated minimal visual field disturbances, affirming its utility in situations demanding high stability and precision.

These findings underscore the importance of selecting the appropriate stiffness configuration based on the surgical context. Enhanced stiffness is preferable for tasks requiring precision and stability, while reduced stiffness may be advantageous for

navigating complex anatomical structures. This adaptability highlights the potential of stiffness-modulated soft actuators to improve the versatility and safety of MIS.

- Limitation and Future work

Limitation 1 Discrepancy in Stiffness Prediction

Our current FEA model in COMSOL Multiphysics exhibits limitations in accurately simulating the stiffness of the soft actuator under high-load conditions, showing discrepancies between predicted and experimentally observed stiffness values. This limitation restricts our ability to precisely predict and control stiffness.

Future Work to Address Limitation 1

We plan to develop and integrate an advanced control system to enhance our capability to dynamically modulate and precisely control the stiffness of the actuator. This system aims to adjust inflation levels within the chambers in real-time, thereby fine-tuning the stiffness of the actuator to adapt to external loads. This approach indirectly facilitates a more accurate approximation of the stiffness of the actuator by enabling on-the-fly adjustments that emulate expected physical responses under varying load conditions. By improving the precision of actuation, we anticipate a better correlation between the real-world performance of the actuator and its simulated projections, especially under conditions that exceed our current simulation model's optimal load range. This strategy aims to bridge the gap between empirical observations and FEA predictions, particularly at higher loads, thereby enhancing the overall predictive accuracy and utility of our simulations in practical applications.

Limitation 2 Limited Scope of Practical Testing

While we have conducted preliminary tests in a physical simulator to approximate real-world conditions, these experiments fall short of fully validating the stiffness modulation functionality in actual surgical scenarios. Such scenarios are complex and vary significantly, necessitating extensive validation to ensure the practical applicability and reliability of the actuator in clinical settings.

Future Work to Address Limitation 2

We plan to conduct comprehensive practical evaluations in environments that closely mimic actual surgical conditions. This includes testing with animal models and synthetic organs to simulate a range of surgical challenge. These tests aim to rigorously assess the performance, adaptability, and reliability of the actuator under conditions that closely replicate actual surgical procedures, thereby providing stronger validation of its potential for clinical applications in MIS.

While our study has certain limitations, it also opens avenues for applying the same FEA model to various scenarios beyond those tested. The flexibility and adaptability of our FEA model suggest its potential applicability to a range of soft actuator designs and configurations. Further research is needed to explore these possibilities and extend the utility of our model to diverse surgical applications and actuator designs. Addressing these

limitations and expanding the model's applicability is crucial for advancing the field of soft robotics in MIS.

3.6. Conclusions

This study elucidated the mechanism of stiffness modulation in multiple antagonistic chambers by constructing an FEA simulation model for soft actuators used in single-port transvesical prostatectomy. The model examined the effects of stress distribution across the hollow center duct structure of a soft actuator on stiffness modulation. This methodological approach enhances our understanding of the mechanical behavior of actuators for precise stiffness modulation and advances the design of soft actuators for complex MIS. Furthermore, the study assessed the impacts of different stiffness modulation strategies on key performance metrics of the soft actuator, including tip-bending angle, response dynamics, and tip force. Notably, an enhanced stiffness configuration was found to be particularly effective, demonstrating superior performance in essential metrics such as tip-bending angle, response time, and tip force. The utility of various stiffness modulation strategies in single-port transvesical prostatectomy was validated within the bladder–prostate model, underscoring the pivotal role of stiffness modulation in enabling the actuator to adapt and respond effectively to external disturbances. The enhanced stiffness configuration, in particular, shows promising applicability in various surgical settings, emphasizing the importance of customizable stiffness adjustments to meet the specific requirements of surgical procedures.

4. Load Sensing and Stiffness Adjustment for Soft Actuator in MIS

4.1. Preface

Chapter 5 introduces an advanced neural network mechanism designed to address the need for precise stiffness selection based on external loads, particularly those from neighboring organs. This chapter explores the non-linear dynamics of actuators and the unpredictability of surgical environments, highlighting our implementation of an environment exploration strategy. Combined with the neural network's inverse dynamics model, this strategy ensures precise stiffness adjustment in response to varying external loads and endoscopes. Portions of this work were published under the title "Neural Network-Based Active Load-Sensing Scheme and Stiffness Adjustment for Pneumatic Soft Actuators for Minimally Invasive Surgery Support" in a journal paper.

4.2. Introduction

In our study, we explored the impact of external loads or resistance from surrounding organs and tissues on pneumatic soft actuators integrated with endoscopes. These actuators sometimes require increased stiffness to counteract these loads. However, excessive stiffness induced by high air pressure in both antagonistic chambers may lead to potential organ damage and air leakage from the actuators [12]. Thus, estimating the external load is crucial for selecting appropriate stiffness levels [18], [37]. Traditional load sensors, which compromise the omnidirectional compliance of pneumatic soft actuators, are unsuitable for this application [38]. Instead, researchers have turned to soft sensors made from compliant materials, which are easier to integrate due to their high compliance [39], [40], [41]. These sensors detect changes in electrical properties like resistance or capacitance due to material stress and strain, but manufacturing these actuator-sensor combinations presents significant challenge. Improper sensor placement can damage the actuator and cause leaks [38]. Moreover, certain soft sensors are restricted to environments involving magnetic or bright light sources [42].

Recent advancements have seen a growing interest in soft actuators equipped with embedded sensing mechanisms [43], [44], [45], [46], incorporating features like fiber embroidery [43], thin biphasic metal films [44], conductive fluids [45], or wires [46] within the actuator. These systems use analytical models based on mechanical or electrical principles to monitor actuator movement or load. For instance, a soft pneumatic actuator capable of self-sensing its external load has been developed [44], employing a sensing layer that is challenging to fabricate. This sensing mechanism, highly sensitive to dynamic signals such as vibrations or impact forces, struggles to measure static external loads crucial for determining stiffness.

Furthermore, the accuracy of these analytical models poses a significant challenge in minimally invasive surgery (MIS). For example, when different flexible endoscopes are inserted into a soft actuator, the characteristics of the actuator—such as bending, stiffness, and deformation—alter, necessitating adjustments to the analytical model. Internal

interference between the endoscope and the actuator complicates these characteristics, especially as the relationship between stiffness and bending angle is nonlinear [12], [19].

To overcome these challenge, we propose using neural networks (NNs), which excel at modeling nonlinearity and uncertainty [47], [48]. Our approach, which eschews traditional physical sensors, utilizes a relationship between target physical quantities and a set of state variables affected by or interacting with these quantities. This relationship, learned from the collected raw data of a soft actuator [47], enables a NN-based system to predict bending angle and contact force from air pressure readings. Although NNs accurately predict scenarios resembling the training data, they can deviate significantly under real test conditions. This discrepancy stems not from the NNs' learning capabilities but from the nonlinearity of the soft actuating system and the uncertainty of its interaction with the environment [48], a common issue in real-world robotic applications [47].

In this context, we introduced a NN-based active-sensing and stiffness adjustment scheme for a MIS-support pneumatic soft actuator with antagonistic chambers, enabling three degrees of freedom (DoFs) in control. This setup included a strategy for environmental exploration to enhance sensing robustness, determining the minimal exploration sequence through estimation errors and minimal changes in bending angles. An inverse dynamics model based on NNs was also established to estimate air pressure from the predicted load and desired stiffness, advancing our understanding of soft actuator design for MIS and paving the way for more effective medical robotic tools.

4.3. Materials and Methods

4.3.1 Measurement of bending angle and stiffness for the soft actuator

The measurement methodology for our soft actuator prototype experiments is outlined in Figure 4.1. The design and fabrication details of the soft actuator are described in Chapter 3.3. The actuator features two degrees of freedom (DoFs). DoF 1 comprises a front upper chamber (FU, see Figure 3.1) and a front lower chamber (FD, see Figure 3.1), while DoF 2 consists of a front left chamber (FL, see Figure 3.1) and a front right chamber (FR, see Figure 3.1). Since DoFs 1 and 2 share identical bending characteristics and structure, except for their orientation, they provide a robust model for study. For instance, inflating FU and FD with 10 kPa and 100 kPa respectively causes the actuator to bend by 41.4 degrees in the x-direction of DoF 1, as shown in Figure 4.1. Similarly, inflating FL and FR with 10 kPa and 100 kPa respectively also results in a 41.4-degree bend in DoF 2. We focused on DoF 1 (FU and FD) for detailed investigation. Due to the symmetry of the chambers FU and FD, asymmetric air pressures can induce movement in the respective bending direction. Hence, only one bending direction was measured. The air pressure for FU (P_FU) was varied from 0 to 30 kPa, while for FD (P_FD), it ranged from 0 to 110 kPa. For every 10 kPa increment in pressure on either side, bending angle and stiffness were recorded, yielding a total of 48 distinct data points.

Before any external load was applied, an endoscope was inserted into the soft actuator, and the initial bending angle was measured as bending angle_original (bending angle_o). Once all chambers reached a steady state, the system—comprising the endoscope and soft actuator—was subjected to various external loads (0 N, 0.15 N, 0.17 N, 0.22 N,

0.27 N, 0.56 N, 1.06 N). Subsequently, the endoscope was stabilized again, and the resulting angle was noted as bending angle_end (bending angle_e). The horizontal displacement of the endoscope was recorded as -x deformation. All coordinate data was captured using ArUco markers (2D markers, [55]) placed in front of all soft actuators. These markers were photographed using a camera (USB8MP02G-SFV, ELP camera, Ailipu Technology Co., Ltd, CN) during the bending process. The calculations for bending angle_o, bending angle_e, and -x deformation were performed using OpenCV with Python 3.8.12.

The impact of endoscope diameter on the expansion of the soft actuator's chambers was also assessed by inserting three different types of endoscopes (Ambu® aScopeTM 4 Broncho Slim, diameter: 3.8 mm; Ambu® aScopeTM 4 Broncho Regular, diameter: 5.0 mm; Ambu® aScopeTM 4 Broncho Cysto, diameter: 5.4 mm; Ambu Inc., DK, as shown in Figure 4.1 left). Notably, the 5.4 mm-endoscope, typically used for bladder surgery, exhibited lower stiffness compared to the 3.8 mm and 5.0 mm endoscopes, which are used for trachea surgery.

In an MIS procedure, the flexible endoscope's lens should be kept a distance from the front (axial direction) organs or tissues to provide surgical view for surgeons. Therefore, the external load with axial direction is very small, which allow us to focus on the external load with horizontal direction. Adjusting the stiffness on -x direction could help the flexible endoscope to resist different external load on -x direction. The overall stiffness with -x direction (K) of the soft actuator and endoscope is calculated by Equation (4.1). The K cannot contain the stiffness with other direction such as axial direction (-y direction). The load of -x direction is the partial load in the horizontal direction calculated by the angle between the rope and the horizontal direction.

$$K = \frac{-x\ Load}{-x\ Deflection} \tag{4.1}$$

$-x\ Load$: load for -x direction; $-x\ Deflection$: deflection after applying load for -x direction

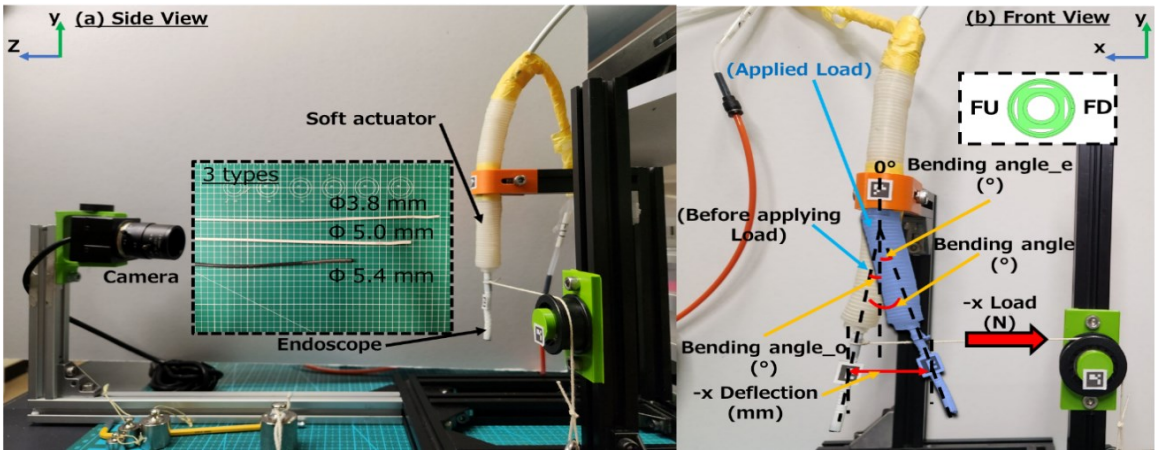

Figure 4.1 The measurement method of soft actuator (a) side view, (b) front view.

4.3.2 A load active-sensing scheme and environment exploration strategy

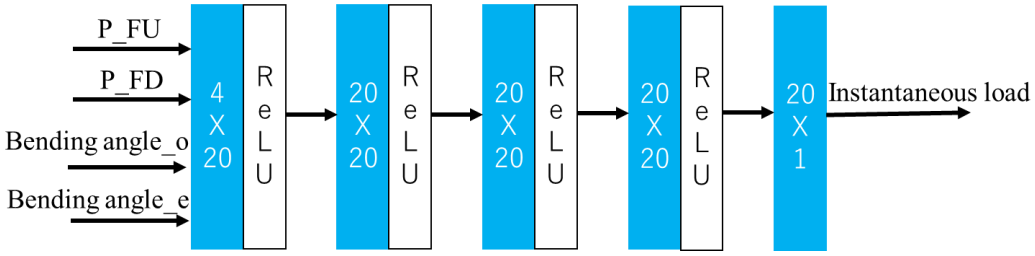

Figure 4.2 The architecture of the load active-sensing scheme

As outlined in the Introduction Section 4.2, accurately estimating external loads is crucial for selecting the appropriate stiffness of a soft actuator. This chapter proposes a load active-sensing scheme.

It is determined that the essential set of input features for the neural network (NN) includes P_FU, P_FD, bending angle_o, and bending angle_e. Firstly, inflating antagonistic chambers can alter the stiffness, which, though angle-dependent, is a preferred feature. The adjustable stiffness allows the actuator to adapt to various scenarios, including differing endoscope types and external loads. Additionally, the soft actuator's angle may also change due to the inflation of these chambers.

Secondly, similar to other self-sensing studies [38], [47], the air pressure applied to the chambers influences the bending of the soft actuator, which is affected by the combined stiffness of the actuator body and the inserted endoscope, along with the external load. Although the actuator's stiffness is angle-dependent, it is not a freely adjustable variable; hence, the external load becomes the critical determining factor.

For these reasons, the pressures applied to the antagonistic chambers and the angles before and after applying external loads are necessary input features. However, these inputs alone are insufficient for predicting the external load, as they are influenced by the combined effects of the overall stiffness of the soft actuator with the endoscope and the external load. This combined effect is further disentangled in the inverse dynamics model as described in Section 4.3.3, utilizing endoscope information.

Figure 4.2 illustrates the architecture of the load active-sensing scheme. The input data shape is (1,4). The three hidden layers each consist of 20 nodes, and the output layer has a single node representing the instantaneous load. The activation function used is ReLu. The active-sensing schemes are developed using Python 3.9.12 64-bits and PyTorch "1.12.1" with CUDA "11.7". The Adam optimizer is used with a learning rate of 1×10^-5, and the total epochs number 80,000. The training data includes all data points with external loads of 0, 0.17, 0.27, 0.56, and 1.06N for endoscopes with diameters of 0, 3.8, and 5.4 mm, while the verification data includes all data points with external loads of 0.15 and 0.22 N for 5 mm endoscopes. A prediction within 10% deviation from the ground-truth external load is defined as successful.

An environment exploration strategy is explored to enhance the robustness of the sensing. The minimal exploration sequence is determined based on the prediction error. Once the network estimates the instantaneous load based on the current state (current P_FU, P_FD, bending angle_o, bending angle_e), a sequence of actuation is executed to explore the environment to address the effects of the system's nonlinearity and the uncertainty in the interaction between the soft actuator and its environment. Taking FD as an example, $P\_FD(n)$ is calculated by Equation (4.2).

$$P\_FD(n) = current\ P\_FD + n \times m\_step \tag{4.2}$$

A positive value of n means forward exploration (e.g., +1, +2…), while a negative value means backward exploration (e.g., -1, -2), m_step is a minimal exploration step (10 kPa in this study). Six different exploration sequences ("+1, +2", "+1, +2, +3", "+1, +2, +3, +4", "-1, +1", "-1, -2, +1, +2", "-1, -2, -3, +1, +2, +3") are investigated. The biggest step number of exploration sequence is 6 and the smallest step number of exploration sequence is 2. The average of all the predicted external load values of all the steps in a sequence is used as the external load of the sequence.

4.3.3 A NN-based inverse dynamics model for stiffness

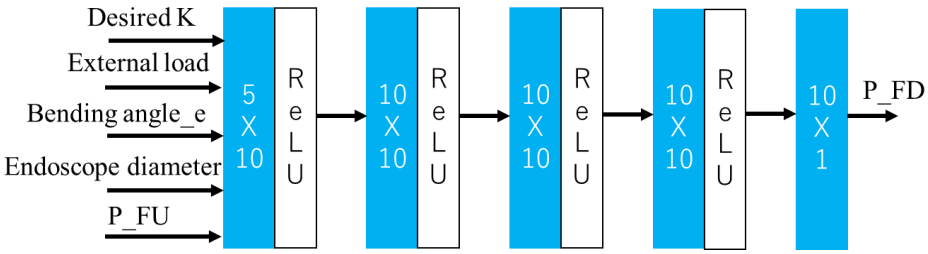

Figure 4.3. The architecture of NN-based inverse dynamic model

In addition to the estimated external load, desired stiffness (K), and bending angle_end (bending angle_e), the diameter of the endoscope also impacts the overall stiffness of the soft actuator-endoscope system. Consequently, this parameter is included as an input to the neural network. The appropriate stiffness selection is determined based on the external load. The stiffness calculated from P_FU, P_FD, endoscope diameter, bending angle_e, and external load serves as the basis for a forward dynamic model for stiffness. Conversely, when a specific stiffness is required, calculating P_FD involves a complex, nonlinear inverse dynamic model for stiffness, which is challenging to model. Neural Networks (NNs) are commonly employed to solve such inverse dynamic models [43]. To control the soft actuator to achieve the desired stiffness, we utilize a multilayer perceptron (MLP), a type of fully connected feedforward artificial neural network (ANN) [48]. Inputs to the MLP include desired K, external load, bending angle_e, and the diameter of the endoscope.

Figure 4.3 showcases the architecture of this model, developed using Python 3.9.12 64-bits. The activation function is ReLu, and the optimizer is the Adam optimizer with a learning rate of 1×10^{-3}, the model is trained over 50,000 epochs. This section utilizes the

same dataset as the load active-sensing scheme section for both training and verification; however, it incorporates additional target stiffness, external load, and endoscope diameter values into the model's input data. The desired stiffness for both data sets is computed according to Equation 4.1. Simultaneously, we exclude bending angle_e from the input data of the model to refine the prediction focus.

4.4. Results

4.4.1 Preliminary result - bending angle_o of soft actuator before applying external load

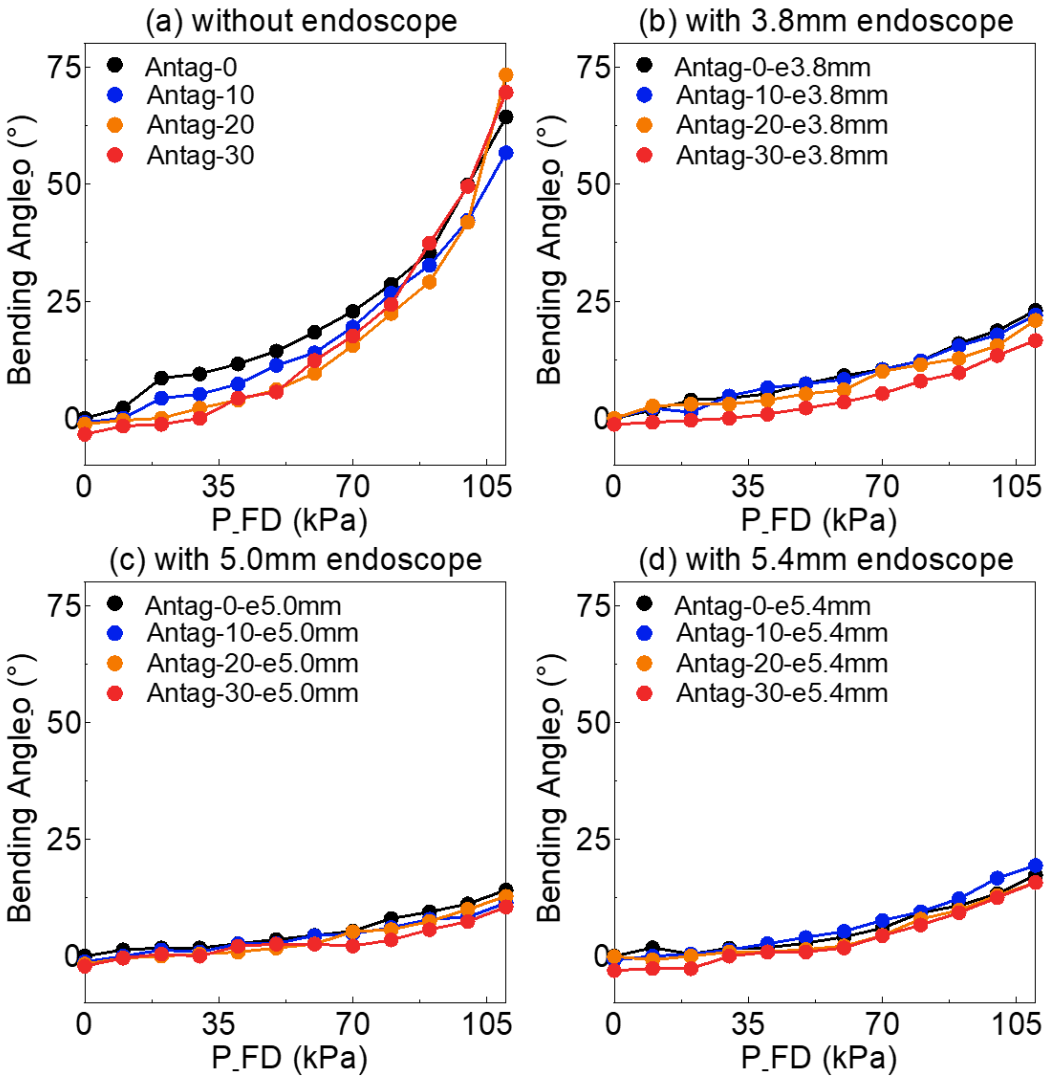

Figure 4.4 The variation of soft actuator's bending angle before applying external load under different sets of FU and FD air pressure (a) without endoscope: without inserting endoscope into soft actuator for experiment, (b) with 3.8 mm endoscope: inserting 3.8 mm endoscope into soft actuator for experiment, (c) with 5.0 mm endoscope: inserting 5.0 mm

endoscope into soft actuator for experiment, (d) with 5.4 mm endoscope: inserting 5.4 mm endoscope into soft actuator for experiment.

Figure 4.4 (a) illustrates the bending angle_o of the soft actuator without an endoscope, under varying levels of agonist pressure (P_FD), which is plotted along the x-axis (range 0-110 kPa), and antagonist pressure (P_FU), labeled as Antag-0, 10, 20, 30 in the legend. Figures 4.4 (b), (c), and (d) display the bending angle_o of the soft actuator equipped with endoscopes of diameters 3.8, 5.0, and 5.4 mm, respectively.

The data show that with a constant P_FU, the bending angle_o increases as P_FD increases, with the rate of increase becoming more pronounced from 70 kPa onwards. Conversely, with a constant P_FD, an increase in P_FU generally reduces the bending angle_o, demonstrating that P_FU negatively impacts the bending angle_o. Despite the bending angle for Antag-30 being higher than that for Antag-0, 10, 20 between 70-110 kPa as seen in Figure 4.4 (a), higher P_FUs tend to significantly decrease the bending angle. Moreover, the diameter of the endoscope (e3.8mm, e5.0mm, e5.4mm) markedly influences the bending angle_o; a larger diameter endoscope exerts a stronger effect on the bending angle_o, as evident from the comparison of bending angle_o between Antag-0 (67.3°) and Antag-0-e5.4mm (17.3°) at 110 kPa.

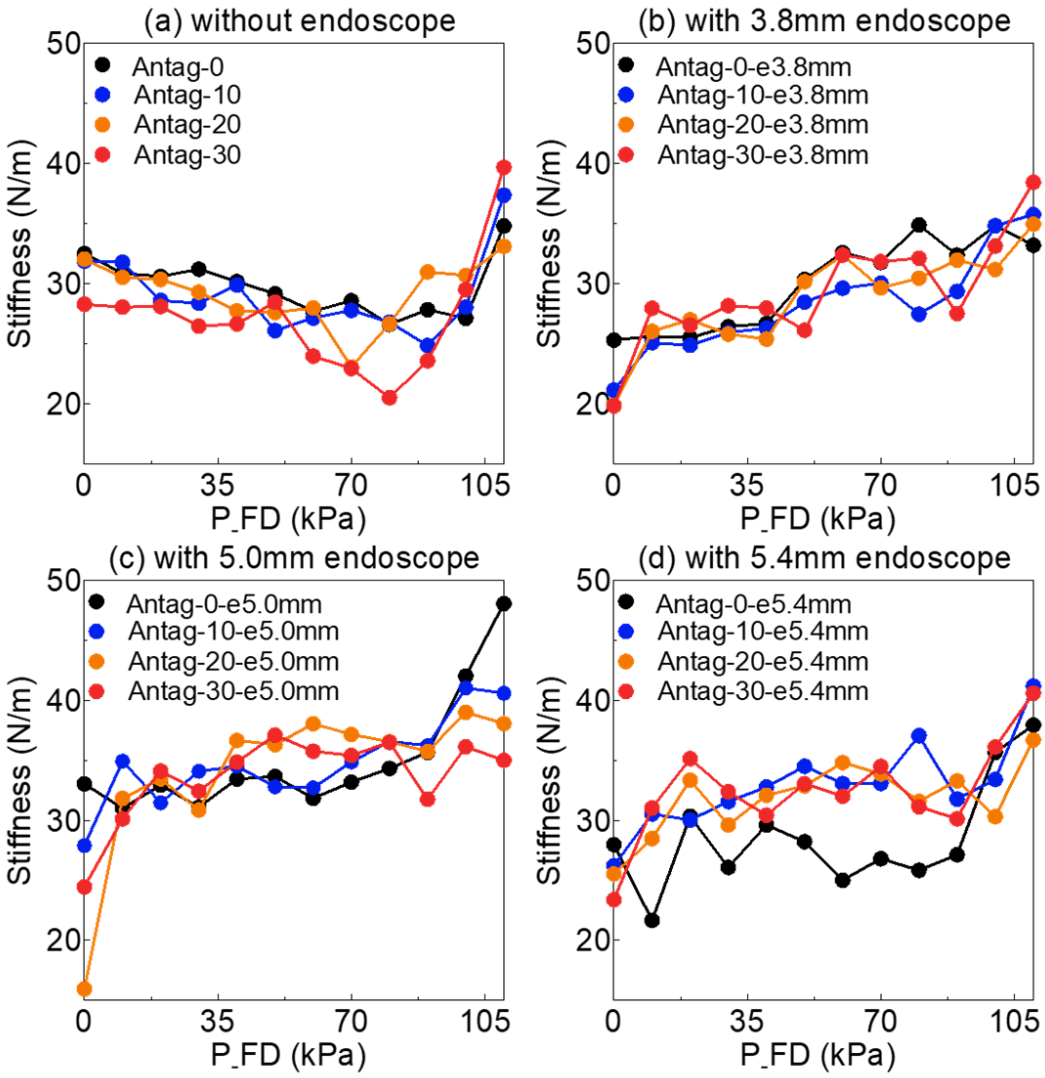

Figure 4.5 The variation of soft actuator's stiffness under different sets of FU air pressure and FD air pressure (a) without endoscope: without inserting endoscope into soft actuator for experiment, (b) with 3.8 mm endoscope: inserting 3.8 mm endoscope into soft actuator for experiment, (c) with 5.0 mm endoscope: inserting 5.0 mm endoscope into soft actuator for experiment, (d) with 5.4 mm endoscope: inserting 5.4 mm endoscope into soft actuator for experiment.

4.4.2 Preliminary result - bending angle_o of soft actuator before applying external load

Figure 4.5 (a) displayed the stiffness of the soft actuator under varying agonist pressures (P_FD) along the x-axis (ranging from 0 to 110 kPa) and different antagonist pressures (P_FU), labeled as Antag-0, 10, 20, 30, without an endoscope. Figures 4.5 (b), (c), and (d) demonstrated the total stiffness of the soft actuator when paired with endoscopes of diameters 3.8 mm, 5.0 mm, and 5.4 mm, respectively.

The data from Figure 4.5 indicated that the same P_FU exerted varying effects on stiffness depending on the P_FD value. Particularly, as P_FD increased beyond 90 kPa, the stiffness of the soft actuator generally rose with increasing P_FD. The influence of P_FU on the stiffness of the soft actuator was nonlinear. When the air pressure was below 90 kPa, this impact differed from expectations, especially in the absence of an endoscope, with P_FD diminishing the stiffness of the soft actuator (under 90 kPa).

Furthermore, different combinations of P_FU and P_FD led to variations in bending angle_o, significantly impacting the internal structure of the soft actuator and, consequently, its stiffness. Figure 4.6 illustrated the relationship between bending angle_o and the stiffness of the soft actuator. The figure showed that the stiffness for all three types of endoscopes exceeded 30 N/m at a considerable bending angle_o (above 8°). Even when the stiffness of the actuator without an endoscope did not reach 30 N/m, there was a gradual increase in actuator stiffness for bending angles_o greater than 30°.

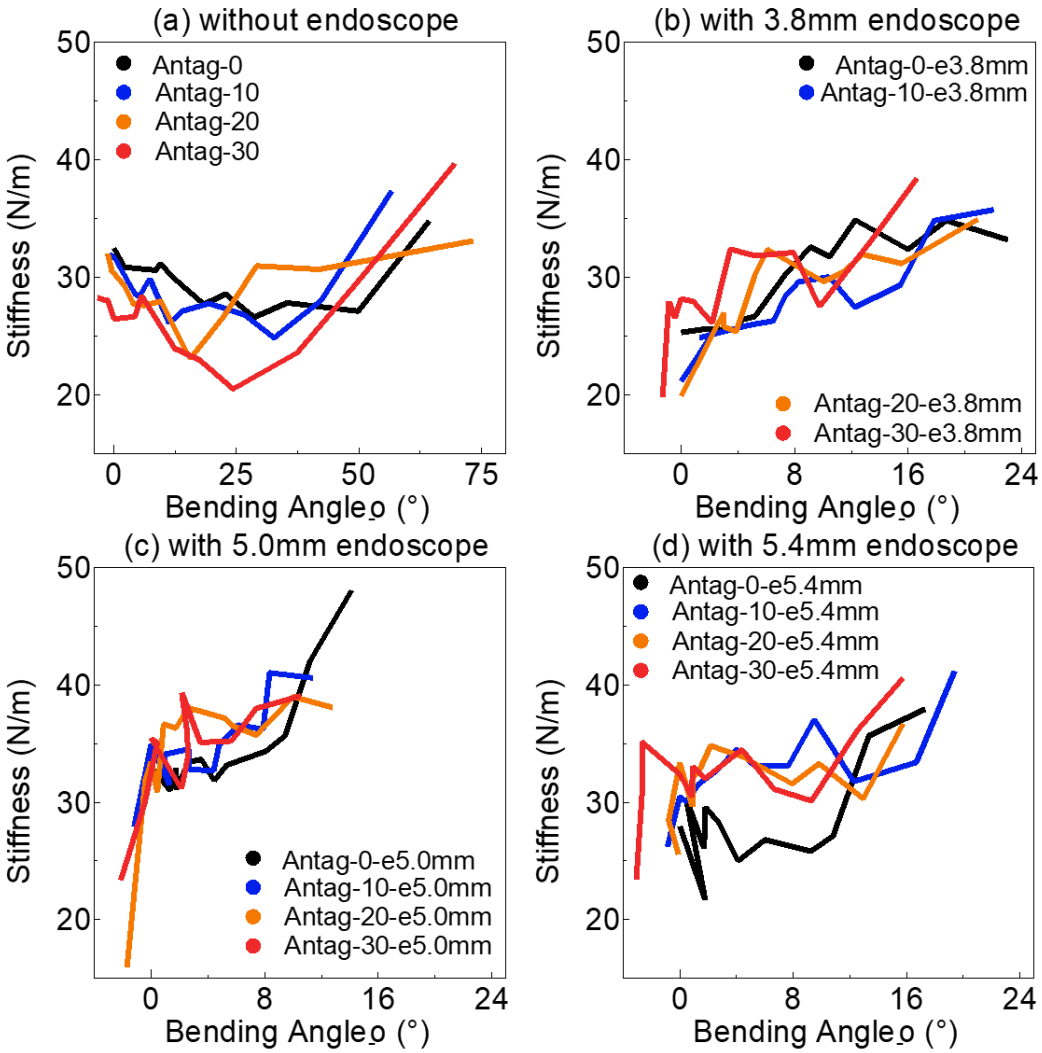

Figure 4.6 The variation of soft actuator's stiffness under different bending angle_o (a) without endoscope: without inserting endoscope into soft actuator for experiment, (b) with

3.8 mm endoscope: inserting 3.8 mm endoscope into soft actuator for experiment, (c) with 5.0 mm endoscope: inserting 5.0 mm endoscope into soft actuator for experiment, (d) with 5.4 mm endoscope: inserting 5.4 mm endoscope into soft actuator for experiment.

4.4.3 Preliminary result - bending angle_o of soft actuator before applying external load

Figure 4.7 depicted the results of the load active-sensing scheme, where the true load in Figure 4.7 (a) and 4.7 (b) were 0.15 N and 0.22 N, respectively. The mean and variance of different exploration sequences were shown in Table 4.1 (for 0.15 N) and Table 4.2 (for 0.22 N).

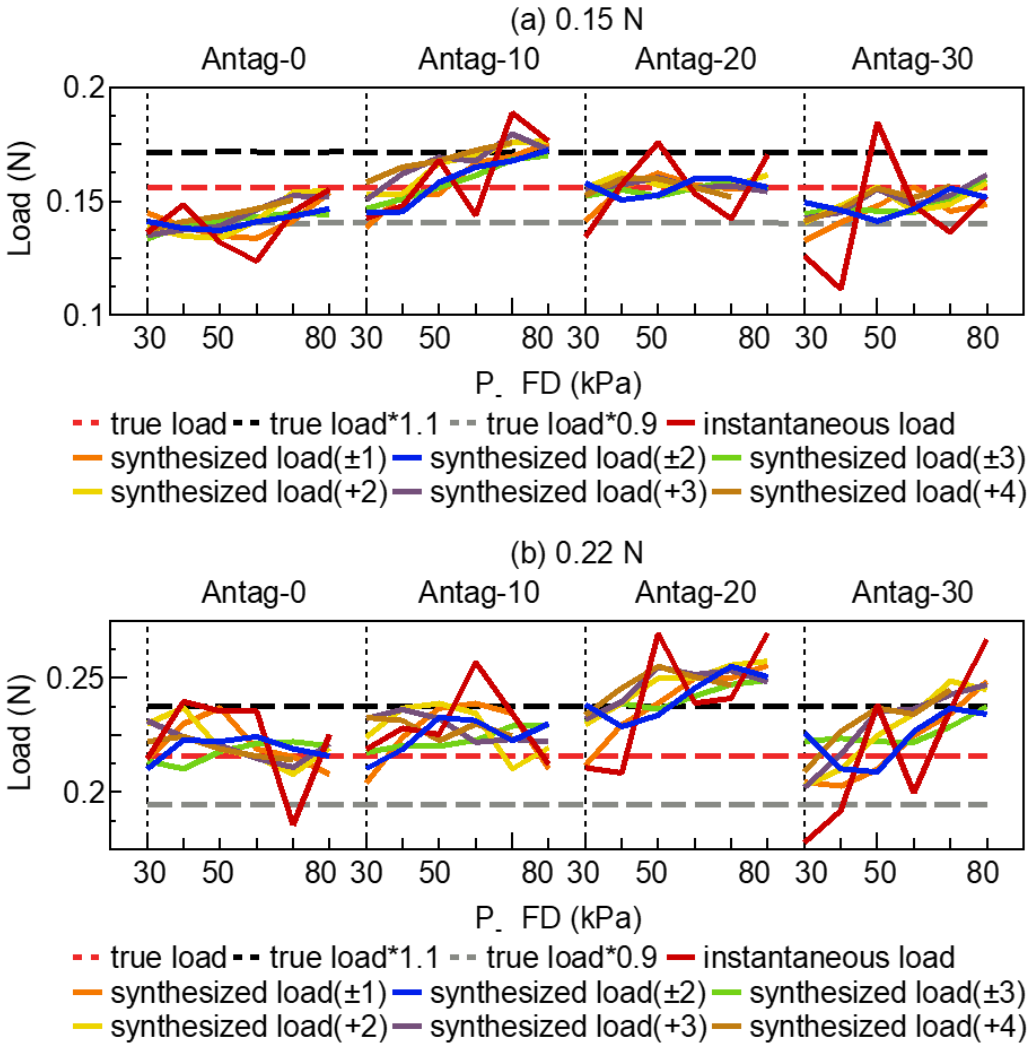

Figure 4.7 The test data of load active sensing scheme with 5.0 mm endoscope from NN (a) 0.15 N, (b) 0.22 N.

Figure 4.7, along with Tables 4.1 and 4.2, demonstrate that compared to the instantaneous load derived solely from the current state, the synthesized load (±n or +n) more closely approximates the true load. Furthermore, the synthesized load (±n, +n) showed reduced variance, indicating that larger errors in the neural network's (NN) output were mitigated through the exploration strategy. For instance, as shown in Table 4.2, the variance for an exploration sequence of length 4 was smaller than that of length 2 (total: synthesized load (±2) vs. synthesized load (±1): 0.012 vs. 0.016). Similarly, the variance for a sequence of length 3 was smaller than that of length 2 (total: synthesized load (+3) vs. synthesized load (+2): 0.014 vs. 0.017). However, the synthesized load (±3) also increased the likelihood of deviating from the ground-truth load estimation. Among sequences of the same length, such as ±2 and +4, or ±1 and +2, the forward inflation strategy (like +4, +2) resulted in greater variance (±2 Antag-0 vs. +4 Antag-0: 0.003 vs. 0.005, Table 4.1).

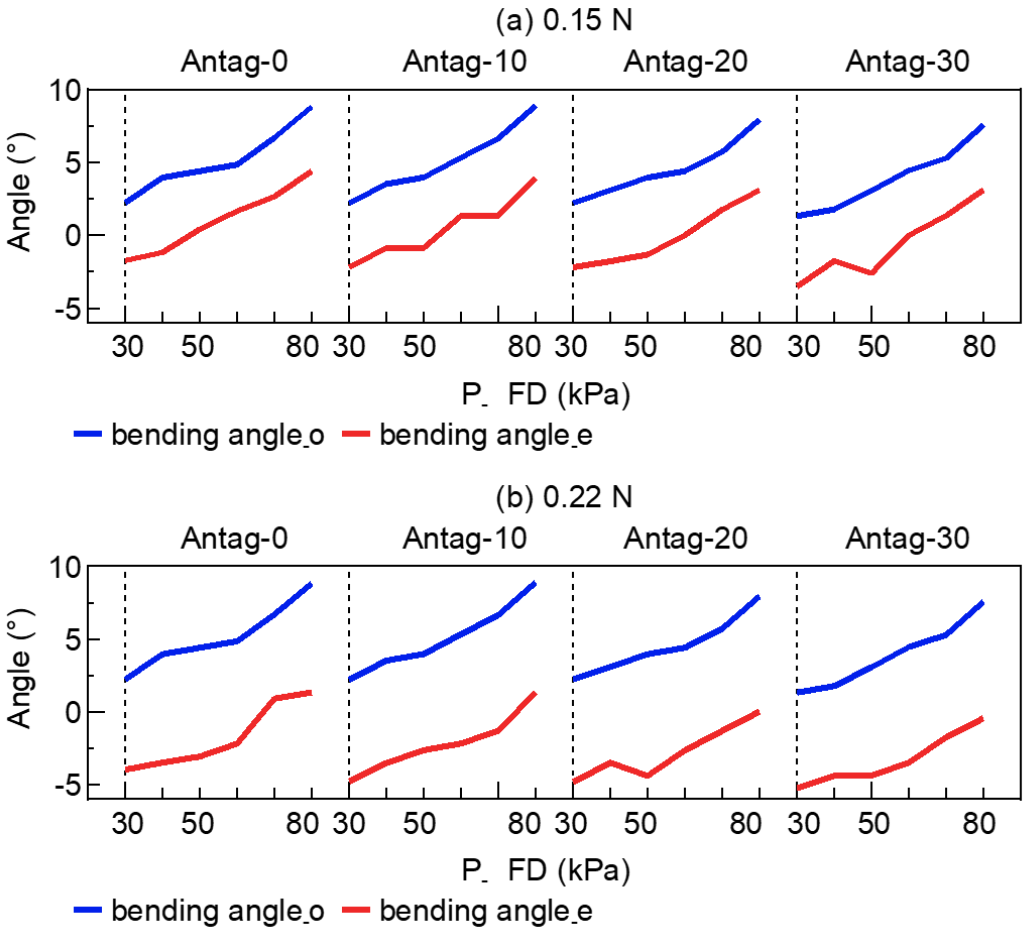

Figure 4.8 The bending angle_o and bending angle_e of soft actuator (a) 0.15 N, (b) 0.22 N.

Ideally, different sets of inputs (P_FD, P_FD, bending angle_o, bending angle_e) for the same external load should yield nearly identical instantaneous loads through a trained NN. Figure 4.8 displays bending angle_o and bending angle_e as network inputs.

When P_FU and P_FD are identical, the bending angles significantly influence the NN's output. As illustrated in Figure 4.8(b), during an early stage of 0.22N, Antag-20, a disturbance caused fluctuations in bending angle_e, leading to notable errors in the network output (instantaneous load). Following the exploration strategy, the synthesized estimation of the external load became smoother and more stable.

Figure 4.9 summarizes the success rate of estimations for each exploration strategy. The results indicate that relative to the instantaneous load, the success rate for each group improved after implementing an exploration strategy, though excessively long sequences introduced more error, while overly short sequences failed to sufficiently mitigate error impacts. Therefore, selecting an optimal exploration sequence length is critical. Given that the ±2, ±3, and +4 sequences achieved a success rate of 80% in estimating two different external loads, the optimal exploration sequence appears to be ±2.

To validate the effectiveness of the optimal exploration sequence (±2), the input data from this sequence was aggregated into a total input vector to train another multi-step estimation NN, meaning the input size for the multi-step estimation NN was (1,16). The single-step estimation NN's performance was comparable to the instantaneous load. Figure 4.10 compares the synthesized load (±2), single-step estimation NN, and multi-step estimation NN. The results confirm that data points from the multi-step estimation NN often deviated from the ground-truth value more frequently compared to the synthesized load (±2) and single-step estimation NN. For example, at 0.15N, the average and variance for the multi-step estimation NN (0.152 N, 0.0365) were higher than those for the single-step estimation NN (0.151 N, 0.0197) and synthesized load (±2) (0.150 N, 0.0195).

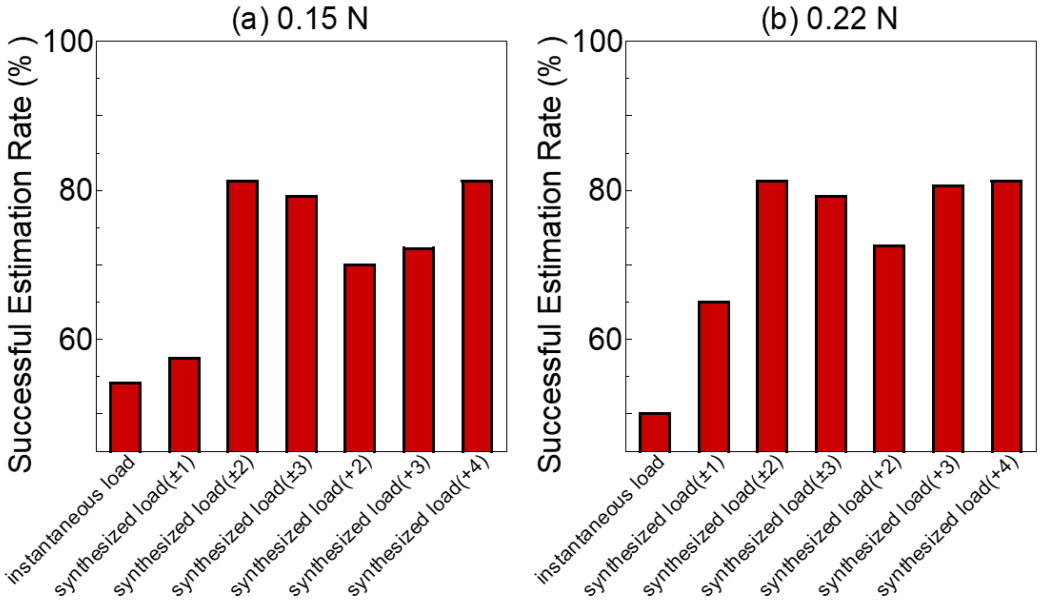

Figure 4.9 The successful estimation rate of load active sensing scheme with different sequence length (a) 0.15 N (b) 0.22 N.

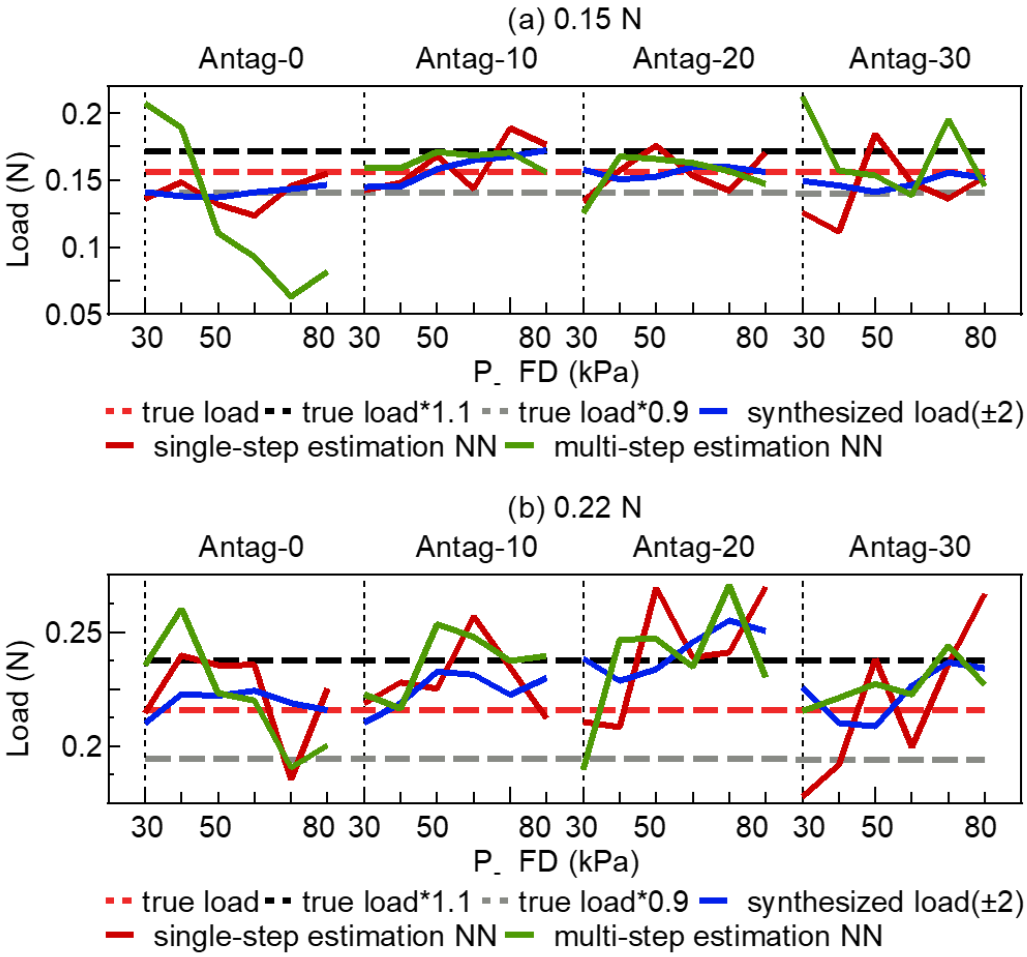

Figure 4.10 The test data of load active sensing scheme with 5.0 mm endoscope from NN at single-step estimation NN and multi-step estimation NN (a) 0.15 N, (b) 0.22 N.

Table 4.1 The mean and variance of different exploration sequences with true load 0.15 N.

P_FU		True load	Instantaneous Load	Synthesized Load (±1)	Synthesized Load (±2)	Synthesized Load (±3)	Synthesized Load (+2)	Synthesized Load (+3)	Synthesized Load (+4)
Antag-0	Mean (N)	0.156	0.140	0.141	0.141	0.141	0.143	0.144	0.144
	Variance (N^2)	3.413×10^{-5}	0.011	0.007	0.003	0.004	0.008	0.007	0.005
Antag-10	Mean (N)	0.156	0.161	0.159	0.159	0.159	0.166	0.167	0.168
	Variance (N^2)	8.078×10^{-6}	0.018	0.013	0.011	0.009	0.010	0.009	0.006

Antag-20	Mean (N)	0.156	0.156	0.155	0.156	0.155	0.158	0.157	0.156
	Variance (N^2)	1.479×10^{-5}	0.015	0.006	0.004	0.002	0.003	0.002	0.003
Antag-30	Mean (N)	0.156	0.143	0.145	0.148	0.149	0.149	0.151	0.150
	Variance (N^2)	1.742×10^{-5}	0.023	0.007	0.005	0.005	0.006	0.006	0.006
Total	Mean (N)	0.156	0.150	0.150	0.152	0.151	0.154	0.155	0.154
	Variance (N^2)	4.367×10^{-5}	0.020	0.009	0.008	0.009	0.010	0.011	0.010

Table 4.2 The mean and variance of different exploration sequences with true load 0.22 N.

P_FU		True load	Instantaneous Load	Synthesized Load (±1)	Synthesized Load (±2)	Synthesized Load (±3)	Synthesized Load (+2)	Synthesized Load (+3)	Synthesized Load (+4)
Antag-0	Mean (N)	0.216	0.223	0.221	0.219	0.218	0.221	0.220	0.219
	Variance (N^2)	4.357×10^{-5}	0.019	0.010	0.005	0.004	0.010	0.007	0.004
Antag-10	Mean (N)	0.216	0.229	0.225	0.224	0.223	0.227	0.228	0.228
	Variance (N^2)	1.029×10^{-5}	0.014	0.013	0.008	0.005	0.010	0.006	0.004
Antag-20	Mean (N)	0.216	0.240	0.239	0.242	0.241	0.247	0.247	0.246
	Variance (N^2)	1.479×10^{-5}	0.025	0.015	0.009	0.006	0.010	0.008	0.007
Antag-30	Mean (N)	0.216	0.218	0.221	0.224	0.226	0.228	0.230	0.230
	Variance (N^2)	1.742×10^{-5}	0.031	0.017	0.011	0.006	0.017	0.016	0.012
Total	Mean (N)	0.216	0.228	0.226	0.225	0.227	0.231	0.231	0.231
	Variance (N^2)	1.134×10^{-5}	0.025	0.016	0.012	0.013	0.017	0.014	0.013

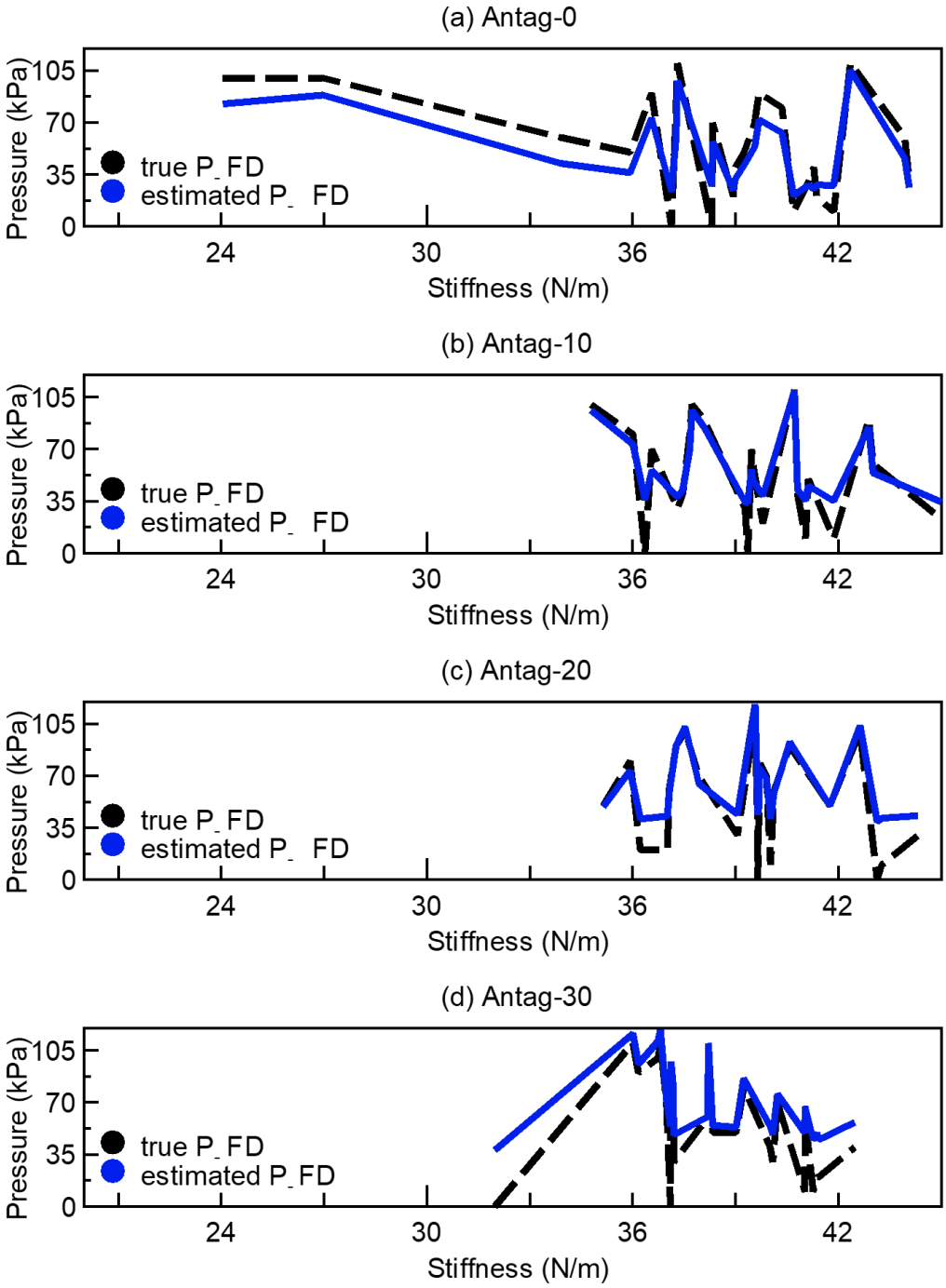

Figure 4.11 The test data of adjusting stiffness with 5.0 mm endoscope from NN (a) Antag-0, (b) Antag-10, (c) Antag-20, (d) Antag-30.

4.4.4 The results of NN-based inverse dynamics model for stiffness

The results from the NN-based inverse dynamics model for stiffness adjustment, which calculates the necessary P_FD based on a specified desired stiffness, are presented in Figure 4.11. Although the relationship between stiffness and air pressure is nonlinear, the

model successfully adjusted the air pressure values to meet the desired stiffness levels. However, the model struggled to predict air pressure accurately when the actual P_FD was below 35 kPa.

4.5. Discussion

Experiments on DoF 1, comprising the FU and FD chambers, were conducted to explore how varying inflation conditions affect the soft actuator's stiffness and bending angle_o. As depicted in Figure 4.4, P_FU and P_FD exert opposite effects on bending angle_o. The P_FU chamber typically inhibits bending, while the P_FD chamber enhances it. This is because asymmetric deformation of the chambers on either side primarily drives the bending of the soft actuator [11], with larger asymmetries resulting in more pronounced bending. Increased P_FD leads to greater symmetric deformation of the actuator in response to the expansion of FD, while expansion of FU reduces the asymmetric deformation, significantly inhibiting bending angle_o.

This inhibitory effect, however, diminishes when P_FD is increased beyond 90 kPa, as shown in Figure 4.4 (a). The strain-limiting cotton fibers on the actuator's exterior, which constrain the deformation of the air chamber outward, allow the chamber to expand only inward toward the hollow structure of the actuator. Consequently, an expanding FD may eventually conflict with the expansion of FU internally, thus enhancing asymmetric deformation and bending angle_o.

Moreover, the stiffness of an endoscope can vary with its bending angle; notably, stiffness increases significantly at larger bending angles. This variability also applies to the soft actuator, as demonstrated in Figure 4.6 (a), where total stiffness (endoscope plus soft actuator) changes with different bending angles (Figure 4.6). Figure 5 indicates that P_FU impacts the pneumatic actuator's stiffness. Furthermore, expansion due to air pressure may cause the endoscope and FU to compress against each other, leading to unstable contact and friction forces that inhibit bending and affect bending angle_o.

High P_FD levels (over 90 kPa) significantly increase the stiffness of the soft actuator due to the silicon material of the air chamber being extensively stretched, rendering it virtually undeformable under external load [50]. In Figures 4.5 (c) and (d), Antag-0-e5.4mm exhibited lower stiffness compared to Antag-0-e5.0mm, attributable to the lower stiffness of the 5.4 mm endoscope compared to the 5.0 mm endoscope as mentioned in Section 2.1. Although a larger diameter endoscope should theoretically be more easily bent by the soft actuator, it can more substantially impede chamber expansion, reducing bending angle_o. Hence, in Figures 4.4(c) and (d), the bending angle_o of Antag-0-e5.0mm was not greater than that of Antag-0-e5.4mm.

To enhance the precision of external load estimation using the load active-sensing system, an environmental exploration strategy was introduced and implemented in the prototype experiment. Figures 4.7 and 4.9 show that this strategy substantially improved the accuracy of external load estimations and the success rate of estimations. When the exploration strategy was not utilized, and input perturbations such as bending angle_e occurred, the NN's output quality deteriorated, as seen in Figure 4.8. Exploration averaged

out inaccuracies, as shown in Figure 4.7 for Antag-30 with 50 kPa under 0.15 N and Antag-0 with 70 kPa under 0.22 N, employing a moving average concept to smooth the output.

Tables 4.1 and 4.2 indicate that the mean value of the synthesized external load estimation generally increased with longer sequence lengths, while variance decreased. For example, +4 had a higher mean error and a lower variance error than +2, while ±1 and ±3 were similar. This suggests that longer sequences reduce variance in estimation but may increase the risk of errors. Verification showed that the mean value of the load estimation performed well, with the highest success rates for sequences of ±2 and +4, except for the Antag-20 under 0.22 N group. Although ±2 and +4 had the same sequence length, ±2 involved inflating two steps forward and deflating two steps backward, with the maximum air pressure after exploration being 20 kPa higher/lower than the original. In contrast, +4 involved only forward inflation, ending 40 kPa higher than the initial pressure. Figure 4.4 showed that the change in angle increased with rising air pressure, indicating that the change in angle for the ±2 sequence was less than that for the +4 sequence, resulting in shorter exploration times and greater efficiency. Moreover, Figure 4.2 showed that the bending angle_o of Antag-20-e5.0mm changed very little at 30-80 kPa of P_FD, explaining why the Antag-20 under 0.22 N group could not achieve a successful estimate. This suggests that when the difference between two bending angles is minimal, the network's load estimations are adversely affected. At the same time, the optimal exploration sequence (±2) had still not generalizability, and thus this optimal exploration sequence was based on our experiment result of our soft actuator and could not be presumed.

Conversely, multi-step estimation NN, trained with all data from the optimal exploration sequence, did not enhance the effectiveness of instantaneous load estimations and introduced larger errors, as shown in Figure 4.10. This could be attributed to the increased perturbations introduced by expanded input data. Hence, using the optimal exploration sequence (±2) as input for NN may not be advisable.

The NN-based inverse dynamics model effectively estimates appropriate P_FD for desired stiffness above 35 kPa. However, below this threshold, the model’s performance declines, possibly due to minimal variation in actuator stiffness at lower pressures, which hampers accurate P_FD estimation.

The contribution of our study:

1. In related research [47], it was observed that NNs often generate highly deviated predictions for real test samples. In our work, we introduced a load active-sensing scheme and an environment exploration strategy to refine the instantaneous load predictions from the NN. Furthermore, we investigated the optimal exploration sequence, which reduced the estimation error to less than 0.01N and increased the successful estimation rate to 80%. Our proposed method not only aids surgeons in selecting the appropriate stiffness of the soft actuator based on accurate external load assessment but also provides engineers with crucial data for designing more effective feedback controllers.

Additionally, we developed an inverse dynamics model for stiffness adjustment, which assists surgeons in easily modifying the actuator's stiffness to counter varying external loads during MIS procedures, thus maintaining a stable surgical view. This model holds potential for future in-depth studies on soft actuators’ stiffness or impedance control.

4.6. Conclusion and future work

In this chapter, we presented a NN-based load active-sensing scheme and a stiffness adjustment mechanism for a soft actuator, aimed at ensuring a stable surgical view during MIS. To accurately estimate external load and thereby determine suitable stiffness for the soft actuator, we enhanced the estimation accuracy using an environment exploration strategy.

Our findings demonstrated that this strategy significantly improved the accuracy and success rate of external load estimations compared to direct NN outputs. The synthesized load (±2) was identified as the optimal exploration sequence, offering the highest successful estimation rate, a minimal exploration range, and reduced exploration time. We also introduced and implemented an inverse dynamics model for stiffness adjustment, which effectively calculates the necessary air pressure P_FD to achieve the desired stiffness for the soft actuator.

Future research will focus on expanding the load active-sensing scheme to encompass multiple degrees of freedom (multi-DoFs) in soft actuators and developing a closed-loop feedback controller that can adjust for desired angles and stiffness.

5. Master–Slave Operational Framework

5.1. Preface

Chapter 5 of this thesis validates the practical relevance of our research by introducing a preliminary master-slave framework and detailing the experimental setup. In addition to the initial surgical simulations that underscore the potential of our actuator in enhancing surgical precision and safety in transvesical prostatectomy, we conducted evaluations within a porcine bladder model. By simulating the circumferential resection of the bladder wall, we assessed the effects of stiffness modulation and the operational functionality of the Master-Slave Operational Framework. These experiments not only demonstrate the actuator's capacity in a controlled environment but also provide a deeper understanding of its performance in more realistic surgical scenarios. Collectively, these investigations deliver valuable insights that contribute to improving the design and performance of actuators in complex minimally invasive surgeries (MIS). This chapter serves as a critical bridge between theoretical research and practical application, underscoring the effectiveness of our proposed solutions in real-world surgical environments.

5.2. Setup of Master–Slave Operational Framework

To demonstrate the capabilities of our 3-DoF pneumatic soft actuator, whose design aligns with that described in Chapter 3 (see Figure 3.1(a)), we utilized a master-slave operational framework showcased in Figure 5.1(a). This setup integrates a user-centric handle that directs the motions of a coupled robotic arm (myCobot 320-M5, Elephant Robotics Co., Ltd., CN) and the soft actuator, essential for precise navigations within critical surgical zones. Embedded within the actuator, an endoscope (Ambu® aScopeTM 4 Broncho Slim, diameter: 3.8 mm) equipped with a laser-cutting device (SLIMLINE 365 MKTG S/N:1, Lumenis GmbH, DE) provides real-time visual feedback, guiding surgical interventions as depicted in Figure 5.1(a).

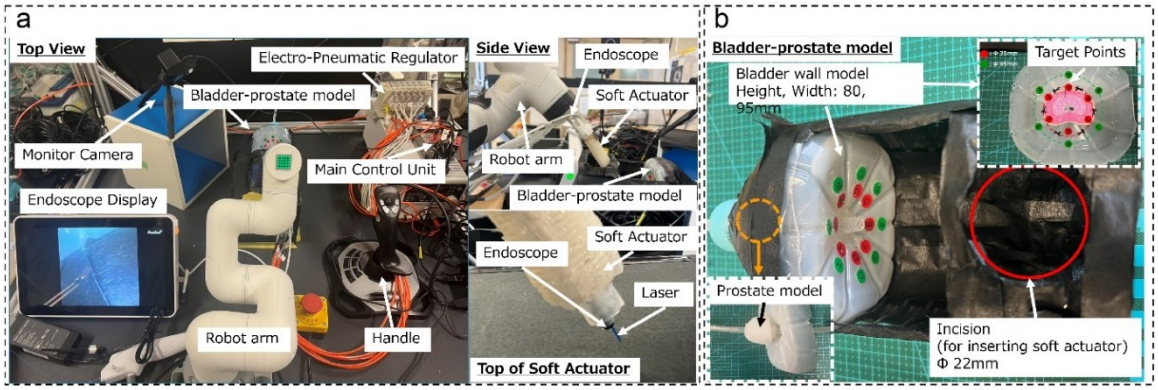

Figure 5.1 (a) Master–Slave Operational Framework (b) Prototype Bladder–Prostate Model

The master-slave control system's block diagram, depicted in Figure 5.2(a), showcases the detailed mechanism through which the surgeon, serving as the primary

operator, dynamically controls the soft actuator in x, y, and z axes based on real-time visual feedback provided by the endoscope embedded within the actuator. This system effectively integrates and transforms various control and feedback mechanisms to manage the soft actuator's precise movements within a surgical setting.

Control Signal 1, modulated by the operator's manipulation of the handle, varies from 0 to 2000, corresponding to output voltages between 0-2V from an air regulator. These voltages directly influence the air pressure within the actuator's chambers, facilitating precise deformations in the y and z axes. Figure 5.2(b) details the correlation between the control signal magnitude and the resultant air pressures, ensuring that operational inputs translate into accurate mechanical responses.

Control Signal 2, managed through an encoder, is transmitted directly to the robotic arm. It controls the arm's steady movement at a controlled speed of 1mm/s along the x-axis. This consistency is vital for maintaining the actuator's alignment with the surgical target, ensuring precise positioning within the designated surgical zones.

The integration of the robotic arm and the soft actuator involves a sophisticated coordinate transformation where joint coordinates are translated to world coordinates in the surgical field through a Denavit-Hartenberg (DH) transformation. This aligns the actuator's base with the robot arm's endpoint, providing a seamless control experience for the surgeon. The real-time visual feedback from the endoscope allows the surgeon to make immediate adjustments, influencing Control Signals 1 and 2 to fine-tune the actuator's orientation and position in response to the surgical environment's dynamic requirements.

Feedback mechanisms within the system include:

1. Visual Feedback from the Endoscope: Essential for the surgeon to observe the actuator's position relative to the surgical target and adjust control inputs accordingly.
2. Encoder Feedback from the Robotic Arm: Ensures precise x-axis movement control.
3. Internal Feedback from the Actuator: Monitors changes in air pressure within the actuator, providing essential data back to the control system for further adjustments.

This master-slave control framework exemplifies the critical integration of feedback and control necessary for precise surgical manipulations. By continuously monitoring and adjusting based on real-time data, the system ensures that the actuator performs accurately under varying surgical conditions, enhancing the overall reliability and effectiveness of surgical interventions.

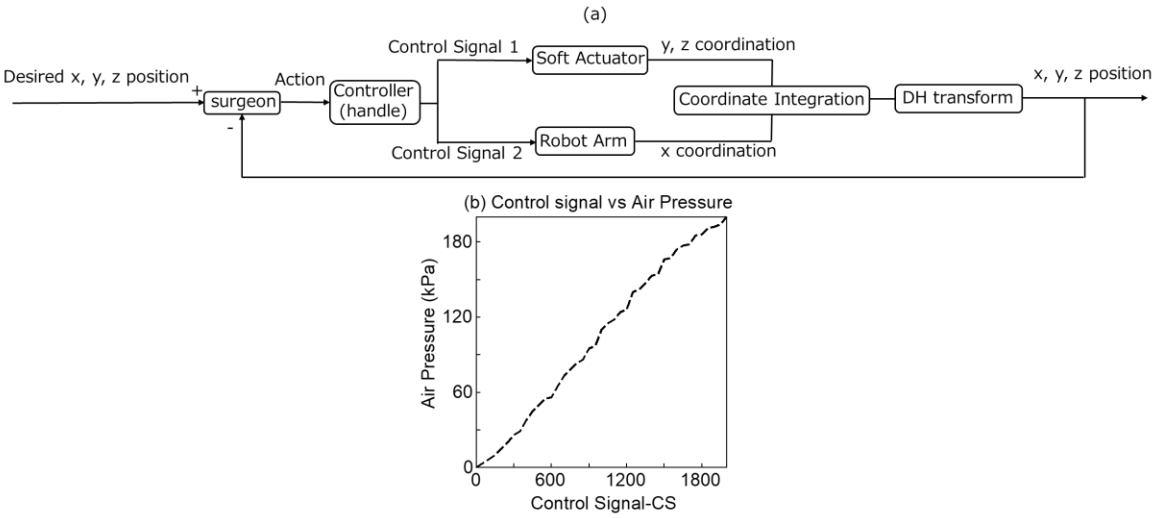

Figure 5.2 (a) Block Diagram of the Master-Slave Control System for Soft Actuator Manipulation (b) Relationship Between Control Signal 1 and Resultant Air Pressure in the Soft Actuator

To critically assess the master-slave framework's operational characteristics, the operator performed rapid oscillations of the handle to maximize the actuator's movement speed in the y-direction. During these dynamic tests, we continuously monitored variations in the control signal, air pressure, and y deformation. This analysis was pivotal for evaluating the actuator's responsiveness and the system's stability under conditions mimicking those in surgical settings. It was particularly informative for understanding the time lag between manual inputs at the handle and the actuator's corresponding responses.

These experiments are crucial for refining the design and control algorithms of the system, enhancing its accuracy and reliability for clinical applications. By examining the direct impact of control adjustments on actuator behavior, this phase aids in optimizing the system for better performance in real-world surgical scenarios, ensuring that surgeons can rely on the actuator for precise and controlled surgical maneuvers.

5.3. Experiment Setup with a Bladder–Prostate Model

The primary goal of ·bladder–prostate model experiment was to assess the functionality of the soft actuator in two key areas: its ability to accurately navigate to pre-defined target points within a bladder model and its precision in positioning a laser at these points to simulate surgical incisions, mirroring critical steps in single-port transvesical prostatectomy procedures [51]. These target points, labeled A–H in Figure 5.1(b), were chosen to evaluate the precision and accuracy of the system in a simulated surgical environment.

We used silicone-fabricated models (Dragonskin 10 MEDIUM, Smooth-On, Inc., US) to simulate the textural properties of the prostate and bladder. Although these models approximate the softness of these tissues, they cannot perfectly replicate their textural properties due to inherent material differences. The soft actuator accessed the bladder

model through a designated circular opening, simulating an entry incision (Figure 5.1(b)) for surgical instruments in a single-port MIS procedure.

In the prototype experiments conducted using the bladder–prostate model, four participants were selected from a pool of medical engineering students without prior experience in soft robotic systems or robotics. This selection criterion ensured an unbiased assessment of the master–slave operational framework. Before the experiment, the participants received a structured training session consisting of a 10-min instructional segment on the experiment and system operation, followed by a 3-min hands-on use period. During the hands-on session, participants practiced tasks that mirrored the actual experimental procedure, such as navigating the actuator through a simulated environment and positioning the laser at designated target points.

5.4. Setup of Experiments with a Porcine Bladder Model

To evaluate the practical effects of stiffness modulation of the 3-DoF pneumatic soft actuator (as designed in Chapter 3, see Figure 3.1(a)) on MIS, we conducted experiments with a porcine bladder model. These experiments were designed to simulate the circumferential resection of the bladder wall to assess the actuator's functionality under real surgical conditions.

- Setup

The experiment was performed under the supervision of an experienced urological surgeon, with extensive experience in prostatectomy, operated the master-slave operational framework (as described in Chapter 5.2, see Figure 5.1(a)).

A mature male porcine bladder was secured in a fixed position, and an incision of one inch in diameter was made on the top of the bladder to simulate a surgical entry point. The soft actuator, equipped with an endoscope (Ambu® aScope™ 4 Broncho Slim, diameter: 3.8 mm) and a laser-cutting device (SLIMLINE 365 MKTG S/N:1, Lumenis GmbH, DE), was inserted through this incision. The primary objective was to navigate the actuator along elliptical trajectories around the urethral opening as depicted in Figure 5.3(c), providing real-time visual feedback via the endoscope.

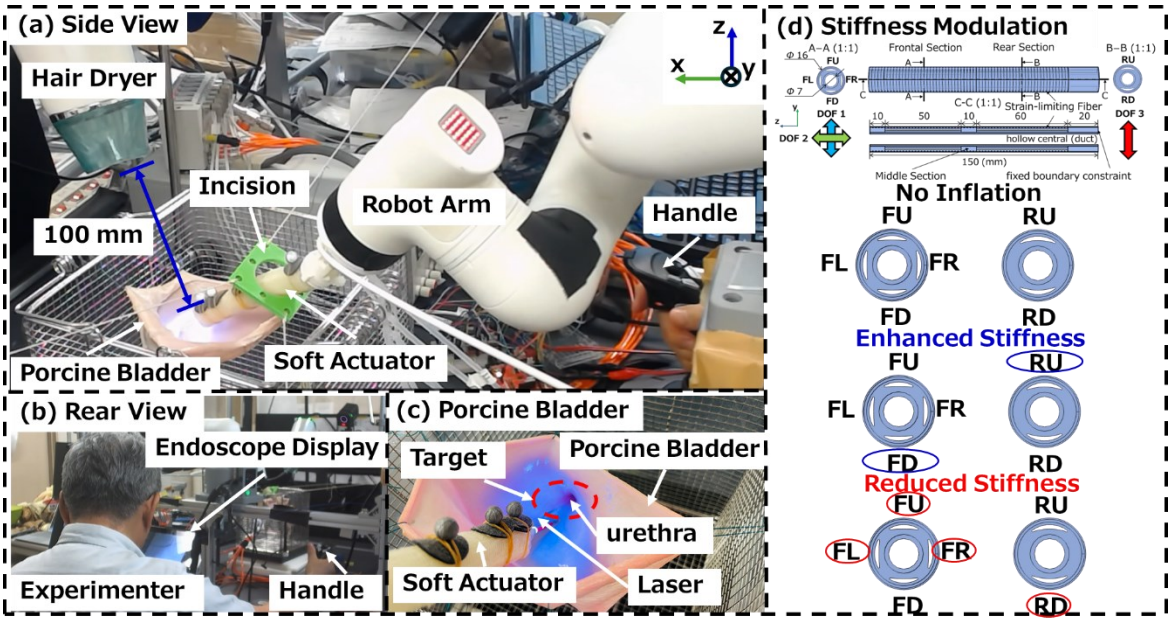

Figure 5.3 Experimental Setup and Trajectory Analysis of the 3-DoF Pneumatic Soft Actuator with a Porcine Bladder Model (a) Setup of the porcine bladder with an incision for actuator insertion (b) Close-up view of the soft actuator navigating the elliptical trajectory around the urethral opening (c) Detailed illustration of the actuator's path along specified points on the elliptical trajectory (d) Diagram showing different stiffness configurations of the actuator with specific chamber inflations at 30kPa

- Simulation of External Disturbances

To simulate external disturbances encountered during surgical procedures, we employed a hair dryer (3 Ion Jet Hair Dryer, 1500 W, Yamada Denki Co., LTD., JP) positioned 100 mm from the actuator. This approach was chosen to represent the unexpected dynamic pressures that can arise from various sources such as irrigation flows, inflation of surgical devices, or external tissue compression during MIS. These dynamic pressures are analogous to air currents, and their effects on surgical instruments can critically influence the precision and operational stability of the instruments.

Using a hair dryer to create controlled airflow allows us to quantitatively mimic these dynamic disturbances in a reproducible way. This method aligns with strategies commonly used in industrial and medical device testing to simulate and measure the resilience of instruments against external physical forces.

For academic support of such simulation methods, while not directly analogous, the previous study [57] discusses the impact of operational environment factors on robotic instrument performance. Although this reference does not specifically address using hair dryers, it underlines the importance of considering external physical disturbances in the design and testing of surgical devices, thereby providing a conceptual backing for our simulation approach.

- Data Collection and Analysis

Motion capture markers were placed on the top of the soft actuator to track its movements in the x-, y-, and z-directions using the NOKOV motion-capture system. An external monitor camera (C390e, WEB camera, Logicool Co. Ltd., JP) was also used to observe the actuator's external movements.

- Stiffness Configurations

The experiments were conducted across different stiffness configurations—no-inflation, enhanced stiffness, and reduced stiffness. These configurations were based on inflating specific chambers to 30kPa as determined in Chapter 3. Each configuration's specific inflation setup is illustrated in Figure 5.3(d).

- Objective

The primary goal of this experiment was to evaluate the trajectory stability and execution accuracy of the soft actuator under various stiffness settings, as manipulated by the experimenter. This evaluation aimed to assess both the stability and completeness of the actuator's performance in replicating precise surgical maneuvers within the porcine bladder model.

5.5. Results and Discussion

- Results of Master–Slave Operational Framework

The experimental results provided significant insights into the dynamic behavior of the soft actuator. As depicted in Figure 5.4(a), the actuator's air pressure response closely aligned with the control signal during rapid movements in the y-direction, showcasing minimal delay. This prompt responsiveness indicates a highly efficient pneumatic system capable of quick adjustments, essential for precise surgical manipulations.

In Figures 5.4(b) and 5.4(c), a noticeable delay was observed between y deformation and the corresponding control signal and air pressure, especially at the beginning of operations with initial delays of approximately 2.5 seconds. These delays diminished progressively with continued operation. This initial lag is likely due to the actuator's internal dynamics, where initially no air is present, and it takes time for the air to fill the actuator and induce deformation. The initial resistance may also be attributed to the properties of the silicone material used in the actuator, which might exhibit initial stiffness until adequately pressurized. As noted in Chapter 3, pre-charging the actuator with a baseline air pressure of 30 kPa significantly enhances its responsiveness—a method akin to pretension in mechanical systems. This pretension effect is planned to be integrated into the operational protocol to ensure improved initial responsiveness.

Moreover, Figure 5.3(d) illustrates the delays in the inflation and deflation cycles, measuring the time taken to reach 50% of the maximum values for control signal, air pressure, and y deformation. Analysis based on these delay times indicates that the differences in response times for control signals, air pressure adjustments, and actual

deformations are exceptionally minimal, within 0.2 seconds, demonstrating an exceptionally synchronized control loop.

These findings highlight the actuator's potential for refined control in surgical settings, particularly when rapid and precise maneuvers are required. The minimal delays in response times across control signals, air pressure adjustments, and actual deformations ensure that the actuator can perform complex tasks with high fidelity, closely following the surgeon's inputs. Future work will aim to further optimize these control mechanisms, introducing strategies such as the forementioned pretension setting to enhance the actuator's operational efficiency and reliability in clinical environments.

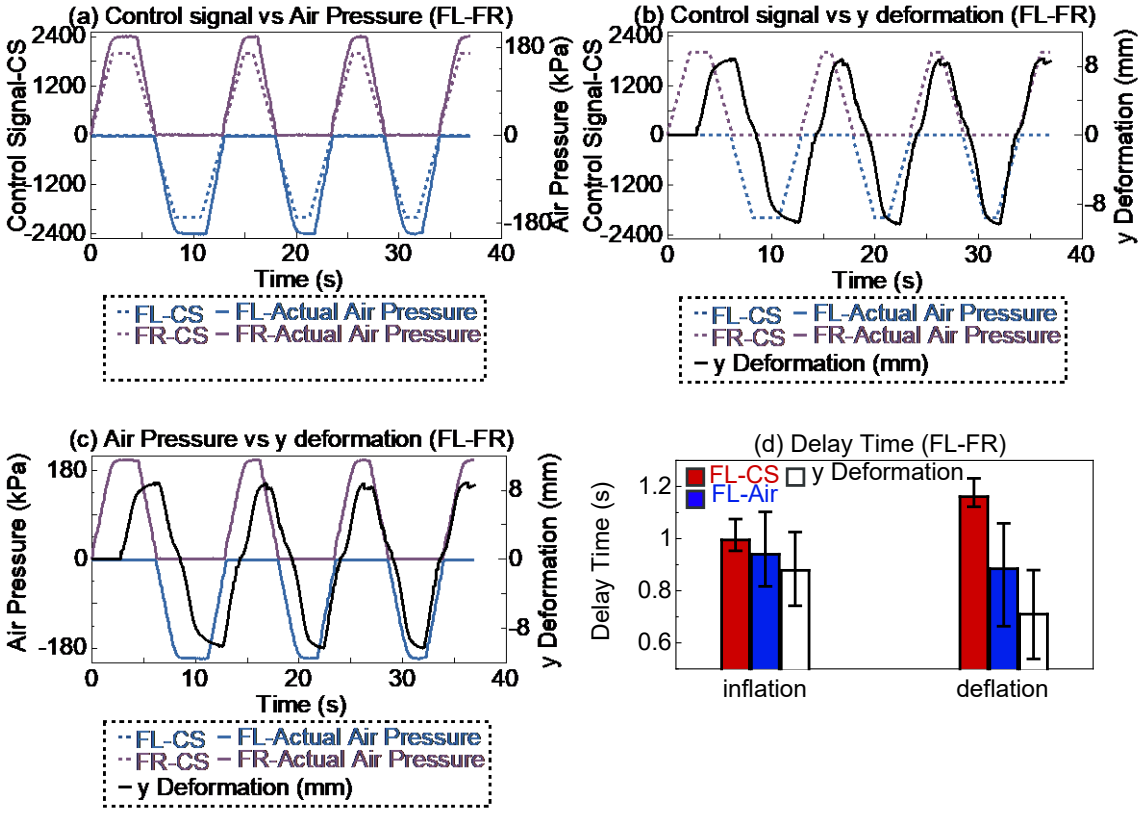

Figure 5.4 Response Dynamics of the Actuator in the Master-Slave Framework (a) Control Signal and Air Pressure Response (b) Delay in Y Deformation at Initial Activation (c) Reduction in Y Deformation Delay Over Repeated Operations (d) Delay Time Analysis during Inflation and Deflation

- Prototype Experiments with a Bladder–Prostate Model

In the prototype experiments conducted with the bladder–prostate model, inadvertent contact with the model occurred when the participants operated the handle to introduce the soft actuator. The designated entry point for the soft actuator proved challenging, with frequent instances of squeezing and friction between the actuator and the model.

Despite these challenge, all participants demonstrated significant precision in guiding the soft actuator to pre-defined target points (labeled A–H). Each participant

accurately located and engaged at these points. This precision is shown in Figure 5.5, which provides endoscopic views illustrating accurate engagement with the target points.

To complement the observed precision in actuator guidance, we quantitatively assessed the performance of the master-slave framework by measuring the extension distances from the end of the endoscope to each predefined target point (labeled A–H). This measurement was crucial to ascertain whether the endoscope could consistently reach the same target areas across multiple trials, thereby verifying the operational accuracy of the master-slave framework.

As depicted in Figure 5.5, due to the inherent angle at which the soft actuator was inserted into the model, the extension distances to each target point varied. However, the variability in extension distances across multiple experiments remained minimal, with error bars within a 1mm range. This consistency in reaching target points despite the varied extension distances illustrates the precision and reliability of the master-slave system under operational conditions. Additionally, the operational time to reach each target varied with the distance to the targets as shown in Figure 5.6. Despite these differences, the consistency of the operational times for the same targets across multiple trials was remarkably high, with time variations within a 3-second range. This further underscores the system's ability to maintain performance consistency even with varying target distances.

The significance of these findings lies in their demonstration that the master-slave framework can reliably control the soft actuator to achieve precise positioning within a complex environment. This ability is critical in surgical applications where precise maneuvering of tools to specific anatomical sites is necessary under varying operational angles and insertion depths. The consistent performance across trials and the minimal variation in operational times suggest that the system can be effectively used in clinical settings, ensuring that surgical instruments maintain their target engagement accuracy, which is paramount for successful surgical outcomes.

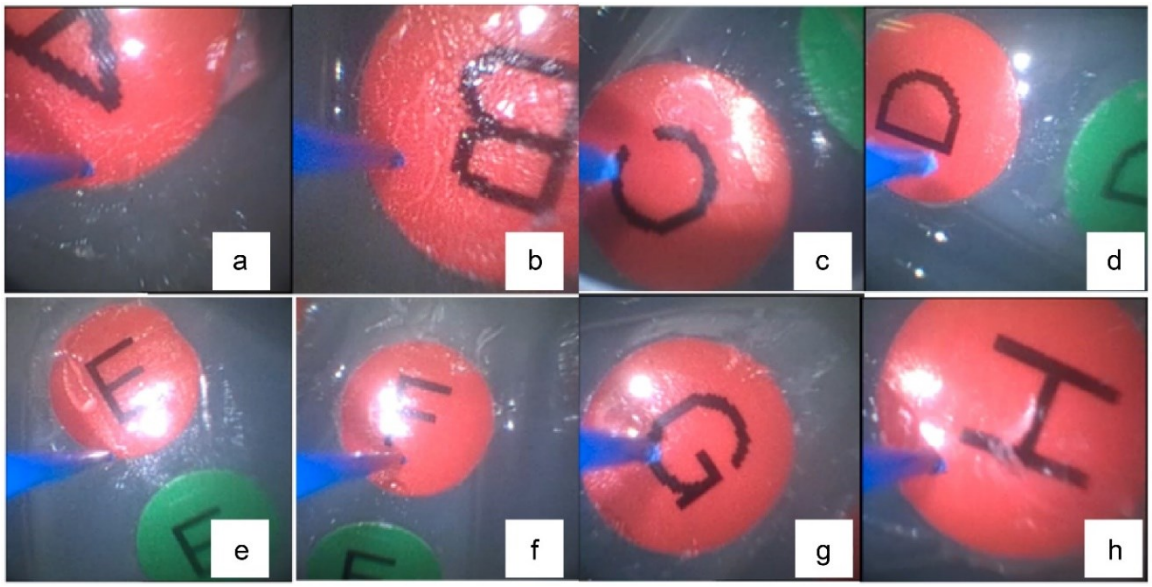

Figure 5.5 Endoscopic Views Demonstrating Accurate Engagement with Pre-Defined Target Points (a–h) by Participants in the Simulated Surgical Setting

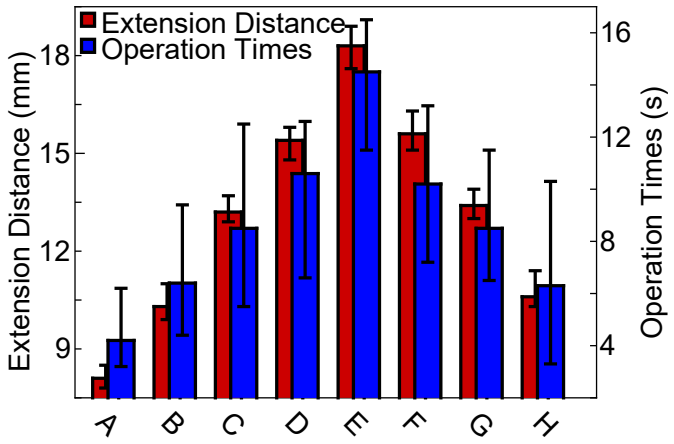

Figure 5.6 Extension Distances and Operation Times from Endoscope to Target Points A-H with Error Bars Showing Variability Across Multiple Trials

The prototype experiments with the bladder–prostate model offered valuable insights into the functionality of the master–slave operational framework in a simulated surgical setting. A key challenge was the recurring friction between the actuator and the model at the specified entry point. The difficulties may stem from the soft actuator's tip dimensions, flexibility, or constraints at the insertion site. Such unintentional interactions in a real-world setting could result in tissue damage or procedural complications. Addressing this issue may require adjustments to the actuator design or insertion technique.

In contrast, the ease and precision with which all participants guided the soft actuator to pre-defined target points underscore the high degree of control and dexterity of the system once inserted. This observed precision suggests that the master–slave operational framework holds great promise for ensuring precision targeting within surgical settings, which is vital for the safety and success of MIS. Additionally, the minimal unintended contacts between the actuator and the bladder–prostate model during the exploration phase validate the inherent stability and predictability of the system post-insertion.

- Prototype Experiments with a Porcine Bladder

In our prototype experiments conducted within a porcine bladder, we assessed the effectiveness of a 3-DoF pneumatic soft actuator integrated with a master-slave operational framework during simulated single-port transvesical prostatectomy. These tests specifically focused on the actuator's ability to navigate elliptical trajectories around the urethral opening. Under all tested stiffness configurations, the operator successfully touched multiple points along the trajectory as illustrated in Figure 5.7 (a-g), demonstrating the actuator's capability to perform the critical step of circumferential bladder wall resection to expose the prostate. This underscores its potential application in single-port transvesical prostatectomies.

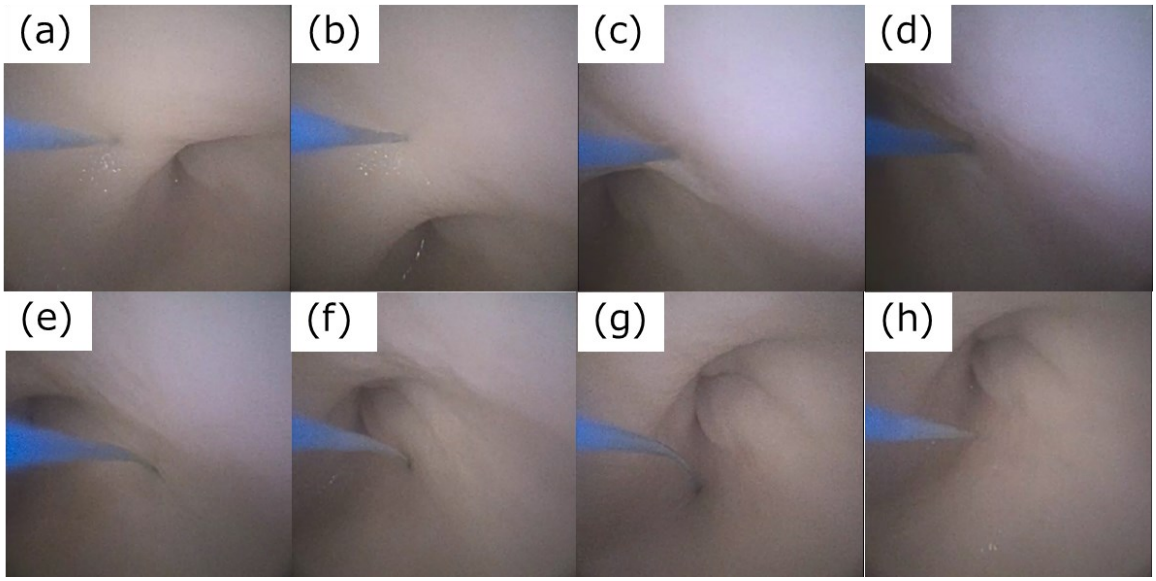

Figure 5.7 Actuator Navigation on Elliptical Trajectory in the Porcine Bladder Model

The actuator was evaluated under different stiffness settings, revealing notable variations in operation time, stability, and task execution completeness. In the enhanced stiffness configuration, the actuator achieved the shortest operational time, averaging approximately 2.00 minutes (mean: 2.01 min, standard deviation: 0.05 min). Motion capture data showed that the actuator's trajectory closely followed the planned elliptical path, effectively resisting external disturbances caused by a hair dryer, which minimized instability or jitter (refer to Figure 5.8(b)).

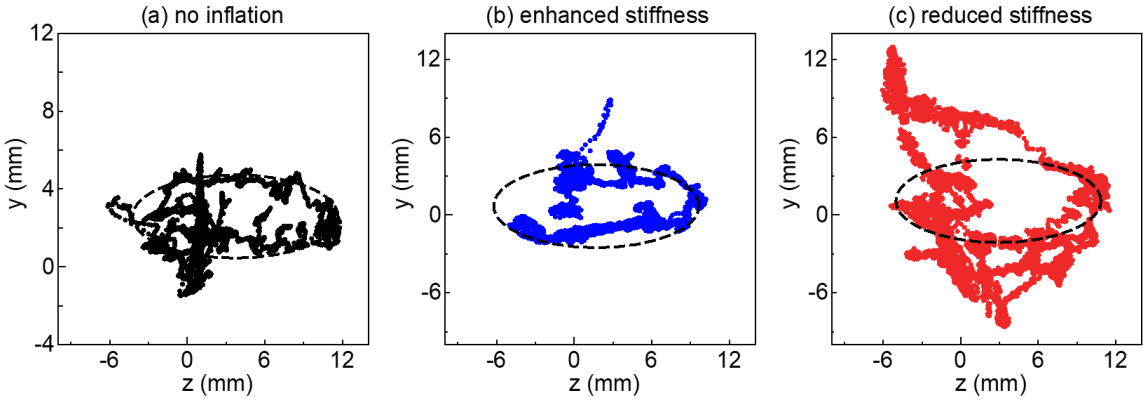

Figure 5.8 Effect of Stiffness Configurations on Actuator Trajectory Stability (a) no inflation (b) enhanced stiffness (c) reduced stiffness

Conversely, in the no inflation configuration, operational time increased to approximately 2.15 minutes (mean: 2.15 min, standard deviation: 0.08 min). Despite generally adhering to the intended path, noticeable jitters were observed (refer to Figure 5.7(a)), requiring frequent manual adjustments by the operator to correct positioning. The most prolonged operational time occurred in the reduced stiffness configuration, which took up to 3.20 minutes (mean: 3.20 min, standard deviation: 0.30 min). In this setup, the

actuator often deviated from the elliptical trajectory, displaying significant deviations and instability due to reduced rigidity, which heightened the impact of external noise on its movement (refer to Figure 5.8(c)).

These observations highlight the critical role that stiffness configuration plays in the functionality of soft actuators within surgical environments. The enhanced stiffness configuration was particularly effective in maintaining trajectory precision and operational speed, suggesting that higher rigidity can better counteract external disturbances common in surgical settings. However, the reduced stiffness configuration, although potentially offering greater flexibility, negatively impacted operation precision and speed due to increased sensitivity to external disturbances.

In elucidating the dynamic operational characteristics of the Master-Slave Operational Framework under various stiffness configurations, our extensive data collection revealed the profound impact of stiffness settings on the actuator's performance metrics. Each configuration, namely no inflation, enhanced, and reduced stiffness, showcased distinct behavioral patterns regarding deformation responsiveness in both the y and x directions as regulated by specific chamber controls: FU and U chambers for negative y-direction, FD and D for positive y-direction, FL for x-direction, and FR for negative x-direction. The operational dynamics under these conditions were thoroughly recorded, analyzing the relationship between time, control signal, air pressure, and resultant deformations, as detailed in Figures 5.9-5.11. These observations highlighted a stark variance in the actuator's performance across different stiffness configuration.

In the no inflation configuration, when both the control signal and air pressure exceeded 600 and 60 kPa respectively, the actuator's y and x deformations adjusted rapidly, showing minimal delay—less than 0.5 seconds (mean: 0.5s, standard deviation: 0.1s). This responsiveness is effectively demonstrated in Figure 5.9(a)-(d), illustrating excellent operational performance. However, when decreasing the control signal and air pressure, delays in y and x deformations increased significantly, reaching up to 2.0 seconds (mean: 2.0s, standard deviation:0.3s). The lag primarily occurred because the electronic proportional valves did not promptly reduce air pressure after a decrease in control signals, resulting in prolonged response times as shown in Figure 5.9(e). At lower control signals and air pressures (greater than 60 kPa), the actuator was heavily influenced by external disturbances (simulated by a hair dryer), which caused significant instability, observable as severe shaking. This instability compromised the actuator’s ability to consistently follow the changes in control signals, leading to poor consistency in the relationship between y and x deformations and control signals.

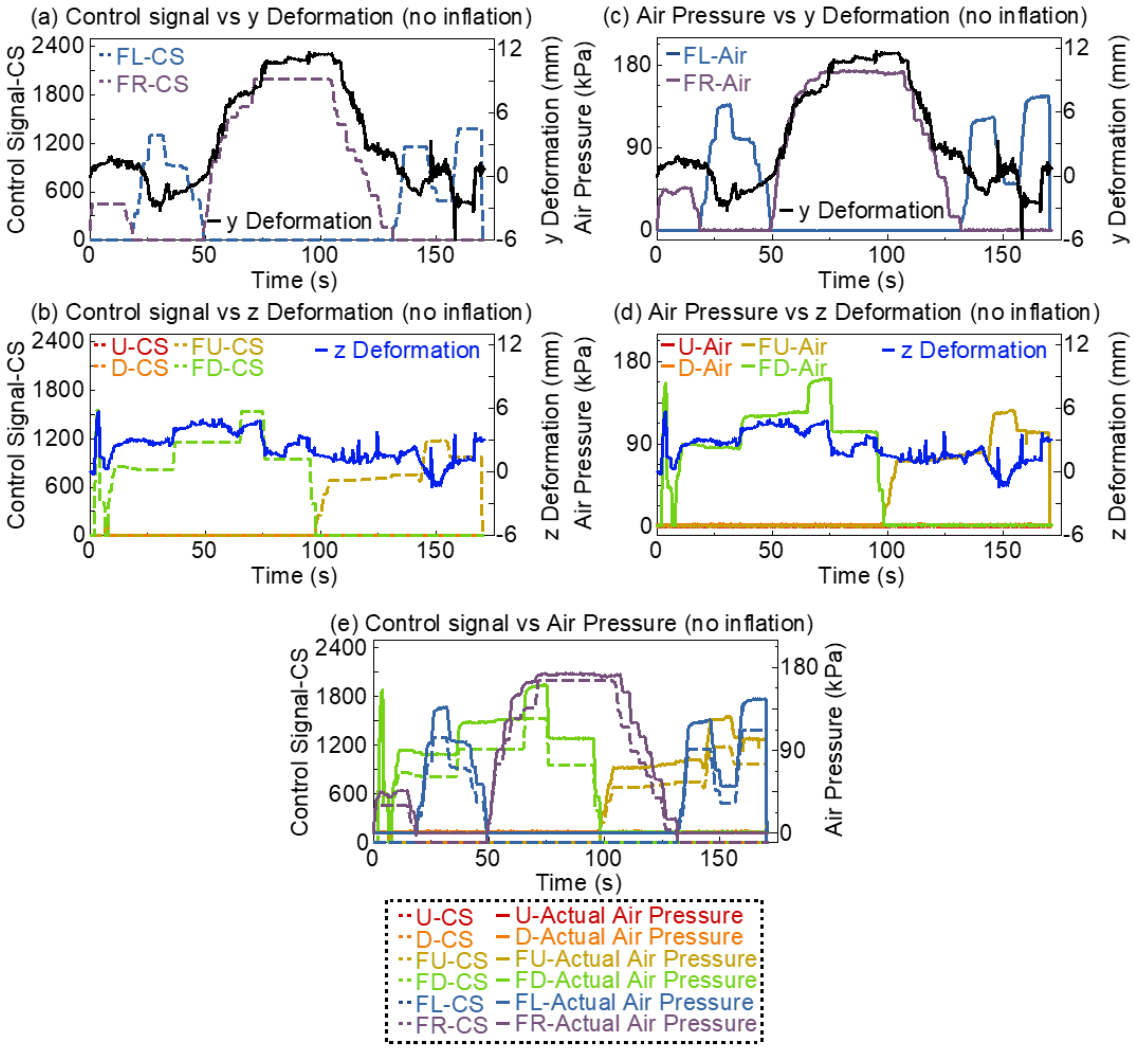

Figure 5.9 Response Dynamics of Soft Actuator under No Inflation Configuration (a) Time-Control Signal vs. y Deformation (b) Time-Control Signal vs. x Deformation (c) Time-Air Pressure vs. y Deformation (d) Time-Air Pressure vs. x Deformation (e) Time-Control Signal vs. Air Pressure

In the enhanced stiffness configuration, the constant higher pressure in the FD chamber facilitated quicker intra-chamber pressure adjustments, significantly reducing the response time to less than 0.3 seconds (mean: 0.3s, standard deviation: 0.1s) when increasing control signals and air pressures, as shown in Figure 5.10(a)-(d). However, as air pressure decreased, the reduction in y and x deformations preceded the reduction in control signal and air pressure. This pre-emptive decrease, illustrated in Figure 5.10(e), suggests that internal pressures could be released more swiftly, potentially leading to unstable chamber interactions and affecting operational control. Despite these potential instabilities, the enhanced stiffness effectively minimized the impact of external disturbances, significantly reducing shaking and improving the actuator's performance in following control signals closely.

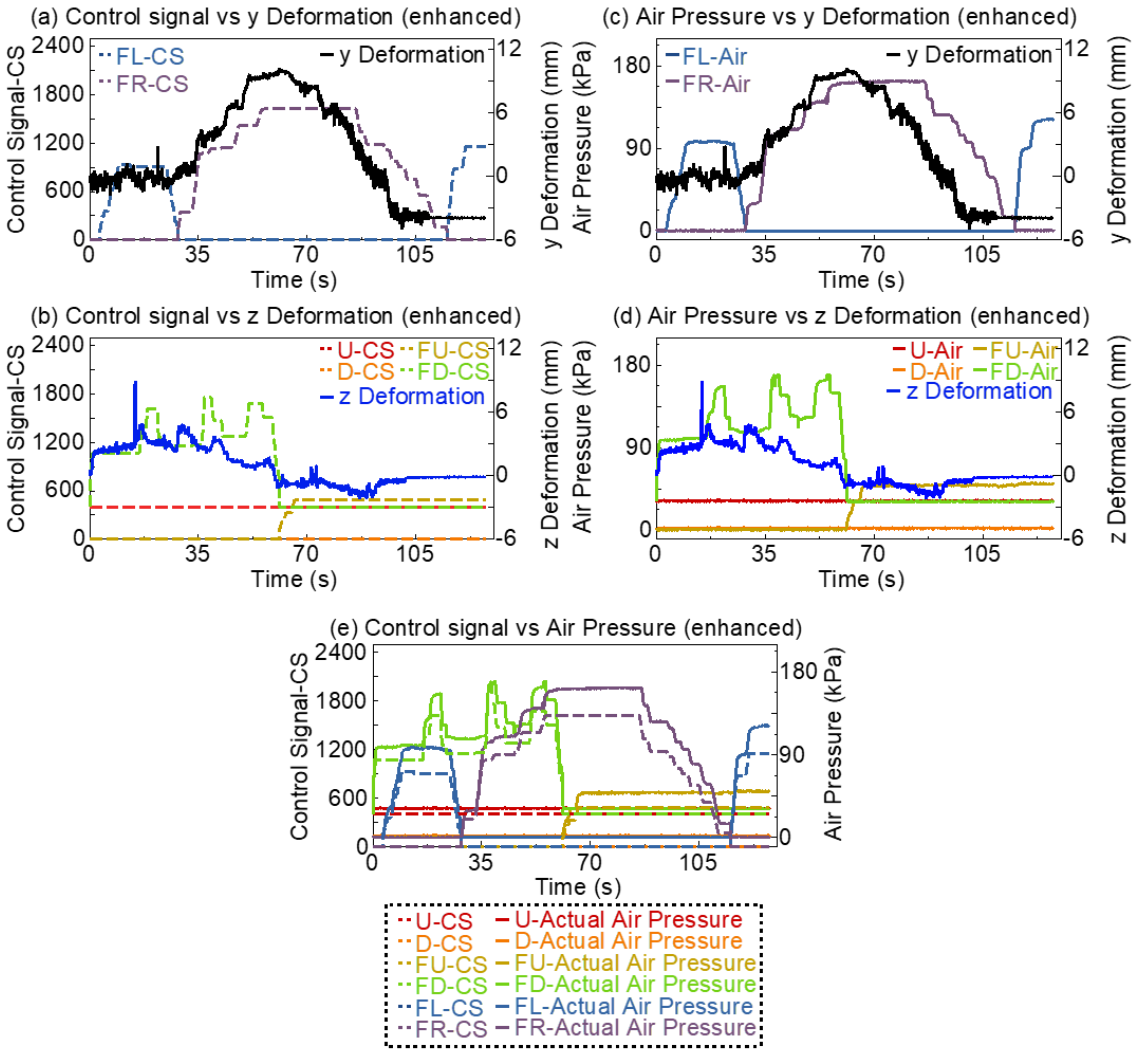

Figure 5.10 Response Dynamics of Soft Actuator under Enhanced Stiffness Configuration (a) Time-Control Signal vs. y Deformation (b) Time-Control Signal vs. x Deformation (c) Time-Air Pressure vs. y Deformation (d) Time-Air Pressure vs. x Deformation (e) Time-Control Signal vs. Air Pressure

The reduced stiffness configuration, maintaining continuous high pressure in the FU, FL, and FR chambers, showed improved response times to both increases and decreases in control signals and air pressures (mean increase: 0.3s, standard deviation: 0.1s; mean decrease: 0.9s, standard deviation: 0.2s) as shown in Figure 5.11(e). However, this setup led to significantly worse operational performance, as depicted in Figure 5.11(a)-(d). The reduced rigidity under this configuration made the actuator highly susceptible to external disturbances, resulting in excessive shaking and considerable deviations in y and x deformations. The constant pressure exerted by the FL, FR, and FD chambers compounded these effects, further diminishing stability and control, leading to erratic behavior and reduced operability.

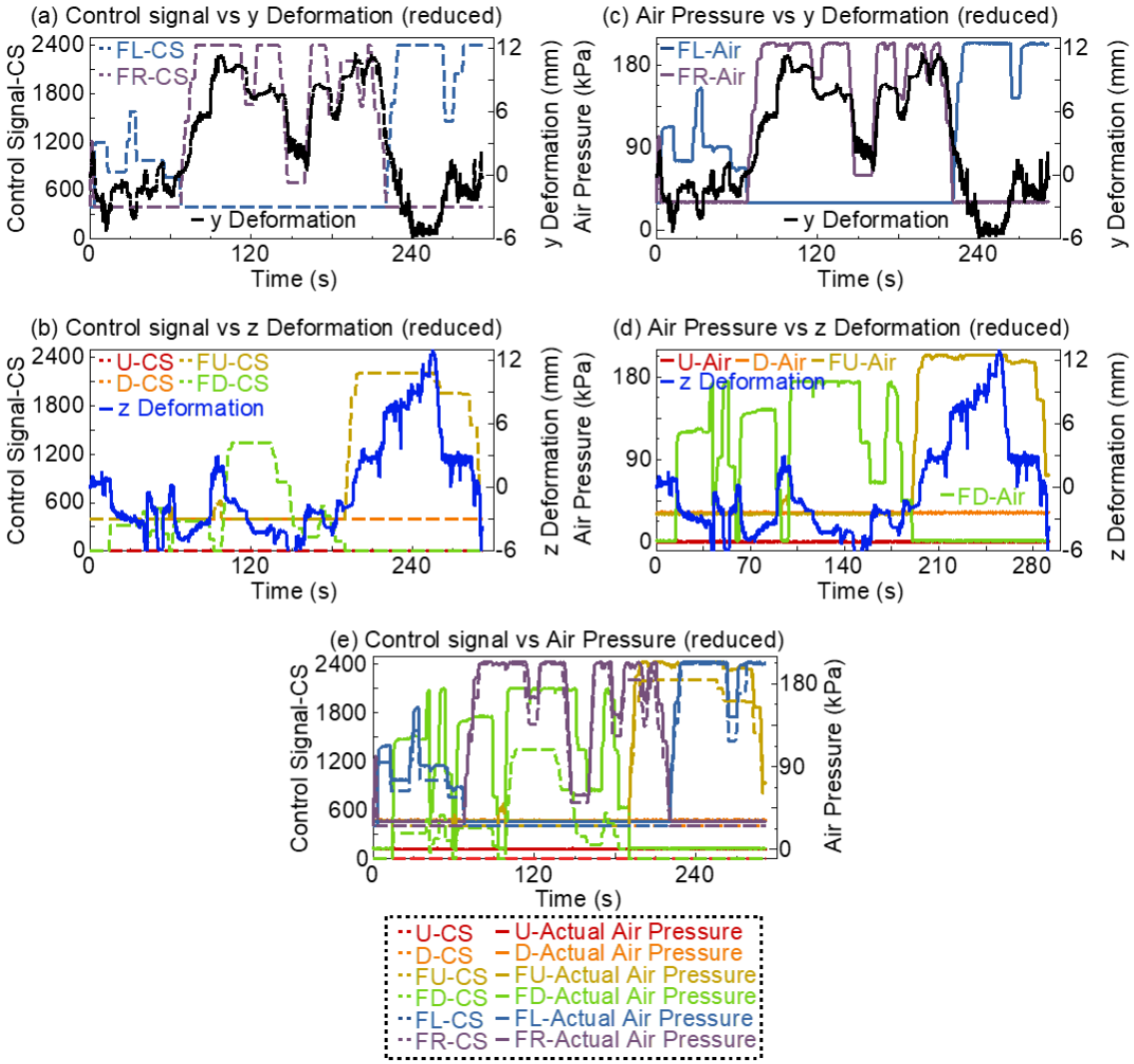

Figure 5.11 Response Dynamics of Soft Actuator under Reduced Stiffness Configuration (a) Time-Control Signal vs. y Deformation (b) Time-Control Signal vs. x Deformation (c) Time-Air Pressure vs. y Deformation (d) Time-Air Pressure vs. x Deformation (e) Time-Control Signal vs. Air Pressure

The observed delays and operational challenge caused by electronic proportional valves and complex interactions within the actuator's chambers significantly affect a surgeon's ability to perform precise manipulations during surgery. This underscores the necessity for refined approaches in future research (detailed in 5.6 Future Work) to enhance both the performance and reliability of the actuator.

5.6. Future Work

To address these challenge, future efforts will concentrate on developing sophisticated models and simulations that accurately depict the dynamic interactions among different chambers of the soft actuator. These models will incorporate the delays caused by

electronic proportional valves and assess their impact on actuator deformations. By using simulations to predict and optimize the behavior of the actuator across various stiffness configurations, we can ensure that these models reflect real-world surgical conditions and allow for preemptive adjustments in control strategies to mitigate observed lags and inconsistencies.

Implementing advanced control systems that can dynamically adjust air pressure based on real-time feedback from the actuator's performance will also be crucial. These systems will compensate for the delays in valve response and the non-linear behavior of the actuator. Moreover, employing machine learning algorithms to predict and mitigate the effects of external disturbances on the actuator's behavior could significantly enhance stability and response accuracy.

Extensive experimental trials will be conducted to validate the new models and control systems, aiming to replicate the complex conditions of surgical environments to test the actuator's performance under both controlled and uncontrolled disturbances. Comparative studies between the current and improved systems will be crucial to quantifying the benefits of the proposed enhancements and determining their impact on surgical outcomes.

Integrating more robust and sensitive sensors to provide accurate feedback on the actuator's position and deformation in real time will also be vital. This data will aid in fine-tuning control algorithms and ensuring precise actuator movement. Developing feedback loops that adjust to real-time measurements and incorporate predictive adjustments based on the anticipated behavior of the actuator under certain loads and pressures will further enhance the system's efficiency.

These advancements are essential for the progression of robotic surgery, where precision and reliability are paramount. By addressing the current limitations in actuator design and control, these efforts will lead to more robust, reliable, and precise surgical tools. This will ultimately improve surgical outcomes by allowing surgeons to perform complex maneuvers with greater accuracy and confidence, reducing the risk of complications and enhancing patient safety.

Future efforts will focus on optimizing stiffness settings to strike an optimal balance between flexibility and stiffness, thus enhancing the actuator's adaptability to various surgical scenarios. Additional research is necessary to refine the actuator's feedback mechanisms and control systems to minimize the need for manual adjustments and boost overall procedural efficiency. These advancements are crucial for the continued development and deployment of soft actuators in complex minimally invasive surgeries.

6. Conclusion and future work

6.1. Preface

In this thesis, we have thoroughly explored the potential of soft actuators for use in minimally invasive surgeries (MIS), with a focus on complex procedures like single-port transvesical prostatectomy. Our investigation covered the necessity for precise navigation and stable control of surgical instruments in unstructured environments such as the bladder and urethra. We demonstrated that soft actuators equipped with multiple pneumatic antagonistic chambers not only enable essential multi-degree of freedom (Multi-DoF) and stiffness modulation without additional equipment but also complicate interactions when inserting endoscopes through their hollow central passages. Through Finite Element Analysis (FEA) simulations and prototype testing, we identified how friction from chamber designs influences bending properties, response property, and overall actuator performance. Additionally, we developed an advanced neural network-based mechanism for precise stiffness adjustment in response to external loads, enhancing the adaptability during surgeries. The culmination of our research was the development and preliminary testing of a master-slave framework that demonstrated the potential of our actuator design to enhance surgical precision and safety. This final chapter summarizes these findings and discusses future avenues for research to advance the design and application of soft actuators in complex MIS.

6.2. Summary of contribution

The contributions of Ph.D. project have advanced the application and understanding of soft actuators in MIS, reflecting improvements across design and function:

1. Elucidation of Cross-Sectional Shapes
   We demonstrated how the shape of pneumatic chambers impacts the bending properties, response dynamics, and stiffness of soft actuators, with a focus on the crucial role of frictional forces. This understanding is pivotal for designing actuators that balance operational performance with surgical precision and safety.
2. Stiffness Modulation Mechanisms
   Through the development and analysis of a Finite Element Analysis (FEA) simulation model, we clarified the mechanisms of stiffness modulation in actuators with multiple antagonistic chambers. This enhanced our ability to design actuators that can be finely tuned for specific surgical needs, improving control over surgical instruments during procedures.
3. Advanced Load Sensing and Stiffness Adjustment:
   We tackled the issue of inaccurate load predictions by developing a neural network-based active-sensing scheme and an environment exploration strategy. This approach significantly reduced estimation errors and improved the success rate of load adjustments, enabling surgeons to better manage varying external loads during surgeries.
4. Practical Application through a Master-Slave Framework
   We devised and tested a master-slave framework to assess the practical relevance of our soft actuators. Initial surgical simulations demonstrated the actuator's potential to

enhance surgical precision and safety, confirming its effectiveness in real-world surgical settings.

Overall, this research has provided valuable insights that contribute to the ongoing evolution of MIS technology, enhancing actuator design and performance in complex surgical environments.

6.3. Summary of Future work

The future work and limitations identified in this study set a clear path for advancing the application of soft actuators in MIS. Here is a concise summary of the main points:

1. Inter-chamber Interference and Endoscope Impact:
   Future studies need to thoroughly explore the potential interference between multiple antagonistic air-chamber pairs and assess how variations in the dimensions and shapes of endoscopes affect actuator performance. Understanding these interactions is crucial for optimizing actuator design and functionality.
2. Frictional Consistency
   Since friction is a significant factor in actuator performance, further research is necessary to investigate how frictional properties change with prolonged use and under different conditions. This will help in ensuring consistent actuator performance over time.
3. Discrepancy in Stiffness Prediction
   The existing FEA models show discrepancies in predicting the stiffness of soft actuators under high-load conditions, limiting the precision of stiffness control. Development of an advanced control system is planned to dynamically modulate and precisely control stiffness. This system will allow real-time adjustments to the inflation levels within the chambers, improving the correlation between predicted and real-world actuator performance, especially under higher loads.
4. Limited Scope of Practical Testing
   Preliminary tests have not fully validated the stiffness modulation functionality of the actuators in actual surgical scenarios. Extensive practical evaluations are planned, including tests with animal models and synthetic organs to better simulate the range of surgical challenge. These tests are aimed at rigorously assessing the performance, adaptability, and reliability of the actuators in conditions that closely mimic actual surgeries.
5. Model Flexibility
   The adaptability of our FEA model suggests its potential applicability to a range of soft actuator designs and configurations. Further research is needed to extend the utility of our model to diverse surgical applications and actuator designs.
6. Advanced Sensing and Feedback Control
   Future studies will also focus on expanding the load active-sensing scheme to different directions of multi-DoFs soft actuators and designing a closed-loop feedback controller for desired angle and stiffness adjustments.

Addressing these limitations and pursuing the outlined future work are essential steps toward enhancing the practical utility and predictive accuracy of soft actuators in MIS.

This research not only highlights current challenge but also opens avenues for significant advancements in soft robotics.

6.4. Conclusion

In conclusion, this doctoral thesis has significantly advanced our understanding of soft actuators within the context of minimally invasive surgeries (MIS), specifically targeting complex procedures such as single-port transvesical prostatectomy. Our research has meticulously examined the integration and functionality of soft actuators, which require precise navigation and stable control in unstructured surgical environments like the bladder and urethra. We have shown that while multiple pneumatic antagonistic chambers provide essential multi-degree of freedom (Multi-DoF) and enable stiffness modulation, they also introduce complexities when combined with endoscopes through the actuator's hollow central passage. Through detailed Finite Element Analysis (FEA) simulations and prototype testing, we discovered how the design of these chambers and the resulting friction influence bending properties, response dynamics, and overall actuator performance. Further, our development of an advanced neural network-based mechanism for adjusting stiffness in response to external loads has markedly enhanced surgical adaptability. The project culminated in the development and preliminary testing of a master-slave framework, proving the enhanced surgical precision and safety capabilities of our actuator design. While these advancements mark significant progress, ongoing efforts to refine control mechanisms and conduct extensive real-world testing are essential for transitioning these technologies into clinical practice. The potential for future applications and improvements remains vast, setting the stage for further innovations in soft robotic systems for MIS.

REFERENCE

[1] J. Burgner-Kahrs, D. C. Rucker, and H. Choset, “Continuum Robots for Medical Applications: A Survey,” IEEE Trans. Robot., vol. 31, pp. 1261–1280, 2015. DOI: 10.1109/TRO.2015.2489500

[2] M. B. Mariano, T. M. Graziottin, and M. V. Tefilli, “Laparoscopic prostatectomy with vascular control for benign prostatic hyperplasia,” J. Urol., vol. 167, pp. 2528–2529, 2002.

[3] T. C. McCullough, F. L. Heldwein, S. J. Soon, et al., “Laparoscopic versus open simple prostatectomy: an evaluation of morbidity,” J. Endourol., vol. 23, pp. 129–133, 2009.

[4] J. Kaouk, “Single-Port Percutaneous Transvesical Simple Prostatectomy Using the SP Robotic System: Initial Clinical Experience,” 2020.

[5] K. T. McVary, P. Dahm, T. S. Kohler, et al., “Surgical management of lower urinary tract symptoms attributed to benign prostatic hyperplasia: AUA Guideline Amendment 2019,” J. Urol., vol. 202, pp. 592–598, 2019. DOI: 10.1097/JU.0000000000000319

[6] [6] M. F. Dall'Oglio, M. Srougi, A. A. Antunes, A. Crippa, and J. Cury, “An improved technique for controlling bleeding during simple retropubic prostatectomy: a randomized controlled study,” BJU Int., vol. 98, no. 2, pp. 384–387, 2006. DOI: 10.1111/j.1464-410X.2006.06236.x

[7] M. Ferretti and J. Phillips, “Prostatectomy for benign prostate disease: open, laparoscopic and robotic techniques,” 2015.

[8] P. L. Anderson, R. A. Lathrop, and R. A. Webster, “Robot-like dexterity without computers and motors: A review of handheld laparoscopic instruments with wrist-like tip articulation,” Expert Rev. Med. Devices, vol. 13, pp. 661–672, 2016.

[9] K. Fareed, O. M. Zaytoun, R. Autorino, et al., “Robotic single port suprapubic transvesical enucleation of the prostate (R-STEP): initial experience,” BJU Int., vol. 110, pp. 732–737, 2012.

[10] B. Gorissen, W. Vincentie, F. Al-Bender, et al., “Modeling and bonding-free fabrication of flexible fluidic micro-actuators with a bending motion,” J. Micromech. Microeng., vol. 23, p. 045012, 2013.

[11] Y. Elsayed, A. Vincensi, C. Lekakou, et al., “Finite element analysis and design optimization of a pneumatically actuating silicone module for robotic surgery applications,” Soft Robot., vol. 1, pp. 255–262, 2014.

[12] M. Runciman, A. Darzi, and G. P. Mylonas, “Soft robotics in minimally invasive surgery,” Soft Robot., vol. 6, pp. 423–443, 2019. DOI: 10.1089/soro.2018.0136

[13] Y. Chang, W. Xu, J. Wu, Y. Xiao, Y. Wang, M. Chen, and D. Gu, “Transvesical Single-Port Robotic Radical Prostatectomy on da Vinci Si: A Safe Access for Patients with Previous Open Surgery for Rectal Cancer,” Videourology, vol. 36, p. 1, 2022.

[14] S. Kokubu, Y. Wang, P. E. Tortós Vinocour, Y. Lu, S. Huang, R. Nishimura, Y. H. Hsueh, and W. Yu, “Evaluation of Fiber-Reinforced Modular Soft Actuators for Individualized Soft Rehabilitation Gloves,” Actuators, vol. 11, pp. 1–21, 2022. DOI: 10.3390/act11030084

[15] S. Guiherme, A. Aminsharifi, J. Garisto, et al., “Single-port transvesical robotic simple prostatectomy using the novel SP surgical system: Technical aspects,” Urol. Video J., vol. 5, p. 100022, 2020. DOI: 10.1016/j.urolvj.2019.100022

[16] H. E. Foster, P. Dahm, T. S. Kohler, et al., “Surgical management of lower urinary tract symptoms attributed to benign prostatic hyperplasia: AUA Guideline Amendment 2019,” J. Urol., vol. 202, pp. 592–598, 2019. DOI: 10.1097/ju.0000000000000319

[17] H. Abidi, G. Gerboni, M. Brancadoro, et al., “Highly dexterous 2-module soft robot for intra-organ navigation in minimally invasive surgery,” Int. J. Med. Robot. Comput. Assist. Surg., vol. 14, pp. 1–9, 2018. DOI: 10.1002/rcs.1875

[18] I. De Falco, M. Cianchetti, and A. Menciassi, “A soft multi-module manipulator with variable stiffness for minimally invasive surgery,” Bioinspir. Biomim., vol. 12, p. 056008, 2017. DOI: 10.1088/1748-3190/aa7ccd

[19] M. S. Xavier, A. J. Fleming, and Y. K. Yong, “Finite element modeling of soft fluidic actuators: overview and recent developments,” Adv. Intell. Syst., vol. 3, p. 2000187, 2021. DOI: 10.1002/aisy.202000187

[20] Y. Lu, Z. Zhou, P. E. Tortós Vinocour, et al., “Effects of chamber shapes on maneuverability and control property of endoscope-support soft actuators,” Front. Bioeng. Biotechnol., vol. 11, p. 1319922, 2023. DOI:10.3389/fbioe.2023.1319922.10.3389/fbioe.2023

[21] Y. Lu, Z. Zhou, S. Kokubu, et al., “Neural network-based active load-sensing scheme and stiffness adjustment for pneumatic soft actuators for minimally invasive surgery support,” Sensors, vol. 23, p. 833, 2023. DOI: 10.3390/s23020833

[22] J. H. Low, M. H. Ang, and C. H. Yeow, "Customizable soft pneumatic finger actuators for hand orthotic and prosthetic applications," in Proc. IEEE Int. Conf. Rehabil. Robot., 2015, pp. 380-385. DOI: 10.1109/ICORR.2015.7281229

[23] R. Deimel and O. Brock, "A novel type of compliant and underactuated robotic hand for dexterous grasping," Int. J. Robot. Res., vol. 35, no. 1-3, pp. 161-185, 2016. DOI: 10.1177/0278364915592961

[24] K. Suzumori, S. Endo, T. Kanda, N. Kato, and H. Suzuki, "A bending pneumatic rubber actuator realizing soft-bodied manta swimming robot," in Proc. IEEE Int. Conf. Robot. Autom., 2007, pp. 4975-4980. DOI: 10.1109/ROBOT.2007.364246

[25] Y. Wang, S. Kokubu, Z. Zhou, X. Guo, Y. Hsueh, and W. Yu, "Designing soft pneumatic actuators for thumb movements," IEEE Robot. Autom. Lett., vol. 6, pp. 8450-8457, 2021. DOI: 10.1109/LRA.2021.3105799

[26] S. Wakimoto, K. Ogura, K. Suzumori, and Y. Nishioka, "Miniature soft hand with curling rubber pneumatic actuators," in Proc. IEEE Int. Conf. Robot. Autom., 2009, pp. 556-561. DOI: 10.1109/ROBOT.2009.5152259

[27] Y. S. Narang, J. J. Vlassak, and R. D. Howe, " Mechanically Versatile Soft Machines through Laminar Jamming," Adv. Funct. Mater., vol. 28, p. 1707136, 2018. DOI: 10.1002/adfm.201707136

[28] Y. Li, Y. Chen, Y. Yang, et al., "Passive particle jamming and its stiffening of soft robotic grippers," IEEE Trans. Robot., vol. 33, pp. 446-455, 2017. DOI: 10.1109/TRO.2016.2636899

[29] A. Stilli, H. A. Wurdemann, and K. Althoefer, "Shrinkable, stiffness-controllable soft manipulator based on a bio-inspired antagonistic actuation principle," in Proc. IEEE Int. Conf. Intell. Robots Syst., 2014, pp. 2476-2481. DOI: 10.1109/IROS.2014.6942899

[30] Z. Zhou, R. Wang, X. Huang, et al., "Optimization of spring constant of a pneumatic artificial muscle-spring driven antagonistic structure," IEEE Robot. Autom. Lett., vol. 7, pp. 5982-5989, 2022. DOI: 10.1109/LRA.2022.3162021

[31] D. Rus and M. T. Tolley, "Design, fabrication and control of soft robots," Nature, vol. 521, pp. 467-475, 2015. DOI: 10.1038/nature14543

[32] A. D. Marchese, R. K. Katzschmann, and D. Rus, "A recipe for soft fluidic elastomer robots," Soft Robot., vol. 2, pp. 7-25, 2015. DOI: 10.1089/soro.2014.0022

[33] H. L. Heung, Z. Q. Tang, X. Q. Shi, et al., "Soft rehabilitation actuator with integrated post-stroke finger spasticity evaluation," Front. Bioeng. Biotechnol., vol. 8, p. 111, 2020. DOI: 10.3389/fbioe.2020.00111

[34] F. Connolly, P. Polygerinos, C. J. Walsh, et al., "Mechanical programming of soft actuators by varying fiber angle," Soft Robot., vol. 2, pp. 26-32, 2015. DOI: 10.1089/soro.2015.0001

[35] G. Agarwal, N. Besuchet, B. Audergon, et al., " Untethered soft robot capable of stable locomotion using soft electrostatic actuators.," Sci. Rep., vol. 6, p. 34224, 2016. DOI: 10.1038/srep34224

[36] J. Cao, L. Qin, J. Liu, et al., " Irrigation-based surgical system: feasibility study on transvesical radical prostatectomy in a porcine model for future development of simple robotic systems.," Extrem. Mech. Lett., vol. 21, pp. 9-16, 2018. DOI: 10.1016/j.eml.2018.02.004

[37] T. L. Buckner, E. L. White, M. C. Yuen, R. A. Bilodeau, and R. K. Kramer, “A Move-and-Hold Pneumatic Actuator Enabled by Self-Softening Variable Stiffness Materials,” in Proc. IEEE Int. Conf. Intell. Robot. Syst., 2017, pp. 3728–3733. DOI: 10.1109/IROS.2017.8206221

[38] B. W. K. Ang and C.-H. Yeow, “A Learning-Based Approach to Sensorize Soft Robots,” Soft Robot., vol. 00, pp. 1–10, 2022. DOI: 10.1089/soro.2020.0172

[39] L. Gerez and M. Liarokapis, “A Pneumatically Driven, Disposable, Soft Robotic Gripper Equipped with Retractable, Telescopic Fingers,” in Proc. IEEE RAS EMBS

Int. Conf. Biomed. Robot. Biomechatronics, 2020, pp. 36–41. DOI: 10.1109/BioRob49111.2020.9224292

[40] J. Byun, Y. Lee, J. Yoon, B. Lee, E. Oh, S. Chung, T. Lee, K. J. Cho, J. Kim, and Y. Hong, “Electronic Skins for Soft, Compact, Reversible Assembly of Wirelessly and Fully Soft Robots,” Sci. Robot., vol. 3, pp. 1–12, 2018. DOI: 10.1126/scirobotics.aas9020

[41] N. Lu and D. H. Kim, “Flexible and Stretchable Electronics Paving the Way for Soft Robotics,” Soft Robot., vol. 1, pp. 53–62, 2014. DOI: 10.1089/soro.2013.0005

[42] H. Mirzanejad and M. Agheli, “Soft Force Sensor Made of Magnetic Powder Blended with Silicone Rubber,” Sensors Actuators A Phys., vol. 293, pp. 108–118, 2019. DOI: 10.1016/j.sna.2019.04.021

[43] S. Ceron, I. Cohen, R. F. Shepherd, J. H. Pikul, and C. Harnett, “Fiber Embroidery of Self-Sensing Soft Actuators,” Biomimetics, vol. 3, pp. 1–14, 2018. DOI: 10.3390/biomimetics3030024

[44] H. A. Sonar, A. P. Gerratt, S. P. Lacour, and J. Paik, “Closed-Loop Haptic Feedback Control Using a Self-Sensing Soft Pneumatic Actuator Skin,” Soft Robot., vol. 7, pp. 22–29, 2020. DOI: 10.1089/soro.2019.0013

[45] T. Helps and J. Rossiter, “Proprioceptive Flexible Fluidic Actuators Using Conductive Working Fluids,” Soft Robot., vol. 5, pp. 175–189, 2018. DOI: 10.1089/soro.2017.0012

[46] W. Felt, M. J. Telleria, T. F. Allen, G. Hein, J. B. Pompa, K. Albert, and C. D. Remy, “An Inductance-Based Sensing System for Bellows-Driven Continuum Joints in Soft Robots,” Auton. Robots, vol. 43, pp. 435–448, 2019. DOI: 10.1007/s10514-018-9769-7

[47] K. Chin, T. Hellebrekers, and C. Majidi, “Machine Learning for Soft Robotic Sensing and Control,” Adv. Intell. Syst., vol. 2, p. 1900171, 2020. DOI: 10.1002/aisy.201900171

[48] G. Soter, A. Conn, H. Hauser, and J. Rossiter, “Bodily Finite Element Analysis and Design Optimization of a Pneumatically Actuating Silicone Module for Robotic Surgery Applications.,” in Proc. IEEE Int. Conf. Robot. Autom., 2018, pp. 2448–2453. DOI: 10.1109/ICRA.2018.8463169

[49] J. J. Craig, Introduction to Robotics. New Jersey: Pearson, 2006.

[50] L. Marechal, P. Balland, L. Lindenroth, F. Petrou, C. Kontovounisios, and F. Bello, "Toward a Common Framework and Database of Materials for Soft Robotics," Soft Robot., pp. 284–297, 2021. DOI: 10.1089/soro.2019.0115

[51] T. Igarashi, S. Sakamoto, A. Takei, et al., "Irrigation-based surgical system: feasibility study on transvesical radical prostatectomy in a porcine model for future development of simple robotic systems," Ther Eng., vol. 35, no. 2, 2023.

[52] D. Maruthavanan, A. Seibel, and J. Schlattmann, "Fluid-structure interaction modelling of a soft pneumatic actuator," Actuators, vol. 10, article 163, 2021. https://doi.org/10.3390/act10070163

[53] C. Spearman, "The proof and measurement of association between two things," Am. J. Psychol., vol. 15, pp. 72–101, 1904. https://psycnet.apa.org/doi/10.2307/1412159

[54] F. P. Beer, E. R. Johnston Jr., J. T. DeWolf, et al., Mechanics of Materials, 6th ed. New York, NY: McGraw-Hill, 2012.

[55] S. Garrido-Jurado, R. Muñoz-Salinas, F. J. Madrid-Cuevas, and M. J. Marín-Jiménez, "Automatic Generation and Detection of Highly Reliable Fiducial Markers under Occlusion," Pattern Recognit., vol. 47, pp. 2280–2292, 2014. DOI: 10.1016/j.patcog.2014.01.005

[56] B. Gorissen, M. De Volder, and D. Reynaerts, "Chip-on-Tip Endoscope Incorporating a Soft Robotic Pneumatic Bending Microactuator," Biomed. Microdevices, vol. 20, pp. 1–7, 2018. DOI: 10.1007/s10544-018-0317-1

[57] J. Rosen, B. Hannaford, and R. M. Satava, Eds., *Surgical Robotics: Systems Applications and Visions*. Springer Science & Business Media, 2011.